PHD

Non-inductive solenoid coils based on second generation high-temperature superconductors and their application in fault current limiters

Liang, Fei

Award date:
2017

Awarding institution:
University of Bath

Non-inductive solenoid coils based on second generation high-temperature superconductors and their application in fault current limiters

Fei Liang

A thesis submitted for the degree of Doctor of Philosophy (PhD)
Department of Electrical and Electronic Engineering
University of Bath

2017

Signature_______________ Date_____________

Abstract

The gradual increase in global warming and environmental pollution has made low-carbon technologies an urgent need for the whole world. Superconducting technology, which is known for its extremely high conductivity and high power density, is capable enough to provide novel solutions, contributing to the future smart grid, thus aiding the power industry towards the realisation of a low-carbon and green planet.

In recent decades, several industrial applications using superconducting technology have been developed. Of them, particularly in the power industry, a range of superconducting applications including superconducting magnetic energy storage (SMES), superconducting motors/generators, superconducting cables and superconducting fault current limiters (SFCLs) have been developed. Among them, SFCLs are one of the most promising and are successfully being implemented in power distribution networks.

SFCLs exhibit low impedance during normal operation and gain considerable impedance under a fault condition, providing a new solution to the increasingly high fault current levels. However, most of the SFCL projects are limited to low-voltage and medium-voltage levels, there are very few successful operational trials of high voltage SFCLs. This thesis, for the first time, studies the comprehensive characteristics of solenoid type SFCLs based on second generation (2G) high temperature superconductors (HTS), which may be successfully implemented in power grids with high voltage levels.

The main contributions of this work include three aspects: 1) proposing an innovative method for simulating the AC losses of the solenoid coils and an electro-magneto-thermal model for simulating the SFCL’s current limiting property; 2) comprehensive and in-depth comparison study concerning the application of the two types of non-inductive solenoid coils (braid type and non-intersecting type) in SFCLs both experimentally and numerically; and 3) the first and thorough discussion of the impact of different parameters such as pitch and radius of coils to the overall performance of braid type SFCLs and the validation of the braid type SFCL concept with a 220 V/300 A SFCL prototype.

Based on these experimental and simulation works, the thesis provide strong guidance for the development of future non-inductive solenoid type SFCLs based on 2G HTS, which are promising for high voltage level power grid applications.

Acknowledgement

I would firstly like to thank my Supervisor Dr. Weijia Yuan for his support and guidance in both my study and personal life. His diligence, rigorosity and practicalness have left me with deep impressions and also made him the best example for me to learn from.

Furthermore, my thanks go to Dr. Min Zhang and Dr. Xiaoze Pei, who provided valuable help and advice based on their own rich experience and high academic attainments.

I would also like to thank my colleagues, Dr. Huiming Zhang, Dr. Zhenyu Zhang, Dr. Jianwei Li, Dr. Xiaojian Li, Dr. Yawei Wang, Dr. Jie Sheng, Sriharsha Venuturumilli, Jay Patel, Mariam Elshiekh, Qixing Sun, Dong Xing, Hamoud Alafnan, Muhammad Zulfiqar Ali and Zixuan Zhu, for their selfless help and for those interesting discussions about research. These experiences not only helped me to finish my thesis, but also enriched my personal life in Bath.

Additionally, I want to express my sincere gratitude to the technicians in my department, Andrew Matthews, Michael Linham, Surendra Kaushik, Sivapathasundaram Sivaraya. It would have been impossible for me to finish my thesis without their generous help and precious advice.

Finally, my deepest gratitude goes to my parents, my brother and his wife, and my two young nieces who always love me and to other family members who always help me.

List of Publications as the First Author

[1] **Fei Liang**, Sriharsha Venuturumilli, et al., ‘A finite element model for simulating second generation high temperature superconducting coils/stacks with large number of turns’, Journal of Applied Physics, vol. 122, p. 043903, 2017.

[2] **Fei Liang**, Timing Qu, et al., ‘Vortex shaking study of REBCO tape with consideration of anisotropic characteristics’, Superconductor Science and technology, vol. 30, p. 094006, 2017.

[3] **Fei Liang**, Weijia Yuan, et al., ‘Experimental test of two types of non-inductive solenoidal coils for superconducting fault current limiters use’, IEEE Transactions on Applied Superconductivity, vol.27, p. 5601505, 2017.

[4] **Fei Liang**, Weijia Yuan, et al., ‘AC loss modelling and experiment of two types of low-inductance solenoidal coils,’ Superconductor Science and Technology, vol. 29, p. 115006, 2016.

[5] **Fei Liang**, Weijia Yuan, Min Zhang, Zhenyu Zhang, Sriharsha Venuturumilli, Jay Patel, ‘The impact of critical current inhomogeneity in HTS coated conductors on the quench process for SFCL application’, IEEE Transactions on Applied Superconductivity, vol. 26, p. 560065, 2016.

[6] **Fei Liang**, Weijia Yuan, Carlos A. Baldan, Min Zhang, Jerika S. Lamas, ‘Modeling and experiment of the current limiting performance of a resistive superconducting fault current limiter in the experimental system’, Journal of Superconductivity and Novel Magnetism, vol. 28, p. 2669-2681, 2015.

Contents

Nomenclature

T_c	critical temperature of superconductors
J_c	critical current density of superconductors
H_c	critical magnetic field of superconductors
I_c	critical current of superconductors
i_{nsc}	current of non-superconductor part of a SFCL
i_{sc}	current of superconductor of a SFCL
i_{tot}	total current in SFCL
E	electric field
J	current density
$\boldsymbol{A}$	magnetic vector potential
V	electric scalar potential
$\boldsymbol{T}$	current vector potential
$\mathbf{\Omega}$	magnetic scalar potential
$\boldsymbol{H}$	magnetic field strength
P_h	the pitch of the solenoidal coil
W	the width of the superconductor tape
r	the radius of the solenoidal coil
i	the i^{th} segment of solenoidal coil

N	the division number of ¼ part of solenoidal coil
θ	the azimuthal angle of solenoidal coil
n	the index of superconductor E-J relationship
E_0	1×10^{-4} V/m
J_{cx} and $J_c(x)$	the critical current density of the superconductor tape, which varies in the width direction
T	cycle
A_{sc}	the cross-sectional area of the superconductors
Q_i	the AC losses in segment i *of solenoid coil*
Q_t	the total AC losses
W_{sc}	the width of the superconductor
T_{sc}	the thickness of the superconductor
d_i	the relative deviation
P_i	the AC losses at the i^{th} turn of the braid type coil
$\overline{P}$	the AC losses of the tape in the braid type coil with infinite turns
I_{rms}	RMS value of current
Q_N	the AC losses of the braid type coil with

	division number equalling N
Q_0	the real AC losses of the braid type coil
R_d	the relative tolerance of each simulated AC losses
$L_{cond}^{\lim}$	the limitation length
L_{cond}^{th}	the thermal length
$I_{\lim}$	the limited fault current
$\mathrm{V}_{\mathrm{cond}}$	the voltage across the superconductor tape
R_l^{cond}	the conductor resistance per unit length
A_{cond}	the cross section of the superconductor tape
ρ	the resistivity
ρ_{cond}	the average resistivity of the superconductor tape
Δt	the fault period
$v_{cond}(t)$	the instantaneous voltage across the superconductor tape
$i_{cond}(t)$	the instantaneous current through the superconductor tape
$T_{\max}$	the maximum temperature
T_0	the operation temperatures
$c_p(T)$	the superconductor specific heat per unit volume

L_{cond}^{th}	the thermal length of the superconductor
$\rho_{cond}(T)$	the average resistivity of the different non-superconducting layers that are connected in parallel.
V_{cond}	the RMS voltage applied to the superconductor tape
N_{sc}	the minimum tape number in SFCL
$I_{\max}$	the maximum current during normal operation
L_{sc}	the tape length of SFCL
L_{tot}	the total length of required superconductor
V_c	the volume of the superconducting element of the SFCL
D	the diameter of the superconducting coil
μ_0	the vacuum permeability
μ_r	the relative permeability
H	the magnetic field strength
ρ_{cc}	the resistivity of the coated conductor
ρ_{sc}	the resistivity of the superconductor
ρ_{norm}	the resistivity of the superconductor at room temperature
J_z	the current that flows through the superconducting layer

B, γ and α	the coefficients that are used to define the new E-J relationship of the superconductor (Equations 6.7-6.10)
$J_c(T)$	critical current of superconductor, which is a function of temperature
T_c	the critical temperature of the superconductor
T_0	the temperature of liquid nitrogen
Q	the power density in the superconductor
ρ_m	mass density
C_p	the heat capacity
k	the thermal conductivity
h	the convective heat transfer coefficient
T_s	the temperature of the superconductor surface
R_{metal}	the resistance of non-superconducting layer, which is function of temperature
I_{metal} I	the current of non-superconducting layer
$R_i(\overline{T})$	resistance of the ith layer
$\rho_i(\overline{T})$	resistivity of the ith layer
R_{ybco}	resistance of superconducting layer
T_{ybco}	temperature of the superconducting layer
Rsc	the superconducting layer resistor

List of Figures

List of Tables

Chapter 1 Introduction

1.1 Thesis background

The increasing global power demand and environmental pollution around the world have made it an urgent and necessary task to develop low carbon technologies. Superconducting technology, which is based on the low resistivity and high power density of superconductors, could not only improve the efficiency of power use, but also decrease the emission of carbon dioxide (CO_2). Previous investigations show that the overall power losses between a power plant and the end user can be between 8% to 15% [1]. If conventional electric apparatus are replaced with superconducting devices, most of the losses can be avoided, which would greatly improve the efficiency in transmission/distribution systems and hence, reduce the CO_2 emissions. Therefore, as a key and novel technology, superconductivity has attracted wide attention from researchers and engineers around the world.

Since the discovery of a superconductor in 1911 by Heike Kamerlingh Onnes [2], superconductors have been applied in various industries such as biomedical research and high energy physics. However, the extremely low operational temperature of low temperature superconductors (LTS, usually below 20 K), which increases the cost of superconducting devices, greatly limited their application in the early stage of their development

This situation continued until the discovery of high temperature superconductor (HTS) by J.G. Bednorz and K.A. Müller in 1986 [3], which opened new possibilities for the application of superconductors. Different from low temperature superconductors that need to be cooled with liquid helium, many HTS show transition temperatures higher than 77 K (normal boiling temperature of liquid nitrogen). For example, the transition temperature for Yttrium barium copper oxide (YBCO) and Bismuth strontium calcium copper oxide (BSCCO) are 93 K and 108 K respectively. In addition, the maximum transition temperature recorded at atmospheric pressure is 138 K for $HgBa_2Ca_2Cu_3O_{8+\delta}$ with TI substitution [4] and the highest accepted superconducting critical temperature is 203 K of sulfur hydride under high pressure of 155 GPa [5]. The high critical temperature of HTS implies that liquid nitrogen is sufficient to be used for cooling, which considerably reduces the operating costs of superconducting devices. Moreover, the development of HTS manufacturing technology in recent decades, such as the commercialisation of (RE)BCO and BSCCO, also provided conditions for the large-scale and widespread application of HTS.

As a result, the research concerning the application of HTS in different industries, such as transportation, aerospace, medical and power systems, has been progressing greatly. Amongst them, the application of HTS in power systems has attracted extensive attention, which includes superconducting cables, superconducting transformers, superconducting magnetic energy storage (SMES) systems, superconducting motors/generators and superconducting fault current limiters (SFCLs).

1.2 Introduction of superconductivity

Different from conventional conductors, superconductors exhibit some unique characteristics such as zero resistivity and Meissner effect and have specific requirement concerning their working conditions. In the following sections, these characteristics are discussed in detail.

1.2.1 Zero resistivity characteristics

One of the basic properties of superconductors is their zero electrical resistivity in the superconducting state. As shown in Figure 1.1, when the temperature of a superconductor decreases below the critical temperature T_c, the superconductor will suddenly lose its electrical resistivity. This is an ideal characteristic for a conductor since no loss is generated in the power transmission process with zero resistivity conductor, which saves at least 2.5% of the transmission power [1]. By taking advantage of this characteristic, superconductors have been developed into different apparatuses, such as electromagnets, SFCLs and SMES systems.

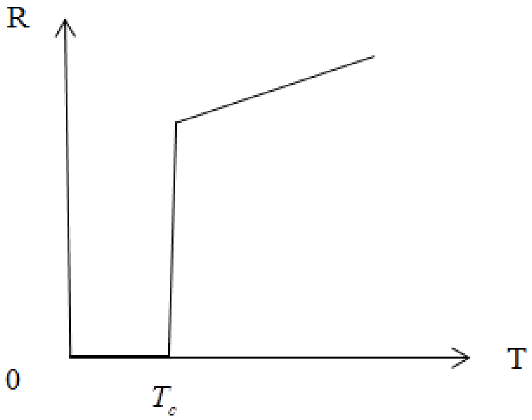

Figure 1.1 Resistance curve of superconductors as a function of temperature

1.2.2 Meissner effect

In 1933, Walther Meissner and Robert Ochsenfeld found that superconducting tin and lead samples excluded nearly all their interior magnetic fields when the temperature was lower than their superconducting transition temperature [6]. This property is named the Meissner effect. The schematics are shown in Figure 1.2.

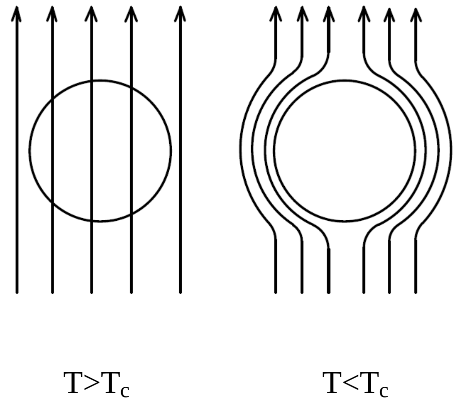

Figure 1.2 Schematic diagram of Meissner effect

As shown in Figure 1.2, when the temperature of a superconductor is higher than its critical temperature ($T>T_c$), the external magnetic field penetrates the superconductor. However, when the temperature is lower than the critical temperature ($T<T_c$), the magnetic field is expelled from the superconductor by the electric current generated on the surface of the superconductor.

1.2.3 Working condition requirements

The operational state of a superconductor, either the superconducting state or the resistive state, is determined by three parameters. The three parameters are current density J, magnetic field H and temperature T, as shown in Figure 1.3. Only when the superconductor is within the grey region defined by the three critical parameters, as shown in Figure 1.3, the superconductor is in the superconducting state with its electrical resistivity being zero. When the superconductor is in the area outside the grey region, it is in its normal state, with a relatively high resistivity. In Figure 1.3, J_c, H_c and T_c refer to the critical current density, the critical magnetic field and the critical temperature respectively. It is worth noting that each critical value varies with the other two parameters.

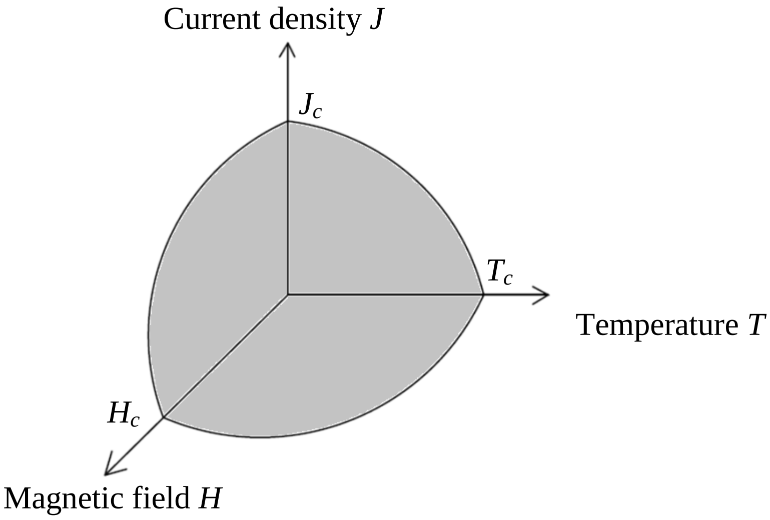

Figure 1.3 Working region of a superconductor

1.3 Application of superconductivity in power systems

To date, various superconducting devices have been developed and used in power systems, including superconducting cables, superconducting transformers, SMES systems, superconducting motors/generators and SFCLs. A Brief introduction is provided here to give a general idea concerning these different superconducting devices.

Superconducting cables utilise superconductors as the current carrying material. Due to the high current density of superconductors, superconducting cables exhibit a higher capacity in compact dimensions [7]. Furthermore, due to their zero resistance characteristic, superconducting cables have much lower transmission losses [7]. Because of the shielding layer used, superconducting cables tend to have no leakage of electro-magnetic field outside of the cable and also possess a low reactance [7]. However, considering the working condition requirements of superconducting cables, cryogenic cooling systems are required to maintain the low temperature of the cables [8].

Superconducting transformers based on HTS have the potential to provide many advantages compared with the conventional transformers. Firstly, a superconducting transformer can be lighter and compact, and the efficiency is higher with a considerable reduction in operational costs [9]. Secondly, there is no increase in losses in overload conditions, which decreases the possibility of damage and increases lifetime [9]. Furthermore, since there is no coolant oil used, there is no risk of fire in superconducting transformers [9].

SMES devices are basically magnets in which energy is stored in the form of a magnetic field, which is created by the flow of direct current in a superconducting magnet. Compared to other types of energy storage systems, SMES is better suited for high power application, especially when the requirement is for a short-term ‘boost’ [10]. Another advantage of SMES is the theoretically infinite number of charge and discharge cycles [10].

Superconductors are used in superconducting motors/generators for building stators/rotors. Due to the low resistivity of superconductors, superconducting motors and generators have higher efficiency and lower losses [10]. Additionally, the high magnetic field in a superconducting machine tends to allow large air-gaps and air-core machines, which results in high short-circuit ratio and higher tolerance in frame-bending distortion [10]. However, there are several factors that need to be considered in the design of superconducting motors/generators, such as cryogenic system, AC losses, effect of AC magnetic field on a superconductor, quench and mechanical stresses.

SFCLs are mainly used for limiting the fault current to a value within the capacity of circuit breakers when a fault occurs in a power grid, enabling the circuit breaker to shut down the fault current successfully. To date, different types of SFCLs have been proposed, such as resistive type, inductive type, transformer type, magnetic-shield type and saturated core type [11]. Some prototypes have been installed in power grids for operational experience. Compared to the traditional fault current limiters, the main difference of the SFCL is that it has little impact on a power grid in normal conditions, but gains considerable resistance when a fault occurs. Furthermore, with SFCLs the fault can be limited in a small area of the power system, without cascading expansion of the affected area of the fault. However, the application of SFCL in the power grid will introduce new challenges to the existing relay protection of power systems. Another disadvantage of SFCL is the high cost of HTS material, usually $50/m for 4 mm SuperPower tape. However, this cost issue will be solved with the gradual decrease in superconductor prices.

1.4 Thesis purpose and structure

Since the discovery of high-temperature superconductors, the application of superconductors in SFCLs has been a popular and important research topic in the applied superconductivity area. Different types of SFCLs have been proposed and some of them have already been applied in power grids [12-16]. However, most of the SFCL projects are limited to low-voltage and medium-voltage levels. Although there are several reports concerning the concept, design and development of high voltage SFCLs, successful operations in power grids are limited. In this work, a new non-inductive type (the braid type) SFCL which is advantageous in withstanding high voltage, is designed, built and tested. To improve people’s understanding of the braid type SFCL, the salient characteristics of this type of SFCL, such as AC losses, quench uniformity and current limiting property are investigated and discussed in detail.

This thesis is composed of seven parts.

In Chapter 2, the background knowledge of different types of SFCLs, the main challenge of resistive type SFCLs and the previous simulation studies concerning AC losses and current limiting performance of SFCLs are reviewed and summarised.

In Chapter 3, the basic characteristics of two non-inductive solenoid type SFCLs (the braid type and the non-intersecting type) are compared in detail, which includes the current limiting property, the AC losses characteristic and the recovery characteristic.

In Chapter 4, the AC loss characteristics of the two types of SFCLs are studied both experimentally and numerically. Using the two-dimensional (2-D) finite element models, the electro-magnetic characteristics and AC loss characteristics of the two types of SFCLs are analysed in detail. Furthermore, using the models, the impacts of different factors on the AC losses of the SFCLs are studied further.

In Chapter 5, a 220 V/300 A braid type SFCL based on second generation (2G) HTS is designed, built, tested and evaluated to validate the application of braid type SFCLs in high voltage level applications.

In Chapter 6, an electro-magneto-thermal model is proposed for simulating the current limiting performance of SFCLs, which is validated with a 220 V resistive type SFCL.

Chapter 7 analyses the impact of different factors on the quench process of SFCLs, including the critical current (I_c) inhomogeneity, the thickness of the stabiliser and the shunt resistor.

Finally, conclusions are provided in Chapter 8, summarising the key results of the entire thesis.

Chapter 2 Research status of superconducting fault current limiters

With the growth of electricity demand and the corresponding structural changes in power grids, higher and more frequent fault currents are expected to occur in power grids. To cope with the problem, different solutions have been proposed, such as current limiting reactors, high impedance transformers, high voltage fuses, building new substations and bus splitting [11]. However, most of the traditional measures such as high impedance transformers and current limiting reactors lead to permanent impedance increase even during normal operation, which is in contradiction with the power quality requirement of power grids. Furthermore, some other methods such as fuses need equipment replacement, which is usually time-consuming and influences the normal operation of power grids.

Therefore, it becomes urgent and essential to develop devices that can effectively limit fault current but have no impact on power grids during normal operation. Based on the characteristics of superconductors, superconducting fault current limiters (SFCLs) have been proposed for limiting fault current in recent decades. Different from those traditional solutions, SFCLs have negligible impact on power grids in normal operation, but gain considerable impedance, in milliseconds, under fault conditions.

In this Chapter, the current research status of SFCLs is summarised and discussed to provide a comprehensive overview of SFCLs. In general, the summarisation is composed of three parts: 1) review of different types of SFCLs; 2) the main challenges in the development of resistive type SFCLs; and 3) review of previous research concerning simulation of SFCLs.

2.1 Review of different types of SFCLs

Many types of SFCLs have been proposed and built and some of them have been operated in power grids. Generally speaking, the SFCLs proposed include five topologies: resistive type, bridge type, DC biased iron core type, shielded iron core type, and hybrid type. In the following sub-sections, the definition, characteristics and development of each type of SFCLs are introduced and discussed. All the discussion provided here are limited to SFCLs based on high-temperature superconductors.

2.1.1 Resistive type SFCL

1) Working principle

The resistive type SFCL is based on the transition of a superconductor from the superconducting state to the normal state under fault conditions. When a fault occurs, the system current exceeds the critical current of SFCLs, which leads to heat generation and an increase in temperature of the superconductor. When the superconductor temperature exceeds its critical temperature, the superconductor will lose its superconductivity (also known as quench), which is accompanied by the sudden increase of superconductor resistivity, as shown in Figure 1.1.

A high-temperature superconductor is composed of two main parts: the superconducting part, which is composed of superconducting layers and the non-superconducting part that consists of stabiliser, protective, substrate and buffer layers. For simplification, a SFCL can be regarded as a parallel connection of a superconducting layer and a shunt resistor, as shown in Figure 2.1.

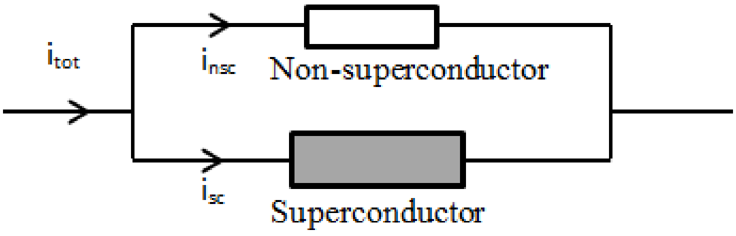

Figure 2.1 Schematic diagram of a SFCL

During normal operation, almost all the current flows through the superconducting layer due to its negligible resistivity and the voltage drop across the superconductor is approximately zero. However, when a fault occurs, the total current (i_{tot}) exceeds the critical current of the superconductor (I_c), which leads to the current diverted to the non-superconductor part, resulting heat generation and the quench of superconductors. The quench of a superconductor increases the resistance of a SFCL and limit the fault current to a lower value within the interrupting capacity of the circuit breaker.

2) Types and structures

To date, resistive type SFCLs have been the most popular and different types of resistive SFCLs have been proposed such as straight line type, pancake type and solenoid type. The structures of these types of SFCLs are shown in Figure 2.2.

In all these types of SFCLs, the superconductors are wound so as to cancel the magnetic field generated. For the long straight type SFCL, the magnetic fields generated by adjacent tapes cancel each other between the tapes. For the pancake type coils and non-intersecting type coils, the current directions in the adjacent tapes are opposite to each other. In the braid type coil, the two windings are wound in different directions and the current flows both from top to bottom of the cylinder, therefore, the magnetic fields generated also cancel each other. There are several advantages for the non-inductive type windings. On one hand, a lower SFCL inductance results in lower impact on power grids during the normal operation, which is paramount for power grids to avoid poor voltage regulation, reduced power quality and the power transmission capability. On the other hand, due to the decrease of magnetic field and the corresponding current density increase, this will also decrease the AC losses of SFCLs during normal operation.

Furthermore, a new concept of resistive type SFCL, which introduces a novel protection technique taking advantage of the magnetic field dependence of critical current density, was also proposed [17]. In this type, a normal conducting coil is wound around a superconducting tube and connected in parallel with the tube. When a fault occurs, the quench of the superconducting tube shunts part of fault current to the coil and the resulting magnetic field drives the superconducting material into fast and homogeneous quench [17].

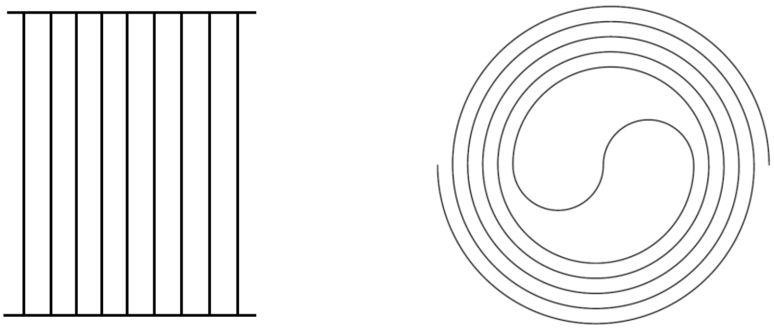

(a) straight line type (b) pancake type

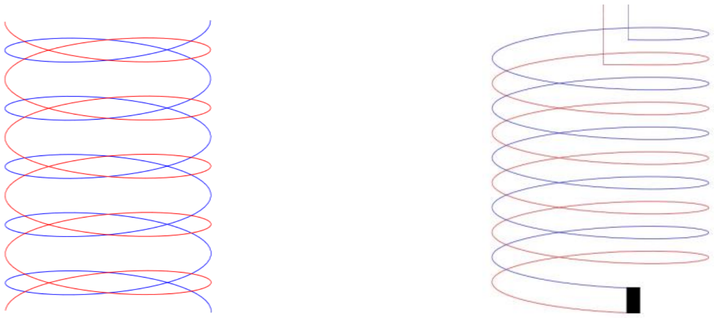

(c) braid solenoid type (d) non-intersecting solenoid type

Figure 2.2 Schematic diagrams of different structures of resistive type SFCLs: (a) Straight line type; (b) pancake type; (c) braid solenoid type; (d) non-intersecting solenoid type

3) Advantages and disadvantages

Resistive type SFCLs are generally compact, fail-safe and have negligible AC losses due to low inductance characteristics. However, due to the quench of a superconductor during a fault condition, recovery time is needed before inserting a SFCL back into the power grid. The recovery time is approximately several seconds for thin film superconductors and is within a minute for bulk superconductor material [11]. Another drawback is the losses generated by heat conduction in the current leads. Generally speaking, 40-50 W/kA heat loss per current lead at cold temperature should be taken into consideration in the design process [11]. Finally, hot spots have been a main problem in resistive SFCLs, which is mainly because of the inhomogeneous distribution of critical current density in superconductors. Previous research shows that the critical current density inhomogeneity leads to the excursion of maximum temperature for low voltage fault in the current limiting process [18, 19]. Furthermore, the low normal zone propagation velocity (NZPV) of 2G HTS tape also makes the elimination of hot spots difficult [20, 21].

4) Summary of resistive type fault current limiter projects

In the past two decades, many resistive SFCL prototypes have been built and some have been operated in power grids on trial basis. Most of these prototypes are based on high-temperature superconductors such as BSCCO and YBCO and only a few of them are made of magnesium diboride (MgB_2).

Europe has been leading in the research and development of resistive type SFCLs. A three-phase 10 kV/10 MVA SFCL demonstrator CURL 10, which is based on high-temperature superconducting BSCCO-2212 bulk material, has been successfully tested in the electrical network of the German utility RWE in 2004-2006 [22]. In the project, the structure used is the non-intersecting type bifilar coils, where the superconductors are connected in series and the electrical inductance of the coil is negligible. Considering the difficulty to scale up the bifilar coil concept to higher voltages, a new concept based on the magnetic field assisted quench was proposed for building a 110 kV/1.8 kA prototype [17]. Based on CURL 10, Nexans has developed the first commercial medium voltage SFCL [23]. Two 12 kV resistive type SFCLs have been installed in Bamber Bridge (2009) and in Ainsworth Lane (2012) of the UK. Furthermore, a 12 kV/800 A SFCL was installed in the auxiliary power supply of a huge power plant in Vattenfall, in Germany [23]. Following the project of Vattenfall in Germany, another project named ENSYSTROB was also launched in the same plant to investigate the properties of a SFCL made of 2G HTS [24, 25]. The project aims to compare the two SFCLs made of different superconducting materials with respect to limitation behaviour, AC losses and recovery time. Additionally, within the European project ECCOFLOW, a resistive SFCL built with 2G HTS was developed for the first time for two different locations--one as a bus bar coupler in a substation of Spain and the other one in the transformer feeder in Slovakia [26, 27]. In 2012, the first Italy’s resistive type SFCL with specification 9 kV/3.4 MVA was installed in A2A S. Dionigi substation [14]. This SFCL operated in the power grid successfully for more than one year [14].

Besides Europe, United States (US) has also conducted significant research concerning resistive SFCLs. A US Department of Energy (DOE) funded project, which is led by American Superconductor Corporation (AMSC), has designed a 115 kV SFCL for power transmission with low inductance pancake module made of

2G HTS tape [28]. Initial tests such as current limiting property, AC losses and the termination and high voltage tests validated the design. Based on 2G HTS, SuperPower Inc. has built modules for superconducting fault current limiters, which makes it possible to scale up the operational voltage to transmission level, such as 138 kV [29]. It is worth noting the SuperPower's design offers Recovery Under Load (RUL), which means the quenched device is capable of recovering to superconducting state while carrying load current. However, there is no report concerning the implementation of this design in a real power grid.

In addition, Asian countries such as China and Japan have also focused on the research concerning resistive type SFCLs. In 2012, a 10 kV/200 A SFCL based on 2G HTS tape was built and tested by Shanghai Jiaotong University[13, 30]. In 2013, the SFCL was connected to a 10 kV grid in Shanghai for trial operation [30]. Under the Super-ACE project, Japan has developed two types of SFCLs: one is a 6.6 kV resistive type superconducting fault current limiter and the other one is a 66 kV/750 A rectifier type fault current limiter, which combines rectifier bridge circuit and HTS coil made of Bi2223 tape. Laboratory tests were completed on the two types of SFCLs and there was no report on their application in a power grid [31]. Following the Super-ACE project, a 6.6 kV/600 A SFCL based on coated conductors was also developed and successfully tested and installed in a user field [32].

2.1.2 Saturated iron core SFCL

1) Working principle

The saturated iron core SFCL is composed of two iron cores, a DC superconducting coil and two AC windings, which are wound around the iron core as shown in Figure 2.3. The principle of the saturated iron core SFCL is the control of the inductance of the SFCL by changing the saturation state of the iron core. During normal operation, the DC current provided to the DC superconductor coil generates a magnetic field, which drives both iron cores into saturation. The AC current in the AC winding is so small that it is unable to change the saturation state of the iron core. However, in the case of a fault, the high fault current can drive the two iron cores out of saturation and into the region of high permeability, leading to a significant increase of the inductance of AC windings [11].

2) Advantages and disadvantages

In saturated iron core type SFCL, there is no quench in the current limiting process, leading to continuous operation without the need to wait for recovery. Furthermore, since the superconductor is operating in DC mode, instead of AC mode, there are no AC losses during its normal operation and smaller amount of superconductors is needed for the DC coil. Another advantage of this type of SFCL is that the current limiting capacity is adjustable via the change of the DC bias.

For saturated iron core fault current limiters, the main disadvantage is the massive use of iron cores, which results in large size, heavy weight and high cost [33]. Additionally, high voltage might be induced in the DC superconducting coil, which might damage the current supply of the DC bias [33].

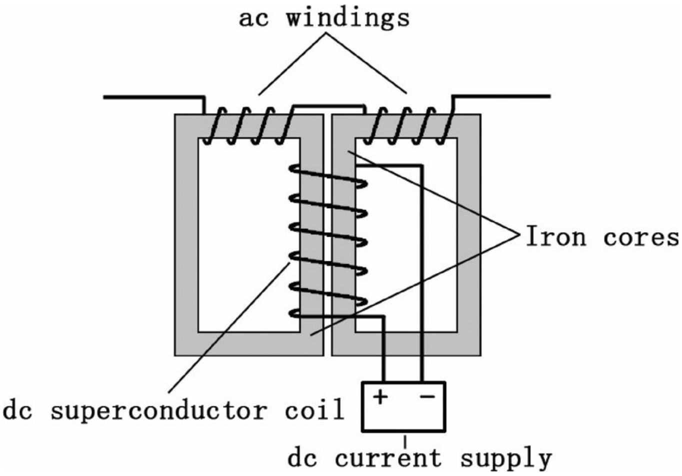

Figure 2.3 Structure of saturated iron core superconducting fault current limiter [33]

To address these problems, different methods have been proposed. One is the use of innovative iron core structure [33], where the vertical limbs of the six iron-core frames are arranged together to form the central column. This improvement not only decreases the volume of the device, but also minimises the inductive voltage induced in the DC coil during normal operation. To protect the DC current supply from the risk of high voltage in the case of a fault, a method of rapidly breaking the DC circuit is proposed [33]. This is realised with a magnetisation control circuit. In the case of a fault, a circuit control unit will send a signal to the fast switch, which is connected in series with the DC coil and DC current supply, to interrupt the DC circuit. Subsequently, the magnetic energy stored in the iron core is then released through the energy release unit. With this method, the risk of the induced high voltage to the DC current supply is avoided and the limitation function of the device is also improved greatly, since both AC coils contribute to the limitation of fault current.

3) Summary of saturated iron core type SFCL projects

For this type of SFCL, the US and China have developed prototypes and installed them in the power grid for trial operation. In America, Zenergy has installed a 15 kV/1.2 kA three-phase saturable core SFCL at SCE’s Shandin substation [34]. Based on the experience gained on the 15 kV SFCL, Zenergy is planning to develop new versions of the saturable core SFCL for application at medium (69 kV) and transmission (138 kV) voltage levels [34]. In China, a 35 kV/90 MVA saturated iron-core type SFCL was developed, tested and installed in a transmission network at Puji substation of China Southern Power Grid for live-grid operation in 2007 [15]. In the design, two main improvements were made: an innovative design in the iron-core configuration and a magnetisation control circuit. Subsequently, based on the success of the 35 kV SFCL, an 220 kV/300 MVA SFCL was also developed and installed in the Shigezhuang substation in Tianjin, China [12].

2.1.3 Bridge type SFCL

1) Working principle

A bridge type SFCL, which is also called a DC reactor type or rectifier type SFCL, consists of thyristors or diodes arranged as a full bridge rectifier, a limiting coil usually made of superconducting material and a voltage source, as shown in Figure 2.4.

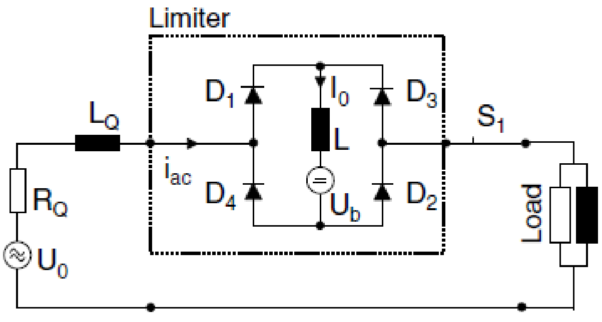

Figure 2.4 Electric circuit of a diode bridge type SFCL [11]

Under normal operation, the AC current amplitude is lower than the DC current produced by the voltage source, thus all the diodes/thyristors are conductive and the AC current flows through the diodes only. However, when a fault occurs the amplitude of the AC current exceeds the DC current, shutting D3 and D4 or D1 and D2, and the AC current therefore limited by the inductance L. The concept was firstly proposed by Boenig and Paice [35]. Different improved types of SFCL have been proposed by introducing a parallel combination of resistor and switch, which are connected in series with the superconducting coil to increase the current limiting capability of these types of SFCLs [36-38].

2) Advantages and disadvantages

For the bridge type SFCL, there is no quench in the superconductors, therefore the SFCL can be used continuously without interruption. Furthermore, since the trigger current is adjustable, the SFCL can be easily used for different applications with different fault currents. However, this type of SFCL is not fail-safe, which is its main disadvantage. For example, once a semiconductor fails, the SFCL cannot be used.

3) Summary of saturated iron core type SFCL projects

To date, several bridge type SFCLs have been developed in Asia and all of them are based on low voltage levels. In China, a 10.5 kV/1.5 kA three phase improved rectifier-type fault current limiter has been installed in a real 10.5 kV substation located in Hunan [37]. In Japan, a 6.6 kV/36 A single-phase, rectifier type SFCL was fabricated and tested in the laboratory [36]. Similarly, a three-phase, 6.6 kV/200 A DC reactor type SFCL was also developed and tested in Korea [39].

2.1.4 Shielded iron core type SFCL

1) Working principle

An inductive type SFCL, which is also called the shielded core type SFCL [11] and transformer type SFCL, is composed of an iron core, the protection circuit and a closed loop superconducting element [11, 40]. Both the protection circuit and the superconducting element are wound around the iron core, thus forming a transformer with the secondary side short-circuited.

During normal operation, the screening current generated in the superconducting element completely cancels the flux in the iron core, leading to a negligible limit to the normal current. However, when a fault occurs, current higher than the critical current of the superconductor is generated, which quenches the superconductor and generates limiting resistance in the protection circuit.

2) Advantages and disadvantages

The advantage of the inductive type SFCL is the magnetic field connection between the protection circuit and the superconducting elements, thus no current leads are needed for the superconducting element. Similar to the saturated iron core type SFCL, the use of the iron core leads to large volume and weight. Furthermore, after the quench of the superconductor, a recovery time of several seconds is needed before its reoperation in power grid.

3) Summary of saturated iron core type SFCL projects

Two demonstrators of the inductive type SFCLs were built and tested in the 1990s. In Switzerland, a 10.5 kV/70 A three-phase prototype limiter was developed by ABB by using BSCCO 2212 cylinders and installed in a Swiss hydropower plant in 1996 [41, 42]. In Japan, Central Research Institute of Electric Power Industry (CRIEPI) built a single-phase 6.6 kV/400 A SFCL in 1997 that also used BSCCO 2212 cylinder [43, 44].

2.1.5 Hybrid type SFCL

1) Working principle

A hybrid type SFCL has been proposed to decrease heat generation in the superconductor and provide the off-line recovery time for the superconductor. For this type of SFCL, different designs have been proposed [45-50]. In order to decrease the AC losses of the SFCL, a hybrid type SFCL, where a resistive SFCL connected in parallel with a fast opening load switch was proposed in Switzerland [45]. During normal operation, the current flows through the fast opening load switch only and in the case of a fault the current is commutated into the superconducting path by the switch [45]. In Japan, a hybrid SFCL, which contained a superconducting element, a vacuum circuit breaker and a parallel coil was proposed [46]. When a fault occurs, the vacuum interrupter is driven by the magnetic field generated in the parallel coil at the same time as quench[46]. Thus, the superconductor element serves as a trigger and the parallel coil is used as the limiting impedance. In Korea, several novel kinds of hybrid type SFCLs, which combine superconductors and conventional electrical equipment were proposed and developed [47-50]. The common characteristic of these different hybrid type SFCLs is that a fast switch is used to transfer the current from the superconductor to the traditional equipment when a fault occurs.

2) Advantages and disadvantages

The advantage of the hybrid type SFCL is that a superconductor is not used for limiting fault current during the fault, thus there is no quench and recovery of the superconductor. However, the system tends to be somewhat complicated and it is problematic when scaled to transmission voltage levels.

3) Summary of hybrid type SFCL projects

Several hybrid type SFCLs have been developed and some of them have been installed in power grid for trial operation. A novel hybrid SFCL, which combined a superconductor and conventional electrical equipment including a vacuum interrupter, power fuse and current limiting reactor, was proposed and developed by LSIS and KEPRI, as shown in Figure 2.5 [49]. Furthermore, a 22.9 kV/630 A hybrid type superconducting fault current limiter, which was developed by Korea Electric Power Research Institute (KEPCO) and LS Industrial System Co., Ltd (LSIS), was installed on a distribution line in Icheon Substation for real-grid operation [51, 52].

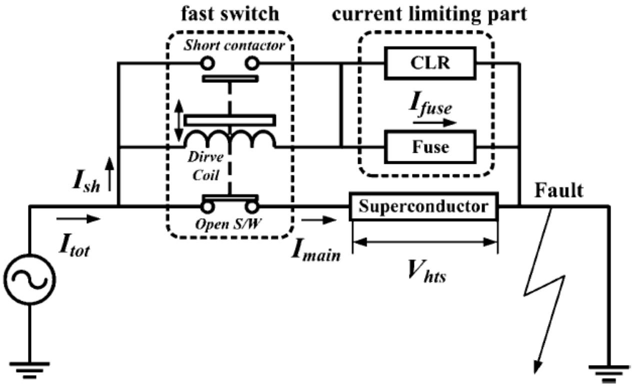

Figure 2.5 A Novel Hybrid Type Superconducting Fault Current Limiters [49]

2.1.6 Summary of SFCL projects

Besides the above five types of SFCLs, there are also some other types of SFCLs such as the flux lock type and the resonance circuit type. However, due to the comparatively lower levels of R&D effort, these are not covered in this chapter. To provide an overview of SFCL projects development, detailed information of different SFCL demonstrators developed across the world are summarised in Table 2.1.

Table 2.1 Summary of SFCL projects around the world

Leader company/project	Country/year	Type	Data	SC material
ACCEL Instruments GmbH	German/2004	Resistive	10 kV/10 MVA	BSCC0-2212
Nexans	UK/2009	Resistive	12 kV/100 A	BSCCO-2212
Nexans	Germany/2009	Resistive	12 kV/800 A	BSCCO-2212
Nexans/ENSYSTROB	Germany/2011	Resistive	12 kV/533 A	YBCO
Nexans/ECCOFLOW	Spain/2013	Resistive	24 kV/1005 A	YBCO
Nexans/ECCOFLOW	Slovakia/2013	Resistive	24 kV/1005 A	YBCO
Nexans	UK/2012	Resistive	12 kV	BSCCO-2212
Shanghai Jiaotong University	China/2012	Resistive	10 kV/200 A	YBCO
Toshiba/METI	Japan/2009	Resistive	6.6 kV/600 A	ReBCO
RSE	Italy/2012	Resistive	9 kV/3.4 MVA	BSCCO
Zenergy	USA/2009	Saturable core	15 kV/1.2 kA	BSCCO
Innopower	China/2007	Saturated iron-core	35 kV/90 MVA	BSCCO
Innopower	China/2012	Saturated	220 kV/300	BSCCO

		iron-core	MVA	
Chinese Academy of Sciences	China/2004	Rectifier-type	10.5 kV/1.5 kA	Bi-2223
ABB	Switzerland/1996	Shielded core type	10.5 kV/70 A	Bi-2212
LSIS	Korea/2012	Hybrid type	22.9 kV/630 A	YBCO

2.2 Main challenges in the application of resistive type SFCLs

Based on the review of the different types of SFCLs, the resistive type SFCL has been the most popular and promising SFCL to date. Therefore, this thesis focused on the research of resistive type SFCLs. For the application of the resistive type SFCL in power grids, there are several challenges and limitations such as current limiting performance, AC losses, insulation and volume limit.

The current limiting performance is the first important property to be considered in the design process of a SFCL. Generally, the superconducting element should react fast to limit all kinds of fault currents, which means the critical current of the SFCL should be lower than the minimum fault current amplitude. Furthermore, superconductor quench is not expected in case of transient currents of a power grid such as the starting current of motors and inrush current of transformers [19]. Therefore, the critical current of SFCL should be higher than these transient currents.

Another challenge in the current limiting process of a SFCL is the hot spot problem, which is mainly because of the inhomogeneous current density distribution and the low velocity of normal zone propagation in high temperature superconductors. To cope with this problem, different methods have been proposed. The concept of a current flow diverter, which insets a highly resistive layer between the superconducting and stabiliser layers, to accelerate the normal zone propagation velocity, has been proposed and numerically verified [53]. Based on the analytical study of Tixador, decreasing the superconductor resistivity can effectively weaken the maximum temperature at the hot spot in the case of a fault [19]. Besides, the magnetic field assisted quench propagation has also been proposed and used in improved resistive type SFCLs [17]. In this novel concept, a normal conducting coil is wound around and electrically connected in parallel with a superconducting tube. Therefore, local quench will shunt current to the coil, which generates a strong magnetic field to quench the superconducting element rapidly and homogeneously [17]. In addition, different simulation models were developed for simulating the current limiting performance of SFCLs, which are summarised in Section 2.3.2.

The extent of AC losses in SFCLs is another important property to be considered in the design of SFCLs. Lower AC loss is preferable to decrease the cooling power consumption, thus reduce the requirement of the cooling system and lower the maintenance costs. The AC losses of a superconductor are mainly composed of two parts: hysteresis loss in the superconducting layer and the ferromagnetic loss in the magnetic substrate. The latter only exists in superconductors with a magnetic substrate such as Ni-5at%W. To decrease the AC losses, bifilar pancake coils have been proposed [54], which is advantageous for its compactness and low AC losses. Experimental and numerical studies show that the AC losses of bifilar pancake coils made of IBAD tapes are lower than that of simple pancake coils and the single-tape loss [55, 56]. While for RABiTs tape, studies show that the front-to-front anti-parallel HTS tape configuration can results in the lowest losses compared with that of the back-to-back configuration [56]. Based on these studies, concerning the impact of magnetic substrate on the AC loss of superconductors, AMSC proposed a novel type superconductor tape named Type 8612, where two HTS/substrate insert structures placed back-to-back are used in the wire. This type of superconducting wire not only increases the critical current of a single wire, but also decrease the impact of the magnetic substrate on the magnetic field distribution, thus decreasing the AC losses [29].

The volume limit of SFCLs is another aspect that challenges the application of SFCLs. SFCLs are usually installed in substations, where there is limited space, especially for substations in urban areas. A complete SFCL system includes a superconducting element, electrical bushing, shunt impedance or reactors, cryogenic dewar and a cooling system. To decrease the occupied space of SFCL, the superconducting element should be arranged densely. However, excessively dense arrangements might lead to an insulation problem. An insulation problem mainly results from the fact that the superconducting element withstands most of line voltage during the fault period. For the bifilar pancake type SFCL, the total SFCL voltage is concentrated on the two ends that are adjacent to each other, as shown in Figure 2.2. Similarly, the voltage is also concentrated on the ends of the non-intersecting type coils. For both kinds of SFCLs, when the operating voltage is scaled up, the insulation problem is more severe. However, for the braid type SFCL and the straight line type SFCL, this problem can be avoided since the voltage is applied to the top end and bottom end, which are relatively far away from each other.

2.3 Simulation of resistive type SFCLs

For applying SFCLs into power grids, simulation studies are necessary and economic for understanding the basic physical principles, monitoring the operational status and also optimising the design of the devices. From the point view of device operation, there are two aspects of simulation that are paramount and essential: the AC losses and the current limiting process.

2.3.1 Simulation of AC losses

Generally speaking, the simulation of the AC losses of superconducting devices can be classified as the electro-magnetic property simulation of superconductors, which has been a popular topic for several decades. Considering that this thesis mainly focuses on the SFCLs made of 2G HTS, only the simulation work concerning thin film superconductors are summarised here.

The simulation of hard superconductors is challenging for several reasons. Firstly, the nonlinear *E-J* characteristics of superconductors makes the calculation difficult to converge, especially for 2G HTS, whose *n* value (*n* value describes the relationship of the voltage drop across a superconductor to the applied current) can reach as high as 50 [57]. Secondly, the high aspect ratio of the superconducting layer leads to a large mesh size, making the calculation cumbersome. Various methods have been developed for simulating HTS tapes, tape stacks and coils, which can be mainly divided into three categories—analytical, integral and differential methods.

In 1969, Norris proposed two analytical methods for calculating the AC losses of hard superconductors with different shaped cross-sections such as ellipse, rectangular, cruciform and box [58]. Brandt extended the Norris model to the electro-magnetic calculation of type-II superconductor strip [59].

Regarding the integral method, Clem first proposed a theoretical framework for estimating the AC losses in a finite Z stack using anisotropic homogeneous-medium approximation [60]. Yuan et al extended the model by replacing the frontier with a quadratic function and introducing the magnetic field dependence of J_c [61-63]. Prigozhin proposed a free-marching numerical scheme based on magnetic vector potential formulation, which can be used for the numerical solution of critical-state problems with arbitrary current-voltage laws [64]. Subsequently, Pardo et al. simulated the electro-magnetic properties and AC losses of pancake coils and stacks of pancake coils by using the minimum magnetic energy variation (MMEV) method, which minimises the magnetic energy variation of superconductors [65-67].

Furthermore, the differential method has also become an attractive choice for simulating electro-magnetic properties of high temperature superconductors, mainly because of their easy realisation with commercially available software packages such as COMSOL and FlexPDE. Generally, there are three types of finite element method (FEM) that have been proposed for solving Maxwell equations: $\boldsymbol{A}$-V ($\boldsymbol{A}$ and V are the magnetic vector and the electric scalar potential) [68, 69], $\boldsymbol{T}$-Ω ($\boldsymbol{T}$ and Ω are the current vector potential and magnetic scalar potential) [70, 71] and $\boldsymbol{H}$ formulations ($\boldsymbol{H}$ is the magnetic field strength) [72, 73], which are defined based on the corresponding variables to be solved. Recently, with thin strip approximation, Zhang proposed an efficient three-dimensional (3-D) FEM model based on a $\boldsymbol{T}$-$\boldsymbol{A}$ formulation, which works well for the 3-D simulation of devices made of coated conductors [74, 75].

2.3.2 Simulation of current limiting performance

Simulation of the current limiting process is paramount to the design of SFCLs, which makes it possible to study whether the fault current can be limited to the expected value and how the superconductor reacts in the case of a fault. Both questions are concerned by the SFCL designers and the distribution network operators. So far, two different kinds of method have been popularly used for simulating the current limiting performance of SFCLs—FEM and the lumped circuit method.

Similar to the simulation of AC losses, FEM has been one of the most popular methods for the simulation of the current limiting performance of SFCLs. Based on this method, the detailed electro-magnetic properties of superconducting devices can be obtained, however, this method is usually time-consuming due to the large mesh size and the non-linear *E-J* characteristics. F. Roy proposed a 2-D electro-magneto-thermal model, which was calculated with *H*-formulation, to simulate the quench performance of superconductor tape. The increase of the thickness of each layers of a superconductor, aiming to speed up calculation, might result in inaccuracy of the calculation result [76, 77]. Similarly, a 2-D axi-symmetric model using H formulation was proposed to calculate the quench propagation of superconducting coils in the case of heat pulses [78, 79]. In the model, a simplified superconductor model was used by deleting the silver and buffer layers to enable faster calculation.

Besides these 2-D FEM models, several 3-D FEM models have also been developed to investigate the current limiting process of SFCLs. J. Duron proposed a 3-D FEM model to study the quench behaviour of the superconductor with a method based on a fast-forward scheme, where the electro-magnetic model and thermal model are calculated alternately. In the simulation, the geometric aspect ratio was decreased by increasing the thickness of YBCO and silver [80]. Another interesting 3-D micrometer-scale model was proposed by Wan Kan Chan, which coupled 2-D and 3-D models to simulate the quench propagation in both superconductor tapes and coils under DC conditions [81-83]. Furthermore, a hybrid model that combines the FEM and a current repartition Matlab function, has also been proposed [84].

The lumped circuit model is based on the idea of concentrating resistance, capacitance and inductance into idealised electrical components, i.e. resistors, capacitors and inductors, thus forming an electrical network with perfectly conducting wires. This method has also attracted great attention from both academia and industry. One of the typical and simple models of a SFCL is a variable resistor, which represents the superconducting element, in parallel with a fixed resistance, representing the metal layers of the superconductors. The variable resistor can be described with different kinds of *E-J* equations. Blair described the three states of superconductors with three exponential curves respectively [85]. Taxidor simulated the superconducting element with a current source ($\beta I_c(T)$) in parallel with a non-superconducting resistor [19], based on which he studied the preliminary design of

SFCLs. Due to the simplification of the SFCL model, all the work discussed above can provide analytical solutions for power system with SFCLs.

To get more detailed information during the quench period of a SFCL, numerical models are required. Tixador implemented the commonly used power law to describe the superconducting part of a SFCL [18], which enabled the model to study the impact of grid faults on inhomogeneous superconducting length. By using the thermal-electrical analogy to solve the heat transfer process in a superconductor, Sousa *et al*. proposed a lumped circuit model for simulating the electric and thermal behaviour of a SFCL [86]. Bonnard *et al*. extend this model to a multi-scale model with commercial software EMTP-RV, which made it possible to simulate not only the cross-section physical process, but also the length direction physical phenomenon, such as heat transfer and hot spot problems [87]. Furthermore, a SPICE model of high-temperature superconductor tape was also proposed based on a lumped circuit for the application to resistive SFCLs [88], where the superconductor element is taken as the parallel connected resistance of the substrate, the HTS layer and the stabiliser. Based on the simulation of a superconductor with electric elements, Morandi *et al*. modelled the coupled electromagnetic-thermal behaviour of a SFCL with an equivalent circuit model, which could be coupled with a power system model and used in evaluating the performance of SFCLs in power grids [89].

Chapter 3 Comparison study of two types of non-inductive solenoidal coils for SFCL application

Based on the literature review concerning SFCLs in Chapter 2, most of previous research work concerning SFCLs were focused on investigating resistive type SFCLs. Therefore, the technique concerning resistive type SFCLs is the most mature. Furthermore, the projects of resistive type SFCLs realised in power grids are also the most. Therefore, in this work, resistive type SFCL is selected as our research direction. Generally speaking, there are three types of structures that have been proposed for building resistive type SFCLs: straight line type [13, 90, 91], bifilar pancake type [92] and solenoidal type [16, 22], as discussed in Section 2.1.1.

To date, both straight line type and bifilar pancake type SFCLs built with 2G HTS tape have already been investigated comprehensively and systematically. However, there is still no systematic work for the solenoidal type of SFCL built with 2G HTS tape. Furthermore, considering most SFCL demonstrators are used in low and medium voltage levels, research concerning SFCLs for high voltage level applications becomes an essential and urgent task. For the application in high voltage level grids, braid type SFCLs might show better performance, considering most of the voltage is applied on the two ends of the coil, as analysed in Section 2.2. Therefore, it is necessary to study the overall performance of non-inductive solenoidal type SFCLs to understand their applicability in high voltage level applications.

In this chapter, an experimental comparison is performed on two types of low-inductance solenoidal coils (non-intersecting type and braid type) to study their overall characteristics for SFCL applications in this chapter. The tests performed include resistance measurement, current limiting property test, recovery time measurement and AC losses measurement.

3.1 Introduction of experimental samples

In this work, two prototypes of non-inductive solenoidal coils are built with SuperPower 2G HTS, as shown in Figure 3.1(a) and (c). The critical current, width and thickness of the Superpower tape are 120 A at 77 K, 4 mm and 0.21 mm respectively. More detailed parameters of the tape are shown in Table 3.1.

In the resistive type SFCL, the inductance of the SFCL should be designed to be as small as possible, to eliminate the impact of the SFCL inductance on the power grid in its normal operating state. In the non-intersecting type coil, as shown in Figure 3.1 (b), the two tapes are wound in the same direction and located in the same layer, with distances between the adjacent tapes the same. To cancel the inductance of the non-intersecting type coil, the two superconductor tapes are connected together at one end of the coil through two copper plates and two copper braids, as shown in Figure 3.1 (a). The copper plates are used as the interconnections between the superconductors and the copper braids. Additionally, the two copper braids are crimped together at a distance that are far from the coils (10 cm), which aims to eliminate the impact of the magnetic field generated by the copper braids connected to the superconductor tapes, as shown in Figure 3.1 (a). To decrease the impact of joint resistance on the critical current and AC losses measurement, only the superconductor voltage is measured during the experiments and the voltage taps are soldered at the superconductor ends, which are 2 cm away from the copper plates.

In the braid type coil, the two tapes are wound in opposite directions and connected in parallel, as shown in Figure 3.1 (c), thus to cancel the inductance of the SFCL. During the preparation of the prototype, an inner winding was firstly wound around the bobbin and Kapton tape was then wound around the inner winding. Finally, the outer layer was wound around the bobbin.

Table 3.2 summarises the detailed specifications of the two coils. It shows the two coils have the same radius and therefore generally the same superconductor length. However, due to the different winding methods, the two coils have different inductance. This also indicates that, compared with the non-intersecting type coil, the magnetic field in the braid type coil are better cancelled.

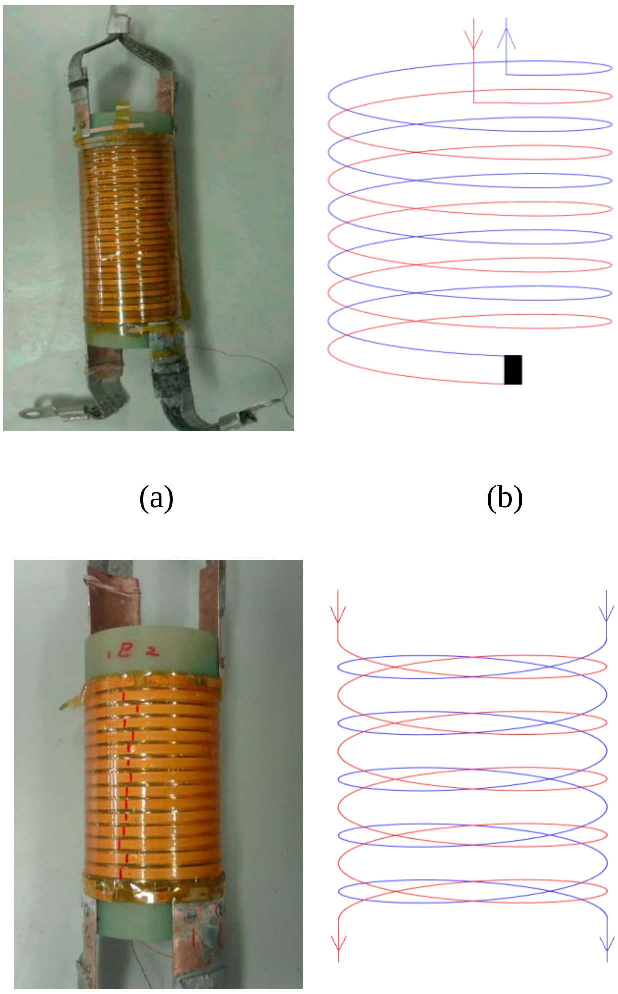

(a) (b)

(c) (d)

Figure 3.1 Experimental prototypes and the corresponding schematic diagrams: (a) the fabricated non-intersecting type coil (b) scheme of non-intersecting type winding (c) the fabricated braid type coil (d) scheme of braid type winding

Table 3.1 Parameter of the 2G HTS tape

Manufacturer	Superpower
Substrate	Hastelloy C-276 (50 µm)
HTS	YBCO (1µm)

Protective	Ag (2 μm)
Stabiliser	Copper (110 μm)
Minimum I_c	120 A

Table 3.2 Parameters of the solenoidal coils

	Non-intersecting type		**Braid type**	
	1st tape	*2nd tape*	*Inner layer*	*Outer layer*
Turns	15	15	15	15
Radius/mm	28.55	28.55	28.55	28.76
Pitch/mm	12	12	6	6
I_c /A	121	121	117	121
Inter-layer separation /mm	0		0.2	
Inductance/μH	1.47		0.86	

3.2 Introduction of experimental systems

3.2.1 AC losses measurement system

The AC losses of both prototypes are measured with the cancellation coil technique. The schematic diagram of the experimental system is shown in Figure 3.2. A power amplifier is used for transferring a weak AC signal generated by a signal generator into a strong AC signal with high voltage and low current. Subsequently, the strong signal is transformed to a high current low voltage signal by using an 18 kVA step down transformer with a voltage ratio of 400:6. Finally, the high current signal flows through the superconductor and a compensation coil, which are connected in series.

To measure the AC losses in the superconductor, both the current flowing through the superconductor and the resistive component of the superconductor voltage need to be measured during experiments. In the experimental system, for the measurement of current flowing through the superconductor, a FLUKE i2000 AC current probe was used for transferring the current signal to a voltage signal that can be acquired by the data acquisition card. For measurement of the resistive component of the superconductor voltage, the compensation coil was used to cancel the inductive component of the superconductor voltage. Then, the resistive component of the superconductor voltage can be obtained by connecting the superconductor voltage and compensation coil voltage in series, as shown in Figure 3.2. For both signals, the NI data acquisition card SCXI-1125 was used for acquiring the signals.

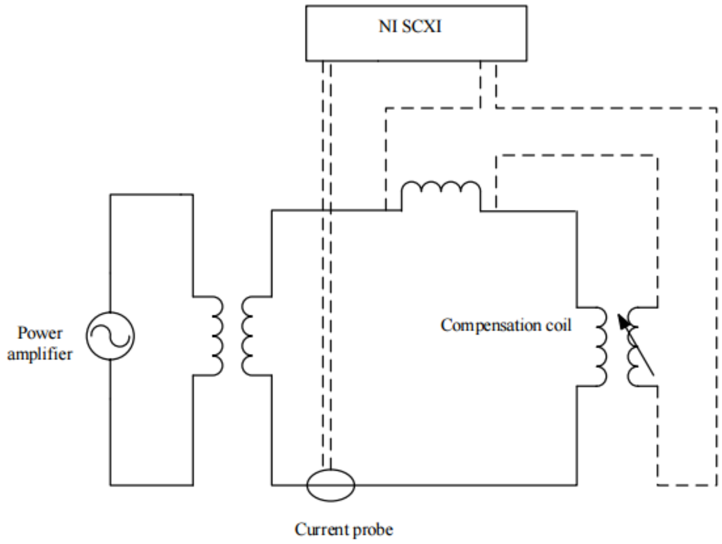

Figure 3.2 Schematic diagram of the AC losses measurement system

As introduced in Section 3.1, both SFCL prototypes comprise of two segments of superconductors. Therefore, to measure the AC losses of both prototypes, both voltage signals need to be taken into consideration. During the experiment, the total voltage of the solenoidal coils were measured with the addition method by connecting the two voltage signals in series [56].

For the non-intersecting type coil, the two segments of the superconductors were connected in series, therefore, the current in the two segments were the same. However, for the braid type coil, the two superconductor windings are connected in parallel and the current in each superconductor was impacted by many factors, such as the inductance of the superconductor and the contact resistances, which makes it difficult to measure the total AC losses. As a result, to obtain an approximate measurement, the two windings of the braid type coil were connected in series with a copper braid, which forces the current in the two windings to be equal. With this method, it was possible to measure the AC losses of the braid type coil with the cancellation coil technique. On one hand, the impact of the contact resistance of both windings on the current distribution in the two windings is avoided successfully. On the other hand, the impact of inductances difference of the two windings on the AC losses is neglected, which will lead to error between the measured AC losses and the practical AC losses. However, considering the distance between two superconducting layers (0.2 mm) is negligible compared with the radius of G10 bobbin (28.55 mm), therefore, the inductance differences of the two windings can be neglected.

3.2.2 Fault current test system

In order to test the current limiting property and the recovery characteristics of SFCLs, a fault current test system was built in this work, as shown in Figure 3.3. The system is composed of an autotransformer, a step-down transformer, a line resistor, a load resistor, a Siemens circuit breaker and a SFCL prototype. The specification of each element is introduced below.

1) For the autotransformer, an 18 kVA/400 V autotransformer was used. For the step-down transformer T2, an 80 KVA/400 V transformer that can provide a short circuit current of 3200 A for 0.1 seconds under 250 V output voltage was chosen. Furthermore, there were eight taps on the secondary side of the step-down transformer T2, which corresponds voltage levels of 5, 10, 25, 50, 100, 150, 200, 250 V respectively.
2) For the circuit breaker, a SIEMENS 3VT3 molded case circuit breaker (MCCB) was chosen. In the fault period, the MCCB should be switched on firstly and then switched off after 0.1 s. Under such high requirement, remote electronic control is needed. To switch on the MCCB remotely, a motorised operating system was used. To switch off the circuit breaker remotely, a shunt opening release was used. With the two elements, the opening and the closing operation can be finished in 50 milliseconds, which make it possible to control the fault period.
3) For the line resistor, resistors with different resistances were chosen.
4) For the load resistor, the resistance was 4.25 Ω.
5) To realise data acquisition, system monitoring and remote control of the experimental system, the NI PCI 6232 data acquisition card was chosen.

During normal operation, S1 is open and current flows though the line resistor, load resistor and the SFCL. In this situation, the system current is smaller than the critical current of the SFCL. Therefore, the SFCL is in the superconducting state. In the case of a fault, S1 is closed and short-circuits the load resistor R_L, generating fault currents in the system. The fault current is much higher than the critical current of the SFCL and thus quenches the SFCL. Finally, the circuit breaker is switched off again to clear the fault current, when the recovery characteristics of SFCL can be measured by measuring the resistance or the temperature of the SFCL.

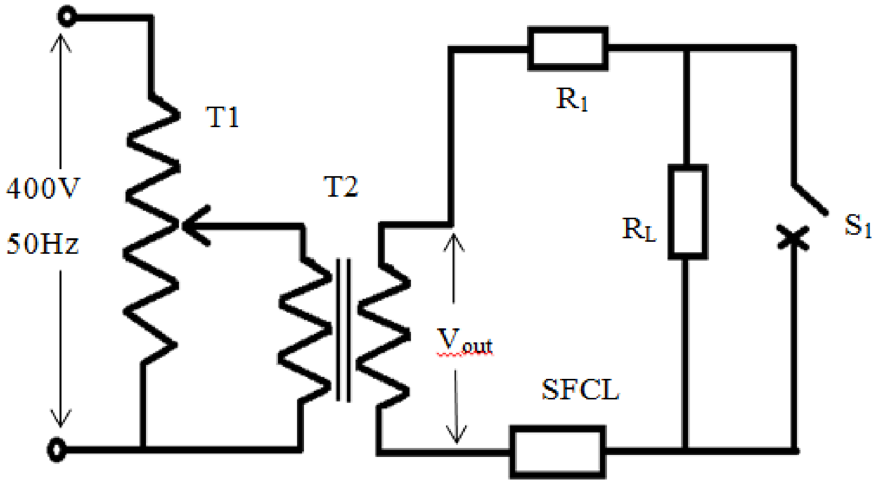

Figure 3.3 Schematic diagram of the experimental system

To mimic the real faults, different prospective fault currents need to be generated with a constant AC source voltage combined with variable line resistors principally. However, to simplify the experimental process in this work, variable source voltages combined with a constant line resistor were used to generate different prospective fault currents.

The constant line resistor R1, which was 3.14 mΩ, is used here to control the limited fault currents in case of a fault. The variable source voltages are realised by combining the autotransformer and the step down transformer.

Considering different connection methods of the two prototypes (the non-intersecting type coil is connected in series, while the braid type is connected in parallel) and that the tape lengths in each winding were approximately the same, the voltage across the non-intersecting type coil should be about twice of that across the braid type coil, to guarantee the same electric field being applied on the superconductors of the two prototypes during the fault test.

3.3 Experimental comparison of two types of non-inductive solenoidal coils

3.3.1 Comparison of the current limiting properties

By using the experimental system introduced in Section 3.2.2, the current limiting properties of the two prototypes in Figure 3.1 were tested and compared. In the experiments, the fault period was set to be 0.1 s, equalling five cycles with frequency 50 Hz. Furthermore, the transformer output voltage, the voltages of the superconducting windings and the current of the SFCL were all measured. After the quench period, the winding voltage was still recorded for analysing the recovery characteristics of the SFCL.

In the experiments, it is quite difficult to keep the output voltage of transformer T2 constant in the experiment, especially for the test of the braid type coil. This is mainly because of the fact that the total impedance of the transformer T1 and T2 is comparable to that of the SFCL after quench, which decrease the voltage withstood by the SFCL and results in a large voltage drop when a fault occurs. Therefore, the SFCL voltage (RMS value) in the last half cycle is taken as a reference for comparison of the current limiting properties. The experimental test results of the braid type coil and the non-intersecting type coil are shown in Table 3.3 and Table 3.4 respectively. Due to the different coil connection methods, the resistance of the non-intersecting type coil is about 4 times of that of the braid type coil at room temperature. This indicates that the current limiting capability of the non-intersecting type coils should be four times that of the braid type coil under the same quench extent. Considering the electric field on the superconductor is the key factor that determines the quench degree, therefore, the average electric field should be used as the reference when the current limiting properties of the two coils are compared.

Table 3.3 Braid type coil

Rated voltage of superconductor/V	Prospective fault current/ A_{rms}	Limited fault current/A_{max}	Current limiting ratio
2.6	828	506	2.30

4.2	1338	608	3.11
6.02	1918	671.6	4.04
7.88	2510	724.6	4.89
12.67	4035	836.7	6.82

Table 3.4 Non-intersecting type coil

Actual voltage of superconductor/V	Prospective fault current/ A_{rms}	Limited fault current/A_{max}	Current limiting ratio
6.40	2038	264	10.92
11.72	3732	303	17.41
15.21	4844	340.8	20.10
18.40	5860	372.6	22.24
26.98	8592	404	30.07
38.28	12190	438.54	39.30
51.77	16487	438.34	53.18

Figure 3.4 illustrates that the current limiting ratio of the two coils verses the electric field, which shows that the current limiting ratio (CLR) of the non-intersecting type coil is just four times of that of the braid type coil. This indicates that the two coils show consistent quench and current limiting properties under different electric fields.

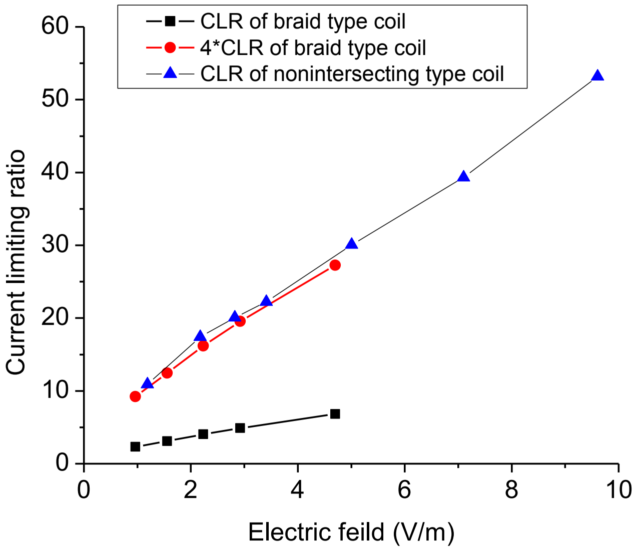

Figure 3.4 Comparison of the current limiting ratio of the braid type coil and the non-intersecting type coil

Figure 3.5 (a) and (b) compares the prospective fault current and the limited fault current for the braid type coil (under an external voltage of 12.67 V) and the non-intersecting type coil (under an external voltage of 24.54 V) separately, which shows that both coil types can limit the fault current effectively. For the non-intersecting type coil, the limited fault current is 396.09 A, which corresponds to a current limiting ratio of 27.84. For the braid type coil, the limited fault current is 836.7 A, which corresponds to a current limiting ratio of 6.82, which is one quarter of that of the non-intersecting type coil.

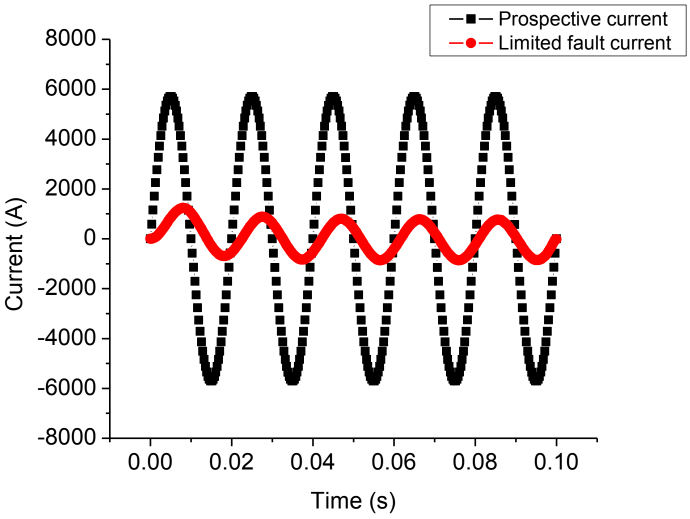

(a) The braid type coil

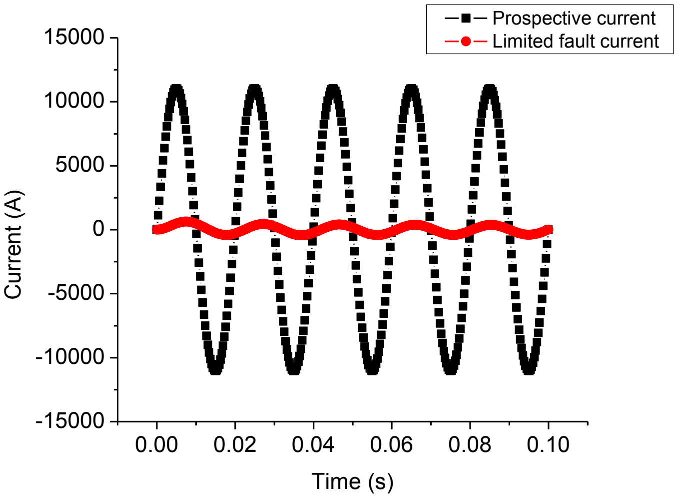

(b) The non-intersecting type coil

Figure 3.5 Prospective and limited fault currents: (a) braid type; (b) non-intersecting type

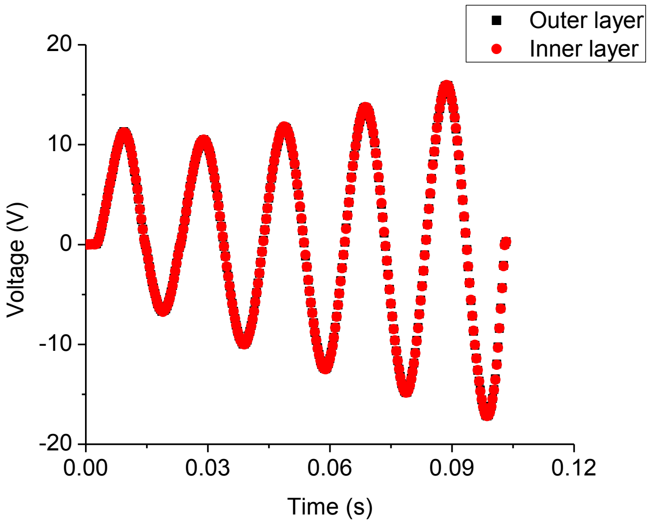

(a) The braid type coil

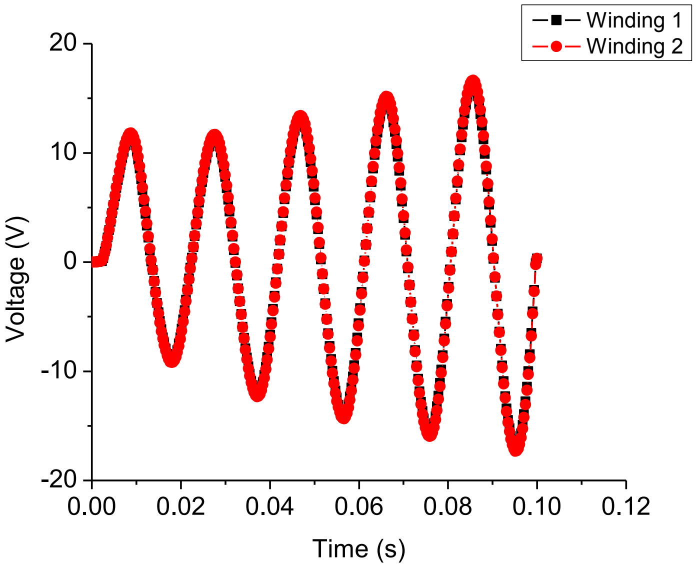

(b) The non-intersecting type coil

Figure 3.6 The voltage change during the quench period of both types of coils: (a) the voltage changes of the two tapes of the braid type coil, (b) the voltage changes of the two tapes in the non-intersecting type coil.

Figure 3.6 indicates that for both types of coils, the quench in the two windings are quite uniform during the quench period, which is paramount to the SFCL because the non-uniform quench easily leads to the generation of hot spots and subsequent burning of local superconductors. The uniform quench can be attributed to two reasons. On one hand, the thick copper stabiliser tends to increase the stability of the superconductor in withstanding different kinds of fault currents, based on the theory of Tixador [19]. On the other hand, the non-inductive structure of the braid type coil tends to accelerate the quench consistency of both windings in the coils. For example, the quench in the local segment of the first winding will result in a current increase in the second winding, which leads to the increase of magnetic field generated by the coil. The increase of magnetic field will lead to the decrease of the critical current of the superconductor and accelerate the quench process of the whole coil.

3.3.2 Comparison of recovery characteristics

Recovery time is another important characteristic of SFCLs. The recovery time is defined as the duration from the end of a system fault to the moment when a superconductor is restored to the superconducting state. In the operation of SFCLs, the shorter the recovery time, the faster that SFCL can be put back into operation, which decreases the impact of system faults on the power grid and thus is benefit to the continuous and stable operation of a power grid.

For the recovery time measurement, different definition and measuring methods have been used in previous research works. Firstly, it is defined as the period between the end of a fault and the time when the temperature of a SFCL decreases to the temperature of liquid nitrogen (77.4 K) [93]. Another method for measuring the recovery time is the period from the end of a fault to the time when the DC voltage of a superconductor decreases to zero. In this method, a small DC current signal is provided to the SFCL after the end of a fault, which makes it possible to measure the SFCL voltage [81]. Finally, the recovery time has also been defined as the minimum time interval between a fault event and the reapplication of nominal current without a detectable voltage [94].

In this chapter, the recovery time of the experimental samples was measured by recording the AC voltage signal of the superconducting windings after the fault period. In this method, a current that is far lower than the fault current is applied to the SFCL after faults, which makes it possible to measure the trend of the SFCL voltage. As shown in Figure 3.7, the recovery time is taken as the time difference between the end of a fault and the time when the voltage of the SFCL drops to zero. This definition is similar to the definition of the DC voltage measurement method.

Both definitions are based on the assumption that the small current applied to the SFCL after the clearance of the fault is far smaller than that during the fault. Therefore, the heat generation due to the small current is negligible compared to that during the fault period.

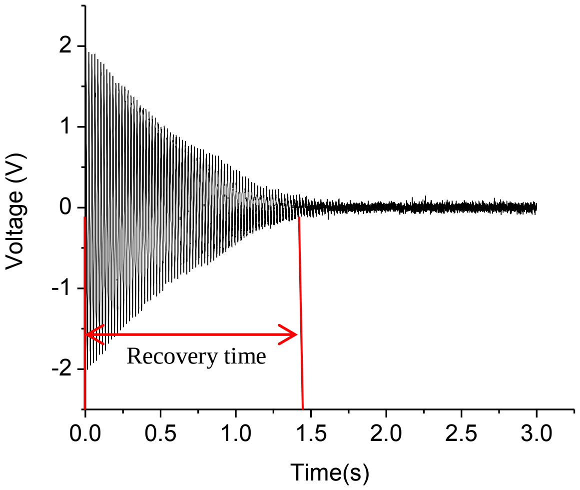

Figure 3.7 Schematic diagram of calculation of recovery time

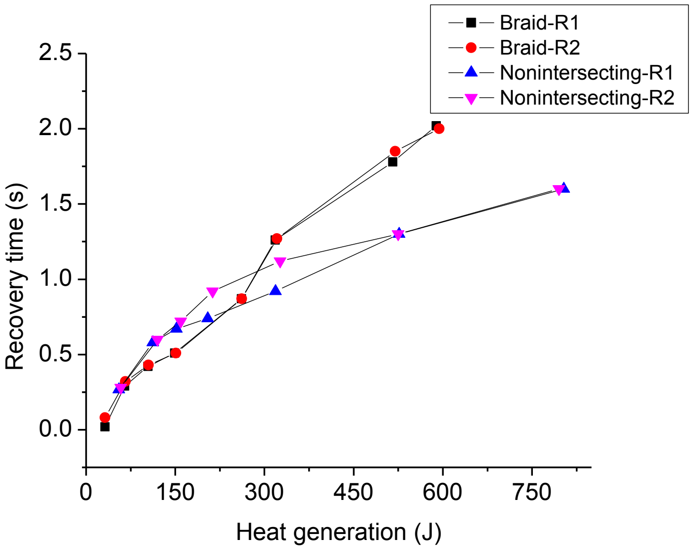

Figure 3.8 The recovery time of the braid type coil and the non-intersecting type coil. For the braid type coil, R1 and R2 mean the outer winding and the inner winding respectively

Based on the analysis in Section 3.2.2, both the voltage and current of the two types of non-inductive coils are variable during the quench period. Therefore, the heat generated (UIt) in each winding is taken as the reference when comparing the recovery time of both types of solenoidal coils, as shown in Figure 3.8. To distinguish the recovery time of the two windings in each solenoidal coil, the recovery times of both windings in the solenoidal coil are all calculated. Based on Figure 3.8, the following observations are made:

1) The recovery times of the two windings of the non-intersecting type coil are different when the generated heat is between 150 J and 520 J. However, the recovery time of the two windings of the braid type coil are always the same under different heat generations.
2) Under high fault levels, such as heat generated higher than 320 J, the recovery time of the braid type coil is longer than that of the non-intersecting type coil.

The first observation is relevant to the structures of both coils. In the braid type coil, the heat exchange between two windings is significant due to the overlapping structure between the inner and outer winding. This leads to little temperature difference between the inner and outer layer and thus, the recovery time is always the same. However, in the non-intersecting type coil, there is no heat conduction between the two windings because of the structure of the non-intersecting type coil. Therefore, the recovery time of the two windings can be different.

Another reason that might be relevant to the difference of recovery time of the non-intersecting type coil might be the non-uniform distribution of critical current. Due to the limitation of manufacturing technology, the critical current distribution cannot be strictly uniform. The non-uniform critical current distribution easily leads to the hot spot problems in a low voltage level fault, As discussed in [19, 95], which leading to the difference in recovery time.

The second phenomenon can be explained with the contact area between the superconductor and liquid nitrogen. For the two types of non-inductive solenoidal coils, the more contact area between the superconductor and liquid nitrogen, the faster the superconductor recovers. Compared to the non-intersecting type coil, there is an overlapping area between the inner winding and outer winding for the braid type coil, which leads to less heat transfer from the superconductor to the liquid nitrogen in a high level fault. Therefore, the recovery time of the braid type coil is much longer than that of the non-intersecting type coil under heat generation in windings higher than 300 J.

3.3.3 AC loss characteristics comparison

The AC losses of both types of solenoidal coils are measured with the AC loss measurement system, as introduced in Section 3.2.1. The detailed measurement results are shown in Figure 3.9. Figure 3.9(a) and (b) show the AC losses of the non-intersecting type and braid type coils respectively, under different frequencies of 70, 170, 270 Hz.

To provide a reference, the AC losses of a 40 cm long straight tape, which is the same with that in the solenoidal coils, is also measured here. As shown in Figure 3.9 (c), the AC losses of the non-intersecting type coil, braid type coil and the long straight tape are compared in detail.

Based on Figure 3.9, the following observations are made.

1) The AC losses measured at different frequencies are always the same for both types of coils, which validates the accuracy of the AC losses measurement method.
2) The AC losses of the braid type coil are about an order of magnitude smaller than that of the single tape, especially in low current regions when I_{rms} is smaller than 70 A. This is mainly because, in the low current range, the perpendicular magnetic field cancellation effect between the inner and outer layer dominates in braid type coils, which leads to a smaller penetration depth in the ends of the superconducting layers and thus lower AC losses. However, the magnetic field cancellation effect in the non-intersecting type coil is negligible due to relative far distance between adjacent tapes.
3) The AC losses curve of the non-intersecting type coil is very close to that of the single straight tape. This is mainly because the structure of the non-intersecting type coil leads to a similar magnetic field distribution and current density distribution to that in the long straight tape. Although the antiparallel structure between adjacent turns tends to increase the magnetic field as well as AC losses, the relatively large distance between adjacent

tapes (2 mm) weakens the magnetic field enhancement effect, thus leading to similar AC losses curves.

To understanding the underlying reasons that lead to these differences, especially the AC losses difference between the two types of solenoidal coils, more simulation work are needed. This will be explained and analysed in Chapter 4, where the electro-magnetic phenomena in both types of solenoidal coils and the current density distribution will be simulated and discussed in detail.

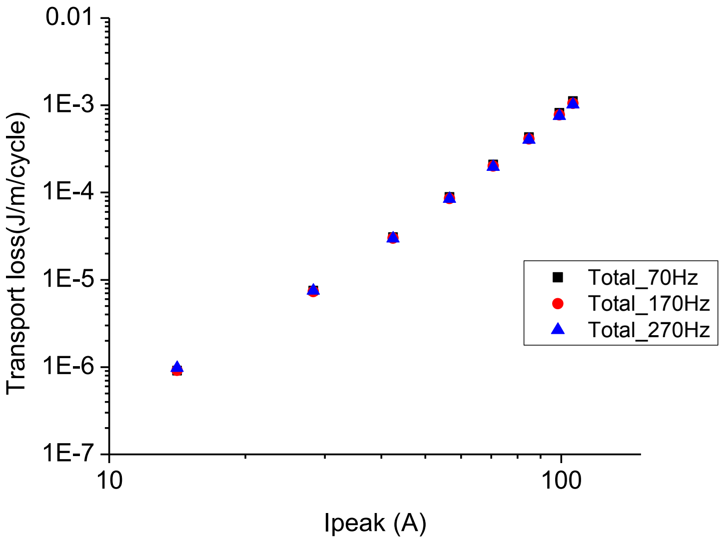

(a) Non-intersecting type coil

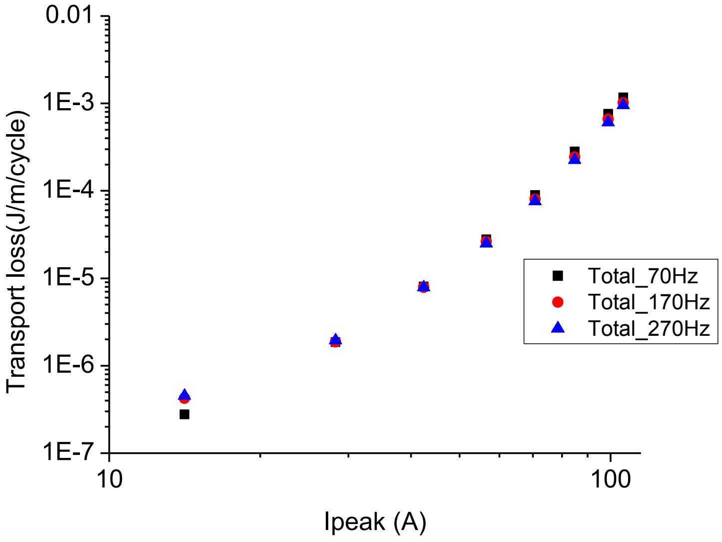

(b) Braid type coils

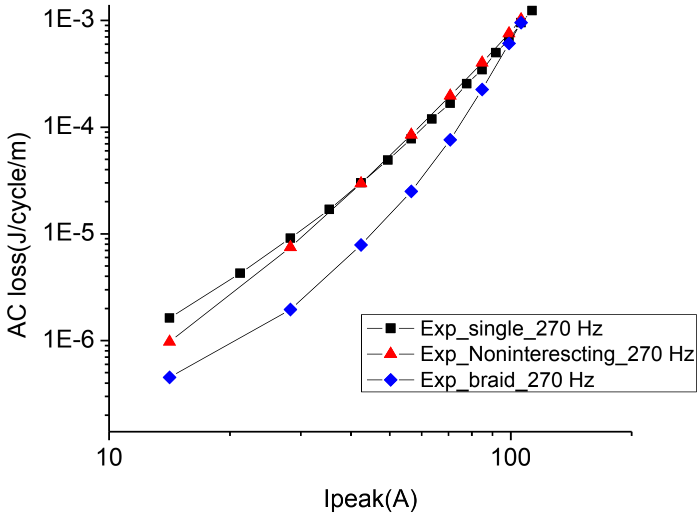

(c) AC losses comparison of two prototypes

Figure 3.9 Measured AC losses of two types of non-inductive soelnoidal coils and the single straight tape

3.4 Conclusions

To study the applicability of non-inductive solenoidal coils for SFCL use, two types of non-inductive solenoidal coils (non-intersecting and braid type) were built, tested and compared experimentally in this chapter. Based on these experimental works, the AC loss characteristics, current limiting properties and the recovery characteristics of both types of coils were compared comprehensively. Based on these experimental results and comparisons, the following conclusions can be generalised:

- Both types of coils can effectively limit different fault current. Due to the different connection methods, the current limiting ratio of the non-intersecting type coil is four times of that of the braid type coil. Furthermore, the quench consistencies in both types of coils are excellent.
- The recovery time of the braid type coil is longer than that of the non-intersecting type coil in conditions with high heat generation in the windings.

However, in a fault condition with low heat generation in the windings, the recovery time in the two windings of the braid type coil is more uniform compared with that in the two windings of the non-intersecting type coil due to the structure difference.

- By designing the parameters of both types of coils properly, the AC losses of the braid type coils can be one order of magnitude lower than that of the non-intersecting type coil made with the same length of superconductors. The AC loss characteristics of the non-intersecting type coils are similar to that of the long straight type tape when the distance between adjacent tapes are far enough.

Based on the analysis above, both types of coils have their own advantages and disadvantages in terms of SFCL application. For example, the non-intersecting type coil performs better with regards to recovery time, due to the larger contact area between the superconductor and liquid nitrogen compared with that of braid type coil. However, the insulation problem will become more severe for the non-intersecting type coil when the operation voltage is scaled up gradually.

For the braid type coil, its performance in AC losses is much better than the non-intersecting type coil, especially in low transport current regions. Furthermore, due to its special structure, the external voltage is applied on the two ends of the coil, instead of concentrated at one end as in the non-intersecting type coil. This characteristic increases the ability of the solenoidal coil in withstanding a higher fault voltage, thus making it a good option for SFCLs to be applied at high voltage levels.

Chapter 4 AC losses simulation of two types of non-inductive solenoidal coils

The AC losses of SFCLs is not only relevant to the operation and maintenance costs, but also has a serious impact on the their thermal stability [96]. Experimental comparison of the AC losses of the non-intersecting type coil and that of the braid type coil shows that the two types of coils show different characteristics. The AC losses of the braid type coil are one order of magnitude lower than that of the non-intersecting type coil under low current excitation and the AC losses of the non-intersecting type coil approaches that of a long straight tape. However, the underlying reason that leads to these difference is still unknown. Therefore in this chapter, the electro-magnetic processes of the non-inductive solenoidal coils are simulated with FEM models.

In the past two decades, both analytical and numerical models have been developed to improve people's understanding concerning AC losses of superconducting devices. Analytical models can provide relative direct and simple formulas for devices with simple geometry, such as a long straight tape and stack. However, when it comes to the complicated geometry of SFCLs, it is quite difficult to simulate with an analytical method. Therefore, for simulating superconducting devices with relatively complicated geometries, numerical methods have been developed. These methods have attracted attention from both industry and academia, mainly due to their powerful ability in numerical calculation. To date, various calculation works have been undertaken for the AC losses calculation of straight type and bifilar pancake type SFCLs [56, 97-100]. Furthermore, AC losses of a solenoidal type SFCL built with MgB_2 has also been under investigation by the University of Manchester [101, 102]. However, as far as we know, there is still no systematic simulation work concerning the AC losses of non-inductive solenoidal type SFCLs built with 2G HTS. Therefore, to understand the physical nature of the AC loss characteristics of non-inductive solenoidal coils, 2-D FEM models based on H-formulation and the commonly used E-J power law is proposed in this chapter.

To verify the effectiveness of the proposed models, the simulated AC losses will be compared with that of the experiments. In addition, based on the simulation model, the electro-magnetic characteristics of both types of coils such as current density, magnetic field and the AC losses distribution will be analysed in detail. Furthermore, the impact of different factors on the AC losses of the non-inductive solenoidal coils such as inter-layer separation and the pitch, will also be discussed deeply.

4.1 Introduction of simulation model

Considering the geometry of the solenoidal coil is relatively complicated, a numerical model is used for solving the electro-magnetic phenomenon of the SFCL. Due to the 3-D geometry of the solenoidal coils, theoretically 3-D models should be used for simulating the electro-magnetic characteristics of the non-inductive solenoidal coils. However, the calculation of 3-D models is generally time-consuming and cumbersome. To simplify the calculation, a simplified method based on 2-D axi-symmetric models is proposed here.

4.1.1 Basic assumption of the simulation method

The 2-D axisymmetric model is based on two assumptions. The first assumption is that current flows only in the tangential direction of the cylindrical coordinate shown in Figure 4.1 (a) and the current in the axial direction is neglected. This is justified based on a very small pitch in comparison with the circumference of the solenoidal coil (refer to Table 3.2). The second assumption of the model is that the magnetic field interaction between segments in different azimuthal angles is neglected. This can be explained with the structures of the non-inductive solenoidal coils, which enhance the magnetic field between adjacent superconductors but cancel the magnetic fields that are far from the superconductors. Thus, considering that the radii of the non-inductive solenoidal coils are large enough, it is assumed that the magnetic field of a superconducting segment is only influenced by the superconductor tapes in the same azimuthal angle. Nonetheless, there are two points that need to be considered carefully before the model is used. Firstly, a pitch increase will increase the current in the axial direction, which leads to possible non-negligible currents in the axial direction. Secondly, the reduction of solenoidal radius will also enhance the magnetic field interaction between segments in different azimuthal angles. Therefore, both factors should be considered and analysed carefully before using the model.

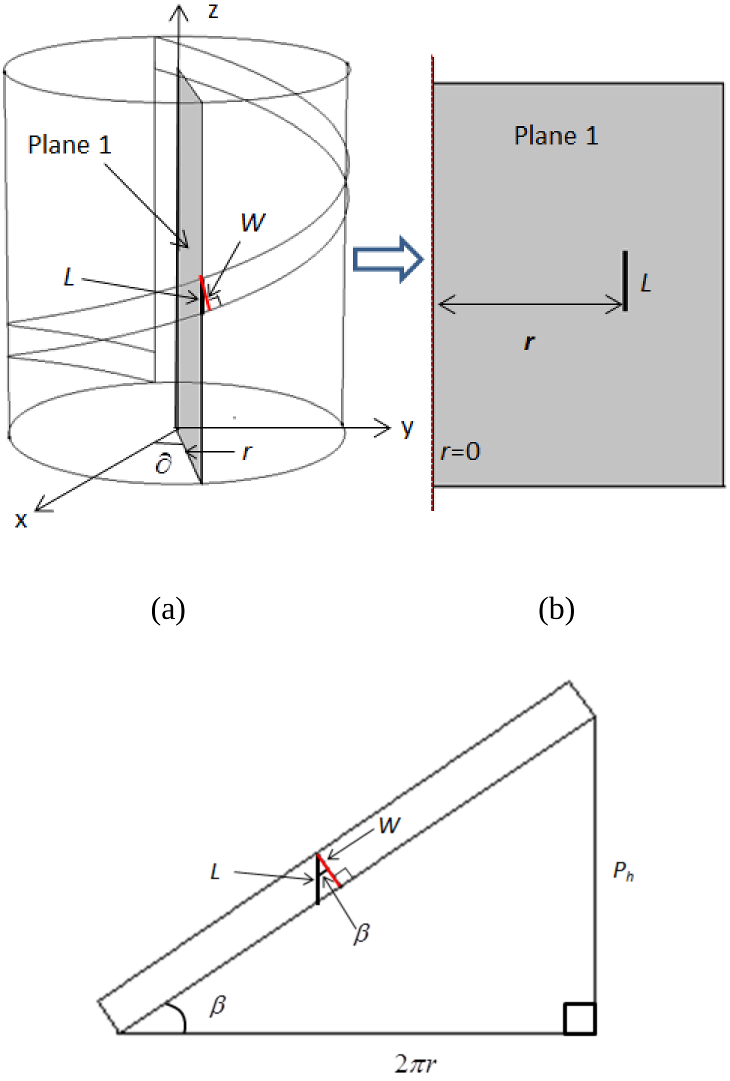

(a) (b)

(c)

Figure 4.1 Overview of the model transformation: (a) cutting of the solenoid coil with Plane 1, which includes the axis of coil; (b) illustration of Plane 1; (c) expanding of the superconducting tape in figure (a) on a plane.

Based on these assumptions, the 2-D axi-symmetric model is extracted from the real geometry. The schematic diagram of the 2-D model extraction is provided here, as shown in Figure 4.1. When the superconducting layer is cut with ‘Plane 1’, the cut section is not exactly the cross-section of the superconducting layer, with the sectional length *L* larger than the width of the superconductor. Therefore, the length *L* needs to be derived. As shown in Figure 4.1 (c), by expanding the superconducting layer onto the same plane, the length *L* can be derived from the width of superconductor (*W*) and the angle β with Equation 4.1 and 4.2.

$$\tan\beta = \frac{P_h}{2\pi r} \tag{4.1}$$

$$\cos\beta = \frac{W}{L} \tag{4.2}$$

where P_h is the pitch of the solenoidal coil, W is the width of the superconductor tape and r is the radius of the solenoidal coil.

4.1.2 Simplification process of both types of non-inductive solenoidal coils

Based on the assumptions introduced in Section 4.1.1, 2-D models are used to simulate the solenoidal coils to save computation time. Due to the symmetry of the non-inductive solenoidal coils, only part of the coil is simulated. For example, for the non-intersecting type coil, only one cross-section of the coil is sufficient for simulating its electro-magnetic characteristics. For the braid type coil, only ¼ part of the coil is sufficient for simulating the electro-magnetic characteristics of the coil. In the following, the symmetry characteristics of the two solenoidal coils, which are used for calculation simplification, and the simplification processes are introduced in detail.

(1) Non-intersecting type coil

For the non-intersecting type coil, it can be cut into two parts with Plane 1, as shown in Figure 4.2(a). If one of them is rotated around the axis of the solenoidal coil for 180°, then the two parts completely overlap. Therefore, for simplification, only 1/2 part of the coil needs to be simulated.

Furthermore, for each part, if Plane 2 that includes the axis is used to cut the winding, then a cross-section with the same relative positions between the tapes will be obtained, as shown in Figure 4.2 (b). Based on the assumption that the magnetic field interaction between segments in different azimuthal angles can be negligible, only one 2-D axisymmetric model is used to simulate the non-intersecting type coil.

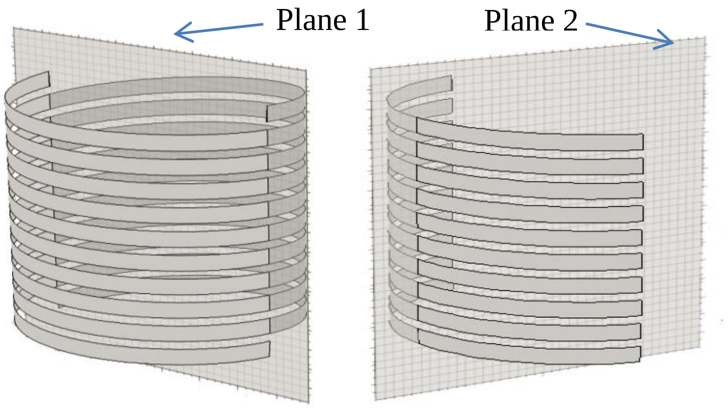

(a) (b)

Figure 4.2 Simplification of the non-intersecting type coil: (a) cutting of non-intersecting coil with plane 1, which includes the axis of coil and the four ending cross-sections; (b) cutting of ½ part of the non-intersecting coil with plane 2, which includes the axis of coil.

(2) Braid type coil

For the simulation of the braid type coil, the whole coil can be divided into four parts, using two perpendicular planes, as shown in Figure 4.3(a) and (b). For the two divided parts in Figure 4.3 (a), by rotating the back part around the axis for 180° and then moving it upwards for pitch/2, the two parts will be absolutely overlapped. Thus for simplification, only ½ part of the coil is needed for simulation. Similarly, after cutting the front part into two segments with the plane 2 in Figure 4.3 (b), the two segments will also be overlapped by rotating one segment around the Line 1 (line 1 is in plane 2 and perpendicular to the axis of solenoidal coil) for 180°. Therefore, based on the two simplifications, only ¼ part of the solenoidal coil is needed for simulation, as shown in Figure 4.3 (c).

Based on Figure 4.3 (c), the ¼ part of the solenoidal coil can be divided into N segments (the impact of divided segment number N to the accuracy of results will be discussed in Section 4.4) by evenly splitting the azimuthal angle θ. Then each segment is approximately simulated with a 2-D axi-symmetric model, which comes from cutting the solenoidal coil with a plane including the axis of the solenoidal coil with azimuthal angle θ equaling $(i-0.5)\pi/2N$ (where i is the i^{th} segment, here $i = 1 \ldots N$).

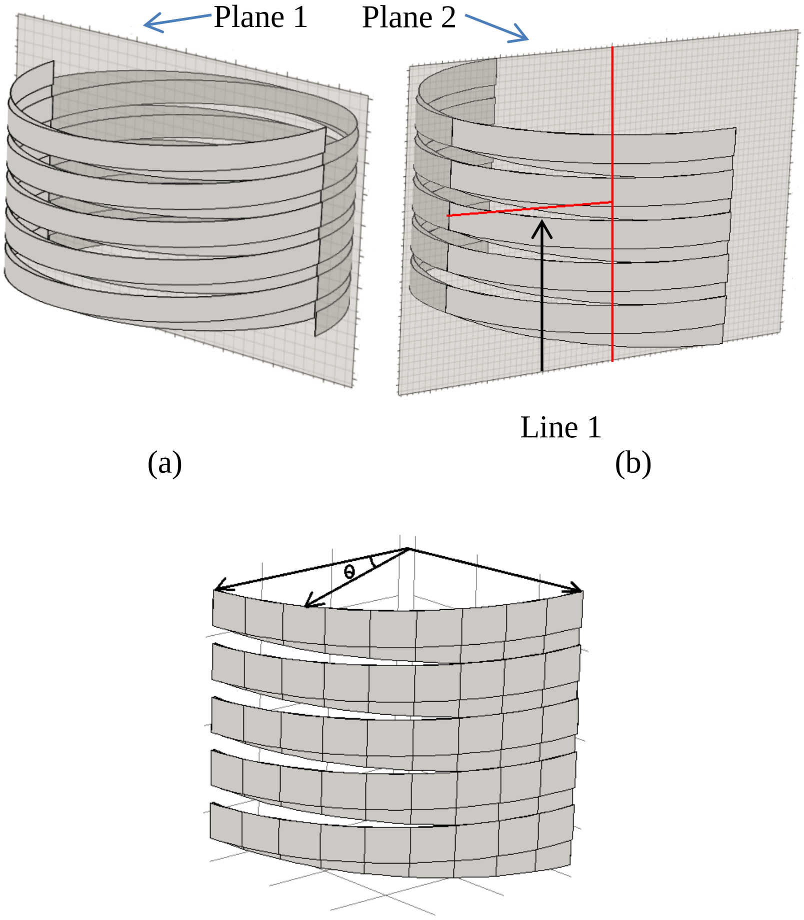

(a) (b)

(c)

Figure 4.3 Simplification of the braid type coil: (a) Cutting of solenoidal coil with plane 1 (plane 1 includes axis of solenoidal coil and is on the same plane with the four ending cross-section),(b) Cutting with solenoidal coil with plane 2 (Plane 2 includes axis of solenoidal coil and is perpendicular with plane 1),(c) Division of ¼ part of solenoidal coil evenly into N segments based on the azimuthal angle θ $(0 \le \theta \le 2\pi)$

4.1.3 Introduction of simulation formulations

In the simulations, the H-formulation [72, 73] and the commonly used *E-J* power law are used as the basic solving equations, which are shown in Equations 4.3 and 4.4.

$$\mu_0\mu_r\frac{\partial H}{\partial t}+\nabla\times(\rho\nabla\times H)=0. \tag{4.3}$$

$$E=E_0\left(\frac{J}{J_{cx}}\right)^n \tag{4.4}$$

n is chosen to be 20, E_0 is defined as 1×10^{-4} V/m, J_{cx} is the critical current density of the superconductor tape, which varies in the width direction.

In all the models proposed, AC losses are calculated with Equation 4.5 as:

$$Q_i=\int_T\int_{A_{sc}}(\boldsymbol{E}\cdot\boldsymbol{J})dsdt \tag{4.5}$$

where T means one cycle, A_{sc} is the cross-sectional area of the superconductors, E and J are the electric field and current density, respectively, and Q_i is the AC losses of the superconductor, with unit J/cycle/m.

For the non-intersecting type coil, the total AC losses per cycle can be calculated with Equation 4.6 as:

$$Q_t=Q_i\cdot2\pi r \tag{4.6}$$

For the braid type coil, the total AC losses per cycle are calculated by Equation 4.7 as:

$$Q_t=4\cdot\sum_{i=1}^{i=N}\left(Q_i\cdot\frac{2\pi r}{4N}\right) \tag{4.7}$$

Where Q_t is the total AC losses and Q_i is the AC losses in segment i (for the non-intersecting type coil, i=1; for braid type coil, i=1…N).

To take into account the impact of the magnetic field on the critical current density, the critical current density of a 10 cm sample under different external magnetic fields was measured. As shown in Figure 4.4(a), the sample was the same as the tape used for building the non-inductive solenoidal coils. Additionally, considering that the magnetic field in the experimental sample is generally a low magnetic field (lower than 50 mT), the self-field effect of the superconductor is also considered by correcting the experimental data with the method proposed by Víctor M. R.

Zermeño [103, 104], as shown in the dashed curve of Figure 4.4 (a). The average error between the experimental measured critical current and the calculated critical current with the corrected $J_c(B)$ is only 0.66%.

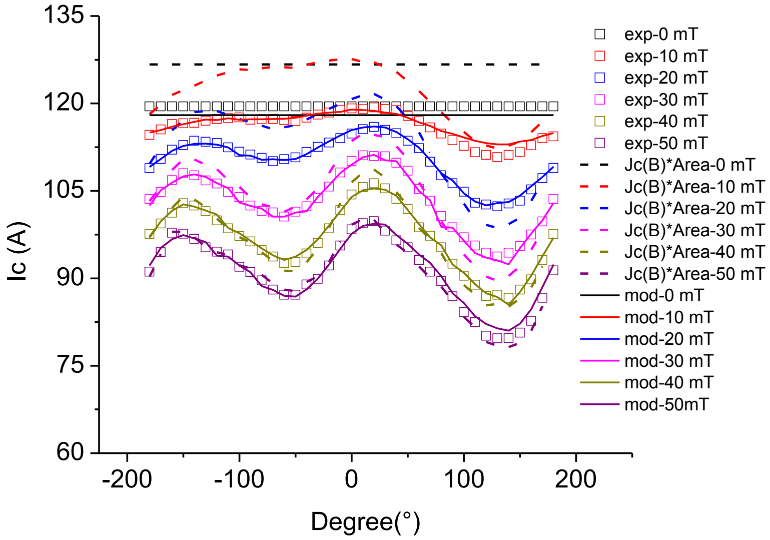

(a)

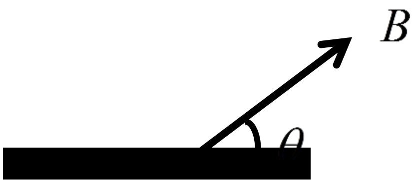

(b)

Figure 4.4 (a) Experimental and simulated critical current of superconductor under external field with different amplitudes and angles, ‘exp’ means the experimental measured value, $J_c(B)$ *Area means the corrected critical current density $J_c(B)$ after taking into consideration the self-field effect, and ‘mod’ means the model calculated critical current with the corrected $J_c(B)$. Here ‘Area’ means the area of superconducting layer cross-section, which is 4e-9 m^2 in this chapter. (b) Schematic diagram of superconductor in external magnetic field.

Besides the magnetic field dependence effect of the critical current density, the degradation of critical current density near the edges of the coated conductors has been known during the fabrication and/or cutting process [105-110]. Therefore, the critical current reduction close to the edges of a superconductor ($J_c(x)$), is also taken into account here, as illustrated in Figure 4.5.

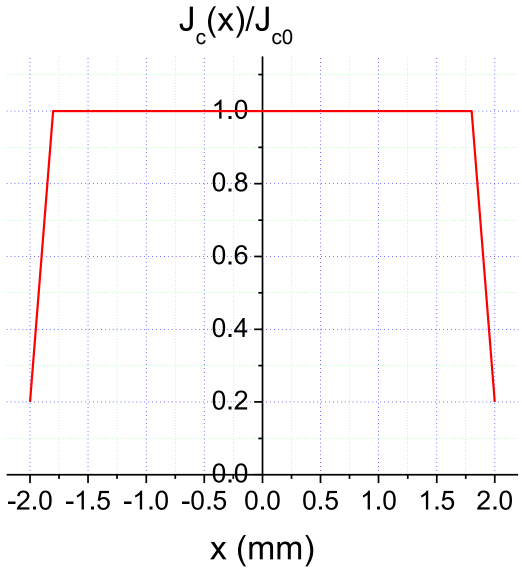

Figure 4.5 Critical current density distribution along the width of the superconductor

J_{c0} is the critical current density in the centre of superconductor, instead of the average critical current density of the superconductor. It can be derived with Equation 4.8 and Figure 4.5 as:

$$\int_{T_{sc}} \int_{W_{sc}} J_c(x)dxdy = I_c \tag{4.8}$$

where $J_c(x)$ means the critical current density and W_{sc} is the width of the superconductor, T_{sc} is the thickness of the superconductor, I_c is the critical current of the superconductor tape.

4.2 Validation of the proposed model

In this section, the AC losses of the non-intersecting type and the braid type coils are simulated with the method proposed. The simulation results are compared with that of experiment, as shown in Figure 4.6. To provide a reference, both the experimental and simulated AC losses of a 40 cm long straight tape are also presented, as also mentioned in Section 3.3.3.

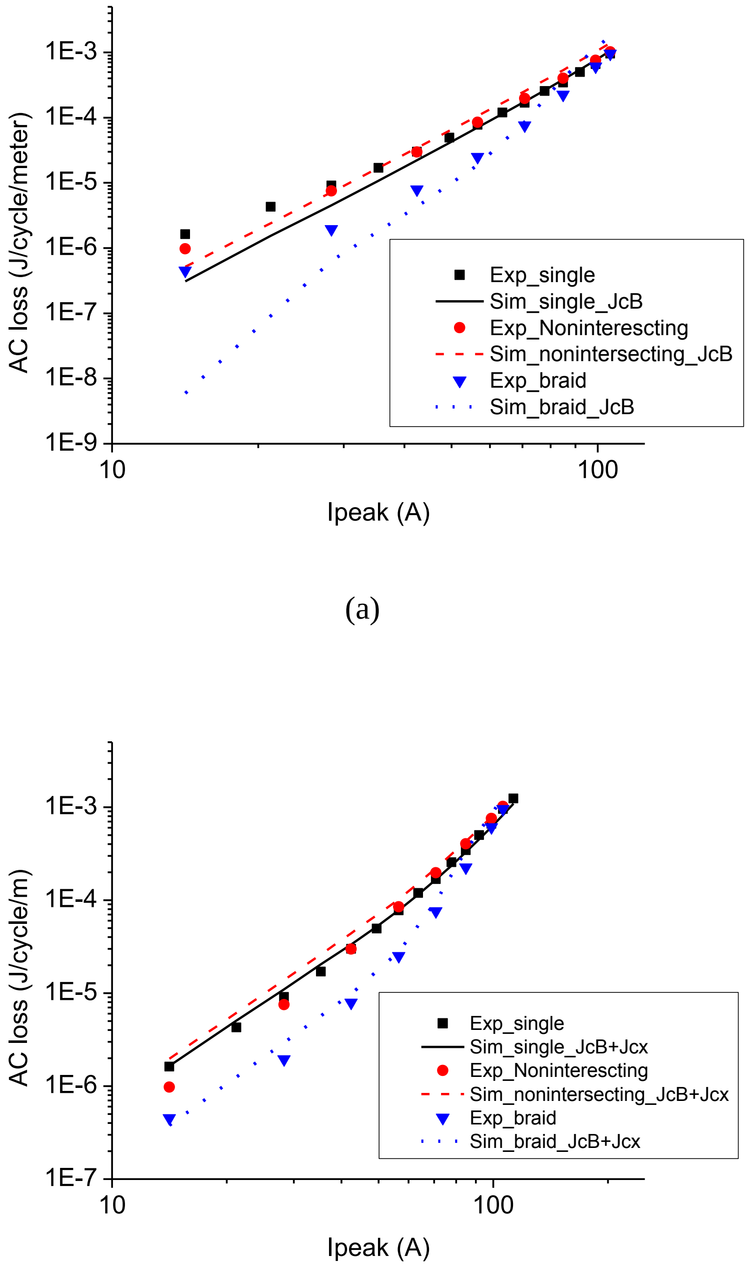

(a)

(b)

Figure 4.6 Comparison of the experimental and simulated AC losses of single straight tape, the non-intersecting type and the braid type coil: (a) only $J_c(B)$ is considered in the simulation, (b) both $J_c(B)$ and $J_c(x)$ are considered in the simulation.

To choose a suitable critical current density in the simulation, two different cases are considered. Firstly, only the impact of magnetic field to critical current density is considered in the simulation, with simulation results shown in Figure 4.6 (a). Figure

4.6 (a) shows that there is a large discrepancy between the experimental results and the calculation results with low applied current, especially for the single tape and the braid type coil when the applied current is smaller than 30 A_{rms}. Secondly, to improve the simulation accuracy, the critical current density reduction at the edge of the superconductor (Figure 4.5) is also taken into account, with the corresponding simulation results shown in Figure 4.6(b). Compared with Figure 4.6(a), Figure 4.6(b) shows a much better agreement between the experimental and simulation results, especially in the low current ranges.

By comparing the experimental and simulation results in Figure 4.6(b), the following observations are made:

- The simulation results of both solenoidal coils are in good agreement with the experimental results, which validates the model in simulating the non-inductive solenoidal coils.
- The AC losses of the braid type coil are smaller than that of the single tape, especially in low current regions (I_{rms} < 70 A). For example, in the case of 14 A, the AC losses ratio of the single tape to the braid type coil reaches seven, which decreases gradually to one with an increasing current.
- The AC losses of the non-intersecting type coil are quite similar to that of the single tape. Only under high currents (I_{rms}>70 A), the AC losses of the non-intersecting type coil is about 20% higher than that of the single tape.

Therefore, the non-intersecting and the braid type coil exhibit different AC loss characteristics: 1) in the low current region, the braid type coil has much lower AC losses compared with the non-intersecting type coil; 2) the slope of AC losses curve of the braid type coil is much higher than that of the non-intersecting coil and single straight tape in the high current region; 3) the AC losses of the non-intersecting type coil is similar with that of the single straight tape. All these phenomena can be attributed to the magnetic field interaction between adjacent tapes in both coils.

In the following section, based on the simulation works done, the AC loss characteristics of both types of non-inductive coils will be analysed in detail to give a more comprehensive explanation.

4.3 Analysis of the AC loss characteristics of the non-intersecting type coil and braid type coils

Based on the model proposed, the AC loss characteristics of the two types of solenoidal coils such as the magnetic field distribution, current density distributions and the AC losses distribution are analysed in detail. However, it is worth noting that only the simulation results (including magnetic field distribution and current density distribution) of the middle turns are presented for both types of coils, which makes it easier to compare the AC loss characteristics of the two types of non-inductive coils.

4.3.1 Non-intersecting type coil

Considering that the AC losses curve of the non-intersecting type coil approximates that of a single tape, as shown in Figure 4.6 (b), the magnetic fields of the nonintersecting type coil and that of a single tape are compared here. Firstly, the magnetic field distribution of the non-intersecting type coil and the single tape in current 75 A_{rms} are provided in Figure 4.7, which shows that for both simulations, a high magnetic field is concentrated near the edges of the superconductor. However, the maximum magnetic field of the tape in the non-intersecting type coil is slightly higher than that of the single tape. This is mainly because of the opposite current directions in adjacent turns, which enhances the magnetic field between the adjacent turns. This also explains why the AC losses of the non-intersecting coil are slightly higher than that of the single tape at high current levels (Figure 4.7).

Besides the magnetic field distribution, the current density distributions of the non-intersecting coil and the single tape in half a cycle when the transport current is 70.7 A are also provided and compared in Figure 4.8. Based on Figure 4.8, the current density distributions of the two prototypes are generally the same, which again provides indication why the AC losses curves of the two prototypes are almost the same. It is worth noting that the decrease of current density in the edges of the superconductor at current peak ($\omega t = 2\pi / 8, 6\pi / 8$) is mainly due to the use of the critical current density distribution J_{cx} (Figure 4.5) in the simulations.

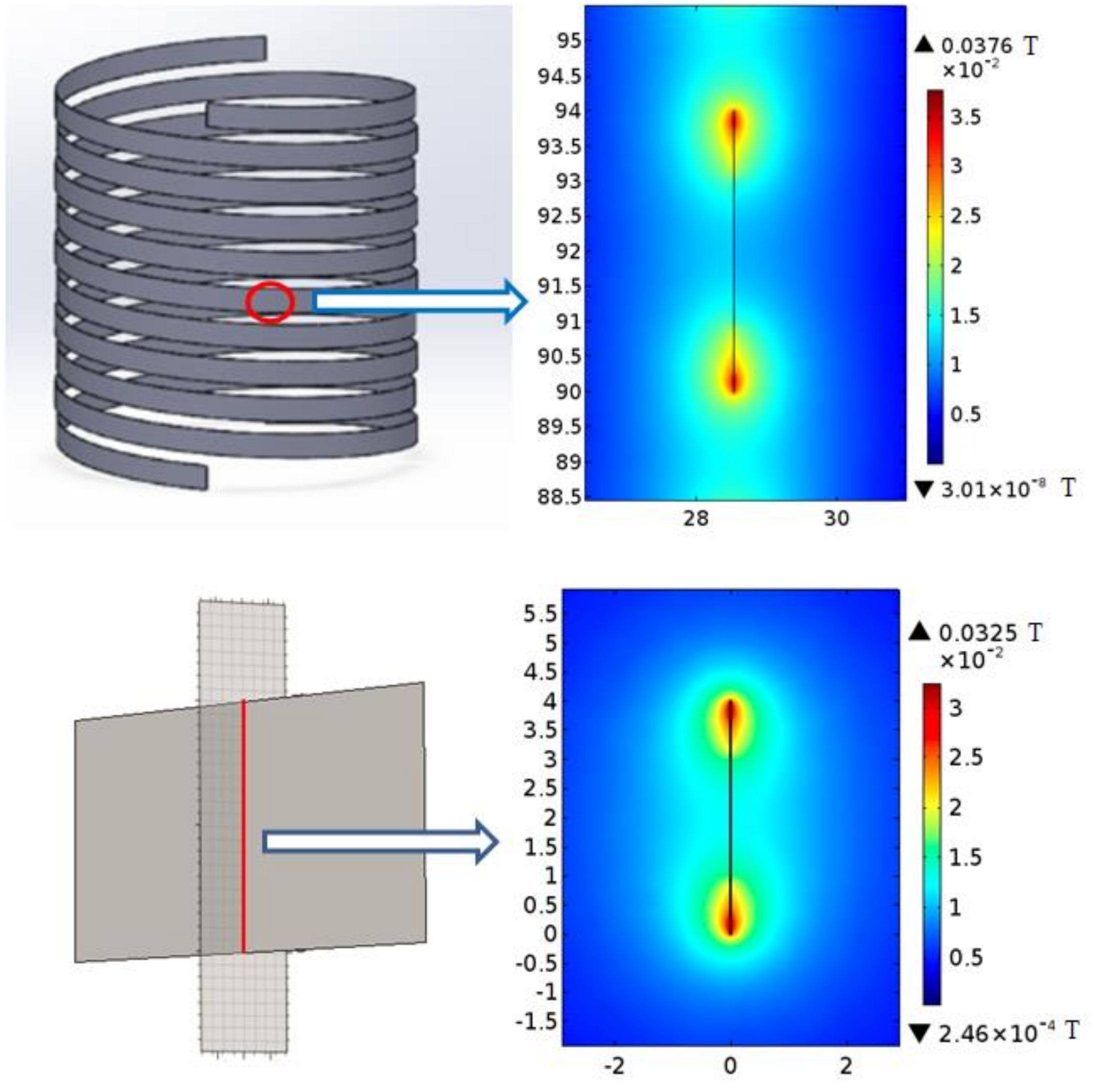

Figure 4.7 Distribution of B_{norm} ($B_{norm} = \sqrt{B_{\perp}^{2} + B_{\parallel}^{2}}$, where $B_{\perp}$ and $B_{\parallel}$ are the magnetic field in the perpendicular direction and parallel direction respectively) in the cross-section of a typical turn in the non-intersecting type coil and that in a long straight tape at 75 A$_{rms}$ (the applied current is $I = \sqrt{2} I_{rms} \sin(2\pi f t)$)

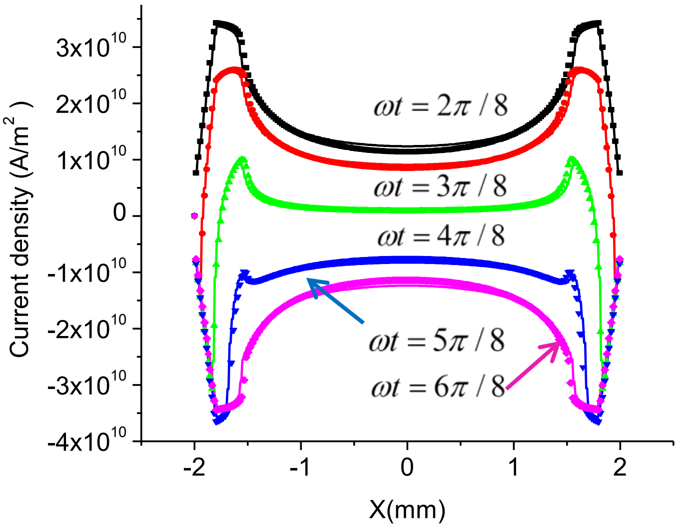

Figure 4.8 Snapshots of the simulated current density distributions along the width of the middle turn of the non-intersecting type coil (scatter symbol) and a single straight tape (solid line) at various times ωt = $2\pi/8$, $3\pi/8$, π, $4\pi/8$, $5\pi/8$, $6\pi/8$) (from top to bottom) during a half cycle when current changes from its positive peak 70.7 A to its negative peak -70.7 A

4.3.2 Braid type coil

Compared to the simulation of the non-intersecting type coil, where only one cross-section model is needed, the simulation of the braid type coil is more complicated. Since the relative position between the inner layer and outer layer varies according to the azimuthal angle, several different 2-D models are needed for the simulation of the braid type coil. Based on the simulation model proposed in Section 4.1.2 (2), the AC losses distributions along θ under different applied currents are plotted in Figure 4.9. Based on Figure 4.9, two phenomena are observed: 1) the AC losses of the superconductor increases with the increase of θ; 2) the AC losses gradually reach a constant with the increase of θ at high current levels, furthermore, the higher the applied current, the larger the AC loss saturation area.

The first observation can be attributed to two reasons. Firstly, for the leftmost segment when θ equals 5°, the tape arrangement is similar to the case of the non-inductive bifilar stack of superconducting strips, where the adjacent turns always carry current in opposite directions. As a result, the magnetic field cancels in the outside space, but increases in the area between the inner layer tape and outer layer tape. Furthermore, the perpendicular magnetic field of the superconductors also cancels due to the symmetric magnetic field distribution (Figure 4.10 (a)), thus leading to significant AC losses reduction, as also analysed in [98, 99]. However, with the increase of θ, the misalignment distance between the two layers of the superconductors increases significantly, resulting in the weakening of perpendicular magnetic field cancellation effects. On the contrary, the misalignment distance increase also leads to the increase of the perpendicular magnetic field enhancement effect, as shown in Figure 4.10 (b). The magnetic field enhancement effect increases the penetration depth from the edges of the superconductor tape, as shown in Figure 4.11, thus leading to higher AC losses of the superconductors in the segments with higher misalignment distances. Especially when the current is high, the AC losses of the segments with $\theta > 45^{\circ}$ are even higher than that of the single tape, as shown in Figure 4.12. However, it is worth noting, for braid type coil, with the change of pitch the AC losses distribution along the coil also changes, which will be analysed in more detail in Section 4.2.2.

Furthermore, Figure 4.12 also provides an indication concerning why the AC losses of the braid type coil is lower than that of a single tape for a range of currents (Figure 4.6 (b)). This is mainly because, in the low current region, the perpendicular magnetic field cancellation effect dominates, which leads to smaller penetration depth and lower AC losses. It is worth noting that, the perpendicular magnetic field cancellation effect is obvious even in segments with high azimuthal angle θ under low current. For example, at a low current of 10 A_{rms}, the maximum magnetic field in the edges of a typical turn in the braid type coil when θ equals 75° is lower than that of a single straight tape, as shown in Figure 4.13.

For the second observation, it is mainly because in higher currents, the perpendicular magnetic enhancement effect reaches its limit, which can be obtained from the penetration depth of the perpendicular magnetic field at segments with different θ, as the example shows in Figure 4.14. When $\theta > 55^{\circ}$, the length of the subcritical region is almost the same, indicating equal total penetration depths (the sum of penetration depth from the two edges of the superconductor) in these positions.

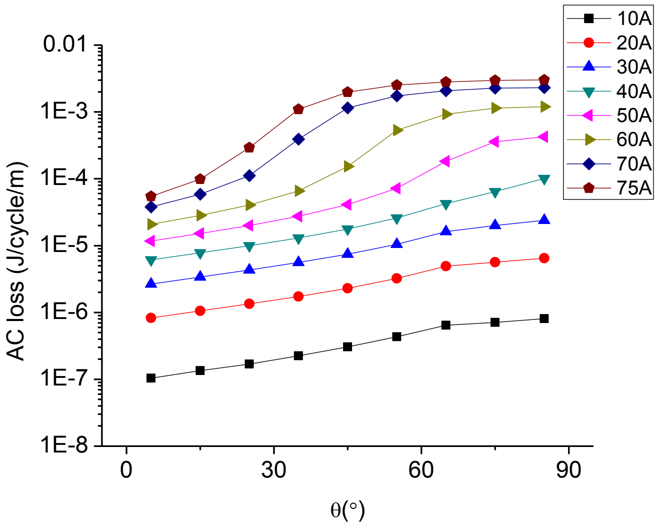

Figure 4.9 AC losses distribution along the different cross sections of the ¼ part of the braid type coil with different applied currents I_{rms} =10…75 A

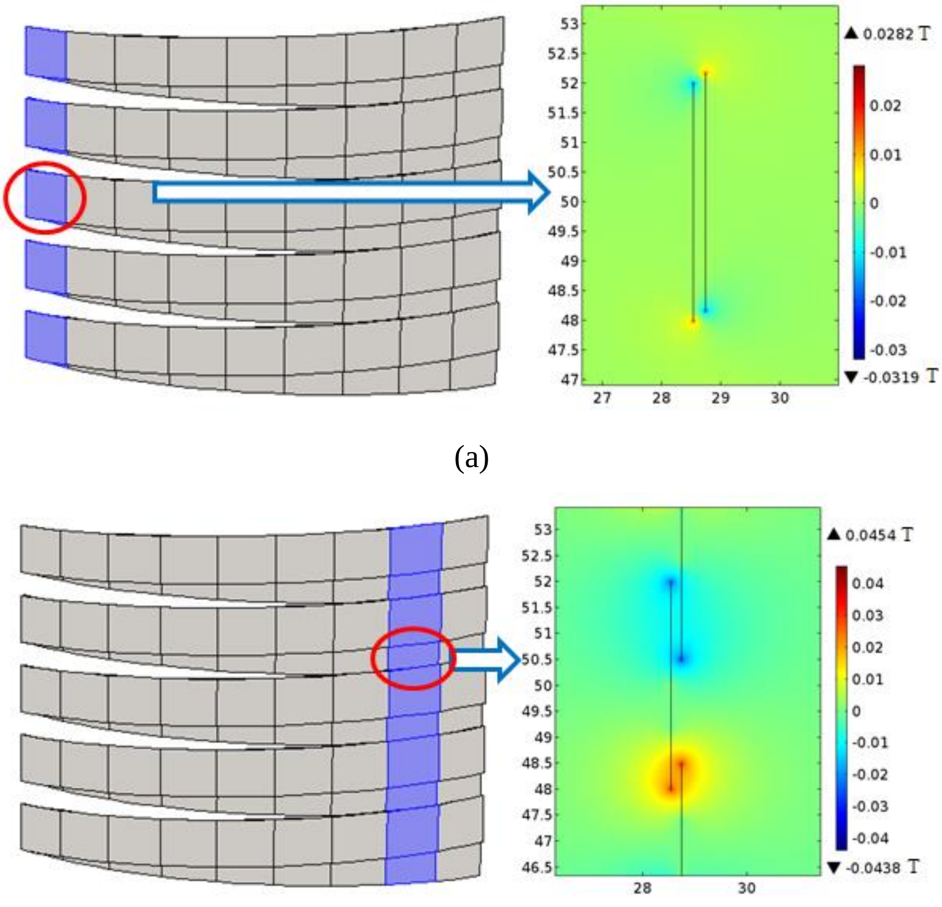

(a)

(b)

Figure 4.10 Distribution of perpendicular magnetic field (B_r) at the current peak when current equals 75A: (a) $\theta = 5^{\circ}$ (b) $\theta = 75^{\circ}$

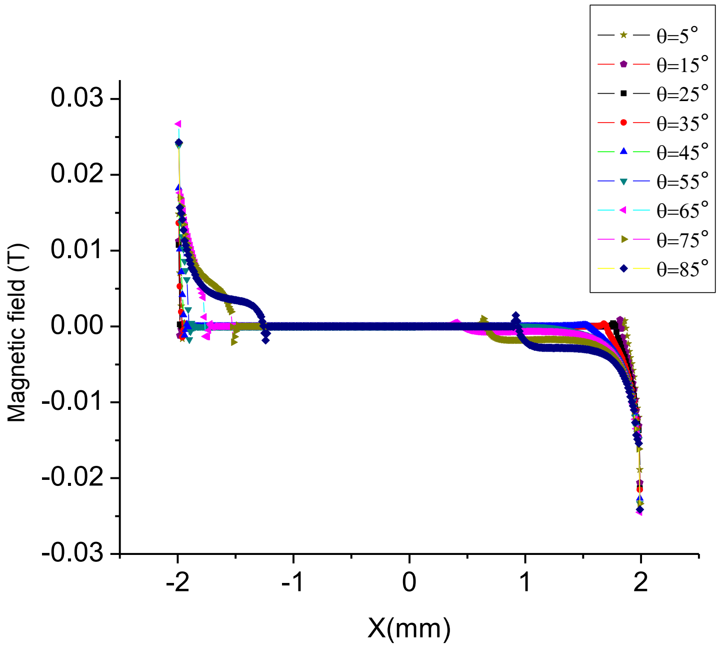

Figure 4.11 Perpendicular magnetic field (B_r) distribution along the width of the superconductor tape at the current peak when the current equals 50 A (Middle turn of the inner layer of the braid type coil is used)

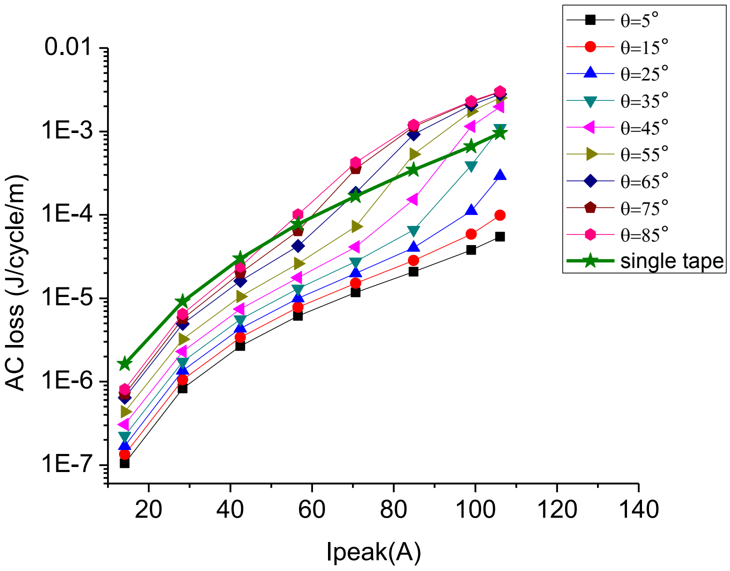

Figure 4.12 Comparison of AC losses at different azimuthal angle of the braid type coil and that of single straight tape

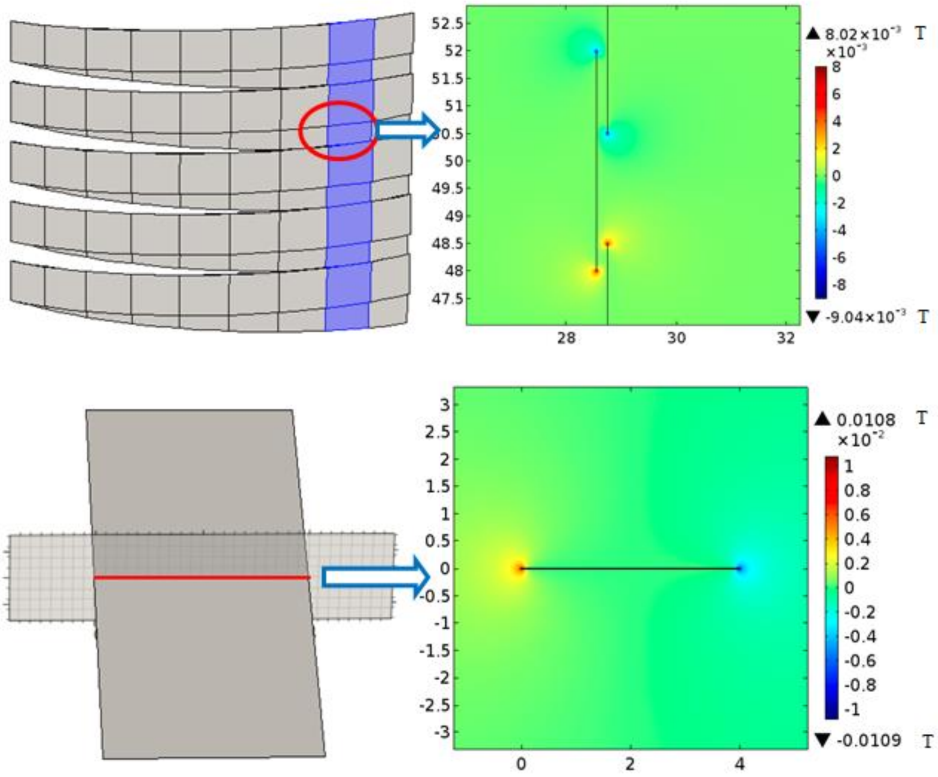

Figure 4.13 Distribution of perpendicular magnetic field ($B_{\perp}$) in the cross-section of a typical turn in (a) the braid type coil and (b) in a long straight tape at the current peak when current is 10 A_{rms}

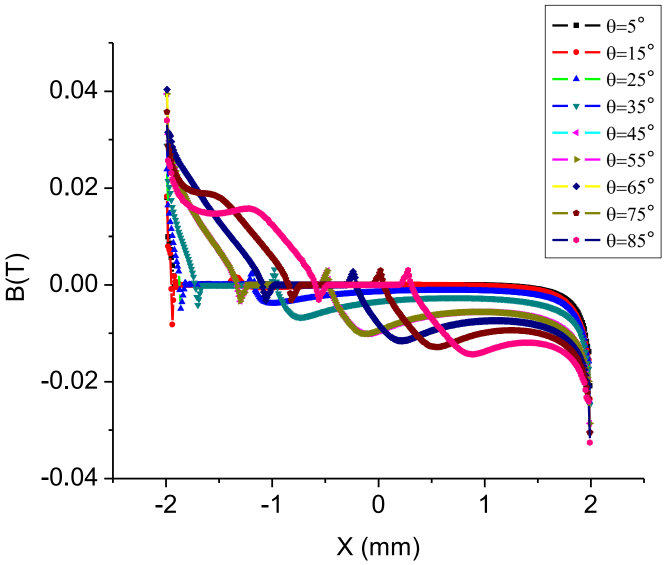

Figure 4.14 The perpendicular magnetic field distribution along the width of the superconductor at current peak when current equals 75A (Middle turn of the inner layer of braid type coil is used)

Another interesting finding related to the braid type coil is the sheet current density distribution, which is shown in Figure 4.15. The sheet current density in the subcritical region is not uniform: the sheet current density at the place with layer overlapping is higher than that of the area without layer overlapping. This is mainly because of the intensive parallel magnetic field between the overlapping area of the adjacent superconductors (Figure 4.16(a), (c)), which penetrates the superconductor from the top and bottom surface of the superconducting strip and generates a high current density near the surface of the overlapping area of the superconductor (Figure 4.16(b) and (d)). The relatively low current density near the left surface of the superconductor in Figure 4.16(b) and that near the right surface of the superconductor in Figure 4.16(d) indicates that the full penetration of parallel magnetic field is still not yet achieved in the overlapping areas. Thus the sheet current density is still lower than the critical sheet current density of the superconductors, as is also indicated in Clem's paper [98].

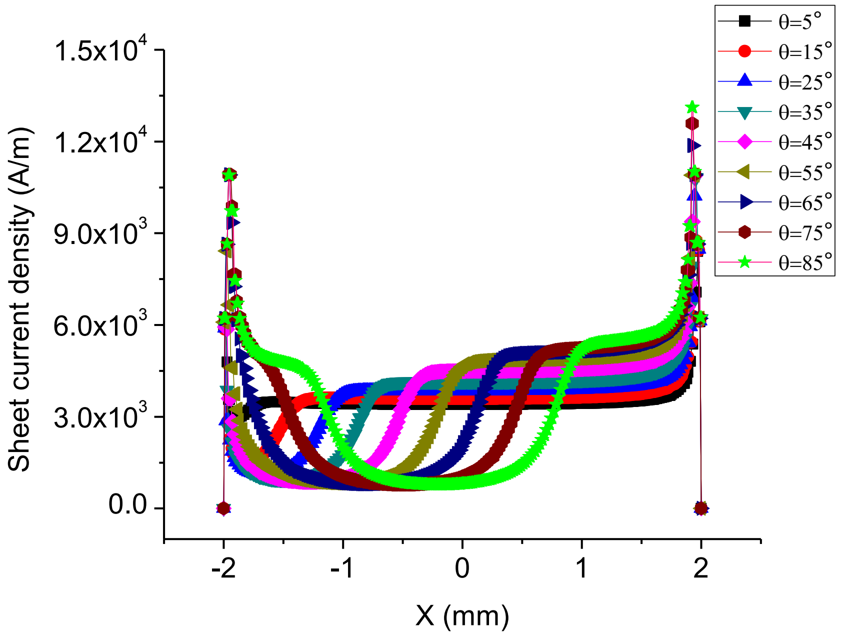

Figure 4.15 Sheet current density distribution of the superconductor at different azimuthal angle of the braid type coil with transport current equaling 10 A_{rms}, (Middle turn of the inner layer of the braid type coil is used)

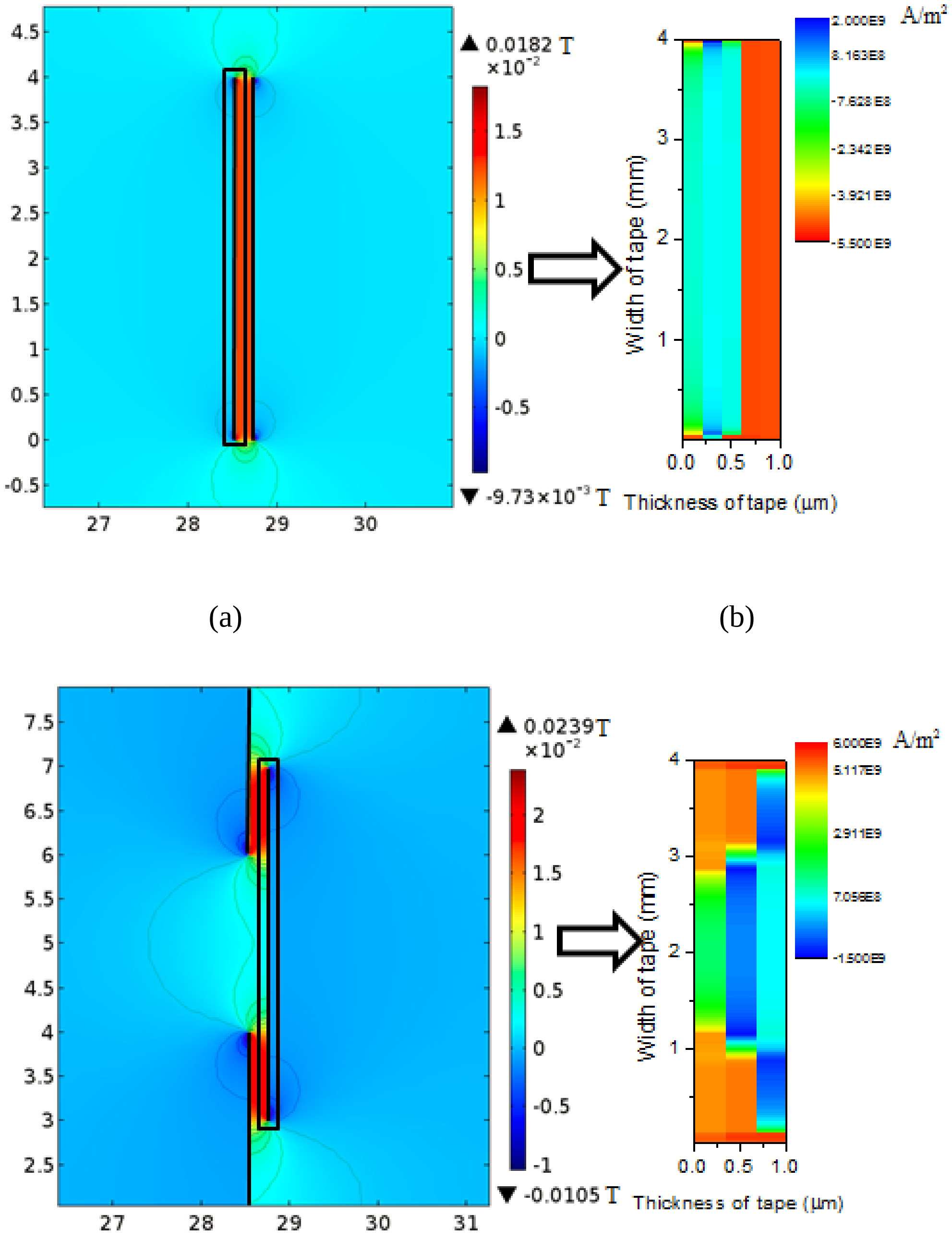

(a) (b)

(c) (d)

Figure 4.16 Contour of parallel magnetic field and current density distribution of the middle turn of braid type coil at the current peak when current equals 30 A: (a) parallel magnetic field distribution when $\theta = 0°$, (b) current density distribution of the superconductor tape indicated in (a), (c) parallel magnetic field distribution when $\theta = 90°$, (d) current density distribution of the superconductor tape indicated in (c).

4.3.3 Analysis concerning the end effects for both types of non-inductive solenoidal coils

For both types of non-inductive solenoidal coils, due to the different magnetic field distribution at the ends of coils, the AC losses at the ends are different from that in the coil middle. In this section, the end effects of both types of solenoidal coils are analysed based on the simulation of the two prototypes.

(1) Braid type coil

To evaluate the end effects of the braid type coil, the AC losses in different turns are compared based on the AC losses calculation of the prototype built. To make it easy to understand, the relative deviation of the AC losses is plotted in Figure 4.17, which is calculated with Equation 4.9.

$$d_i = \frac{\left|P_i - \overline{P}\right|}{\overline{P}} \times 100\% \tag{4.9}$$

where d_i is the relative deviation, P_i is the AC losses at the i^{th} turn of the braid type coil and $\overline{P}$ is the AC losses of the tape in the braid type coil with infinite turns. Here the AC losses of the middle turn (8th turn) is approximated as that of the infinite turn coil, which is validated because the relative deviations of the 7th and 9th turns are lower than 0.3% for all calculated cases with different azimuthal angles.

Figure 4.17 shows the relative deviation d_i of the AC losses in different turns at different azimuthal angles of the braid type coil when the applied current is 75 A_{rms} for both the inner and outer layers. From Figure 4.17, the following are observed:

- The closer the turn is to the end of the coil, the more severe are the end effects. For example, when $\theta = 55^\circ$ the d_i of the first, second and third turns from the bottom are 47.5%, 13% and 6% respectively, which indicates a reduction in the end effects. This can be easily understood based on the comparison between the tape arrangement at the end of the simulated braid type coil and that in the infinite turn coils.
- The end effects in the top and bottom end of the coil are not same. For example, when $\theta = 55^\circ$, the relative deviation of the topmost turn is 30.8%,

and that of the bottommost turn is 47.5%. This is mainly because of the structure of the braid type coil, where there is no symmetry and periodicity for most longitudinal sections. Therefore, the magnetic field interaction between the inner layer and outer layer at the two ends are also different, leading to different AC losses.

- The relative deviation distribution varies according to the azimuthal angle. As shown in Figure 4.17 (a) and (b), the relative deviation of AC losses is always the highest when $\theta = 55^{\circ}$ and $\theta = 65^{\circ}$, and it gradually decreases to both sides. This can be attributed to the dependence of the end effects on the magnetic field interaction between different turns. For segments with small θ, such as when $\theta = 5^{\circ}$, the magnetic interaction between different turns is negligible since the magnetic field is generally constraint between the inner and outer tapes in the same turns, as shown in Figure 4.10 (a). Therefore, the perpendicular magnetic field distribution in the end turns and that in the middle turns are almost the same, leading to similar AC losses with low relative deviation (maximum d_i is 3.5% for $\theta = 5^{\circ}$). However, with the increase of θ, the perpendicular magnetic enhancement effect increases the magnetic field interaction between different turns, as shown in Figure 4.10 (b). This leads to the decrease of the similarity of the magnetic field distribution between the end turns and the middle turns. Therefore, for segments with higher θ, the end effect is more severe and the relative deviation is much higher (maximum d_i is 47.5% for $\theta = 55^{\circ}$).

In summary, the AC losses distribution is severely impacted by the end effect, which is mainly concentrated on the several turns in the end of the coil. The end effect mainly results from the magnetic field interaction between the inner and outer layer windings: when the magnetic field cancellation effect dominates, the end effect is weak, however, when the magnetic field enhancement effect dominates, the end effect is stronger. Additionally, the asymmetric characteristic of braid type coil leads to the different end effects in the top and bottom of the coil.

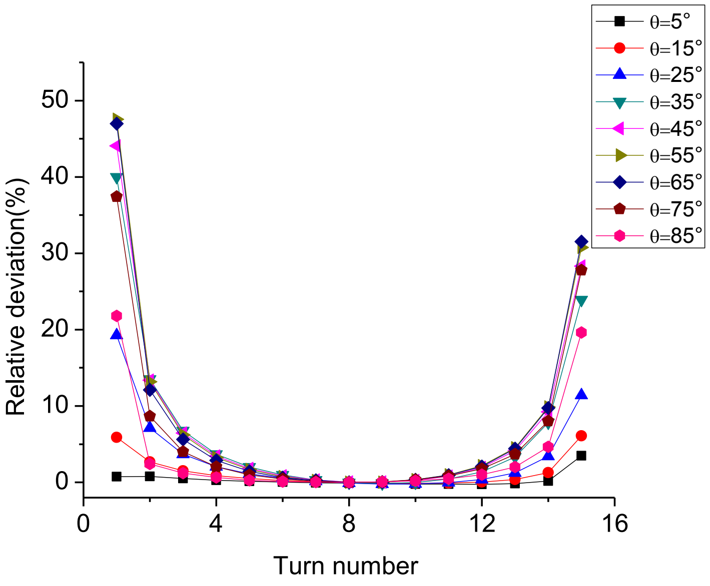

(a) Inner layer of the braid type coil

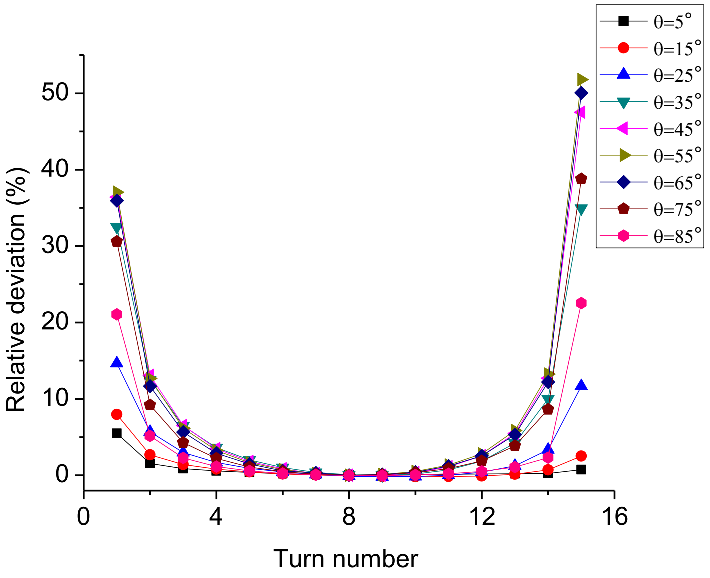

(b) Outer layer of the braid type coil

Figure 4.17 Relative deviation of AC losses distribution at different azimuthal angles when the applied current equals 75 A_{rms}: (a) Inner layer of the braid type coil, (b) Outer layer of the braid type coil. (Turn number is counted from the bottom to top of the braid type coil)

(2) Non-intersecting type coil

For the non-intersecting type coil also, the end effects are analysed using the same method. Different from the braid type coil, where the end effects are quite significant especially for segments with high θ, the end effects of the non-intersecting type coil are relatively weak and is mainly limited to the outermost two turns, as shown in Figure 4.18. For example, the relative deviation of the outermost two turns is between 5%-12%, whilst the relative deviation decreases to 3% in the third turns. The weak end effects might be caused by the relatively far distance between the adjacent turns, which leads to weak magnetic field interactions, as shown in Figure 4.7.

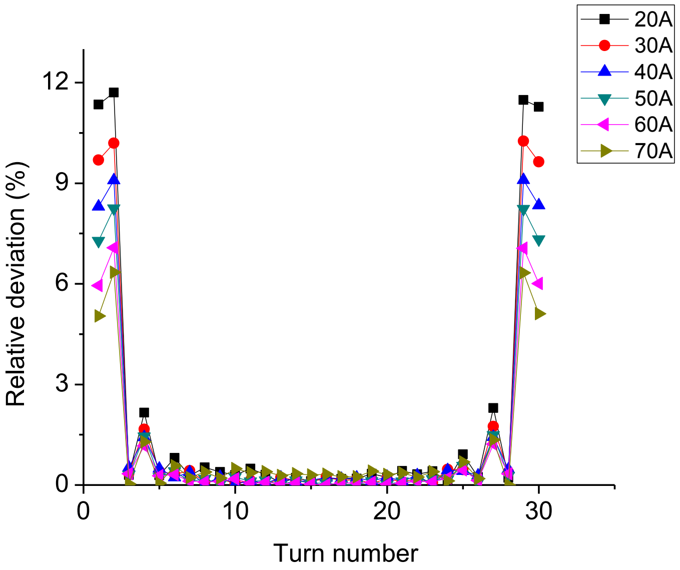

Figure 4.18 Relative deviation of the AC losses distribution of the non-intersecting coil when the applied current $I_{rms} = 20...70A$ (Turn number is counted from the bottom to the top of the non-intersecting type coil)

4.4 Study of the impact of different factors on the AC losses of non-inductive solenoidal coils

For both types of non-inductive solenoidal coils, different factors such as the pitch and radius of coils will influence their AC losses. To determine the impact of these factors, solenoidal coils with different parameters are simulated and the impact trends are extracted from the simulation results.

Here, to save calculation time, simplified models are used for the AC losses calculation of the braid type and the non-intersecting type coils. For the braid type coil, a 14-turn-coil (7 turns for inner layer and 7 turns for outer layer) is used for the

AC losses simulation, where the AC losses of the middle turns are used for comparison. For the simulation of the non-intersecting type coil, a simplified model simulating only one turn by using the periodical condition is used.

4.4.1 Impact of coil division to the AC losses calculation of the braid type coil

To study the impact of coil division number on the simulation results, a fourteen-turn braid type coil is simulated with *N* models, as shown in Figure 4.3(c), where *N* is the division number. The simulated AC losses with different *N* are shown and compared in Figure 4.19. For clear comparison, the relative tolerance of each simulated AC losses is calculated with Equation 4.10.

$$R_d = \frac{Q_N - Q_0}{Q_0} \times 100\% \tag{4.10}$$

Where Q_N is the AC losses of the braid type coil with division number equalling *N* (Figure 4.3(c)), Q_0 is the real AC losses of the braid type coil, which is approximated as the AC losses value with largest division number (15 for an applied current of 10 A and 21 for an applied current of 75 A). Figure 4.19 indicates that the relative tolerance decreases sharply with an increase of division number N from one to three and then gradually reaches zero. Therefore, to get simulation results with relative deviation less than 2.5%, $N \geq 5$ is recommended.

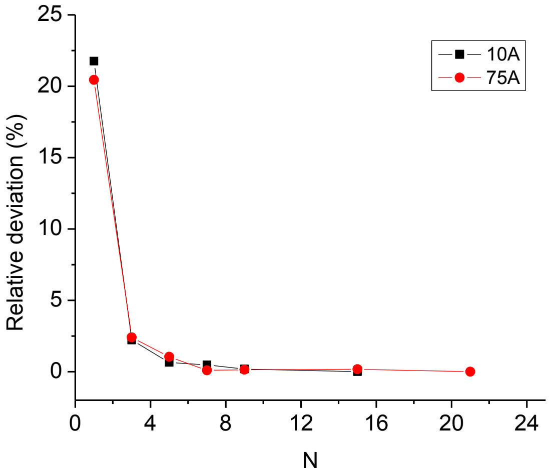

Figure 4.19 Impact of division number *N* of the ¼ solenoidal coil on the relative deviation of the AC losses of the braid type coil

4.4.2 Impact of pitch on the AC losses of the two types of solenoidal coils

To study the impact of the pitch on the AC losses of the non-inductive solenoidal coils, coils with different pitches are simulated for both types of coils.

For braid type coil, different pitches (5, 6, 8, 12, 16 mm) are used and the simulation results are shown in Figure 4.20. Figure 4.20 shows that with the increase of pitch the AC losses of the braid type solenoidal coil increases rapidly first and then decreases gradually. This result can be explained with the detailed AC losses distribution in braid type coil, as shown in Figure 4.21. With different pitches, the AC losses distributions of the braid type coils are quite different. For a pitch smaller than 8 mm, the AC losses increases continuously with the increase of θ. When the pitch increase above 8 mm, the AC losses increase sharply first and then decreases gradually to a stabilised value.

These observations can be explained with the magnetic field interaction between the inner and the outer windings. For braid type coil, the misalignment distance in each segment with longitudinal section with azimuthal angle θ is $\frac{\theta}{\pi/2} \times \frac{Pitch}{2}$. Therefore, the misalignment distance increases with the increase of pitch for each azimuthal angle θ. When the pitch is smaller than 8 mm, the increase of misalignment distance will lead to the weakening of the magnetic field cancellation effect for low θ and increase the magnetic field enhancement effect for high θ, both of which will increase the corresponding AC losses generated. However, when the pitch is higher than 8 mm, there is no overlapped area between the inner and the outer layers when the misalignment distance increases above 4 mm, which leads to a weaker magnetic enhancement effect and thus lower AC losses. This is clearly shown by the AC losses curves of 12 mm and 16 mm in Figure 4.21, where the AC losses decrease after reaching a peak value. Due to the increase of pitch and the corresponding misalignment increase rate, the AC losses decrease faster and approach that of the single tape finally. In summary, the AC losses are higher at positions where the magnetic enhancement effect is strong and are lower at positions where the magnetic field cancellation effect dominates. When both effects are weak, the AC losses tends to approach that of a single long straight tape.

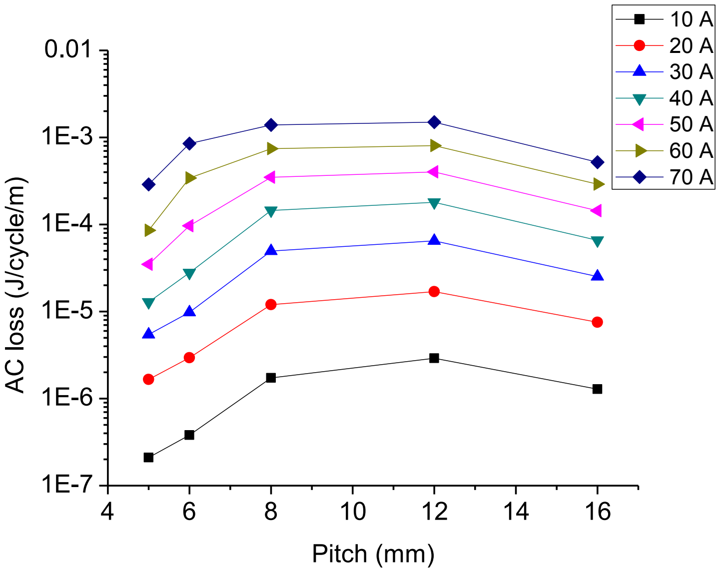

Figure 4.20 The impact of pitch on the AC losses of the braid type coil at different applied currents for layer distance of 0.2 mm

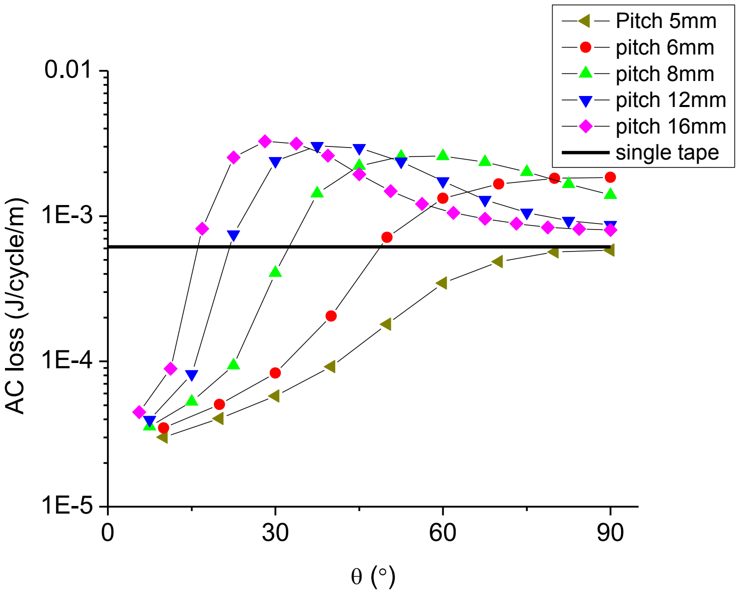

Figure 4.21 Comparison of AC losses distributions of solenoidal coils with different pitches and that of single straight tape when I_{rms} equals 70 A

For the non-intersecting type coil, different pitches (8.2, 10, 12, 16, 20, 24 mm) are also used for testing its impact on the AC losses, as shown in Figure 4.22. With the increase of pitch, the AC losses decreases fast firstly and then gradually decreases to a stabilised value for different applied currents, as shown in Figure 4.22. This phenomenon is easy to understand based on the analysis in Section 4.3.1. A smaller pitch indicates closer distance between tapes in a non-intersecting type coil, which leads to a stronger magnetic field enhancement effect at the edge of the superconductor, thus leading to higher AC losses. With the increase of pitch, the magnetic field enhancement effect weakens gradually, thus leading to lower AC losses.

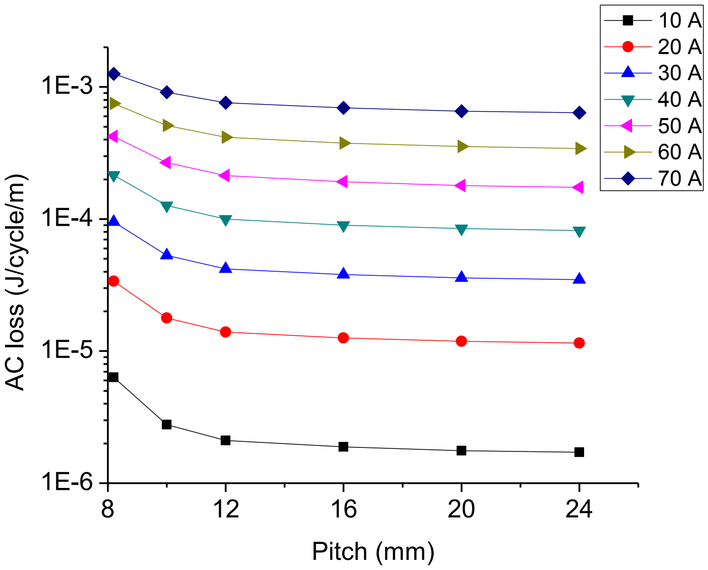

Figure 4.22 Impact of pitch on the AC losses of the non-intersecting type coil when I_{rms} equals 10…70 A

4.4.3 Impact of the inter-layer separation on the AC losses of the braid type coils

To analyse the impact of the inter-layer separation on the AC losses of the braid type coils, coils with different inter-layer separations (0.2 mm, 1 mm and 5 mm) are simulated with the proposed model. As is shown in Figure 4.23, with the increase of the inter-layer separation, the AC losses increase when the applied current is lower than 50 A_{rms} but decrease when the applied current is higher than that. This phenomenon can be explained based on the analysis in Section 4.3.2, Figure 4.24 and Figure 4.25. At low current values such as 20 A (Figure 4.24), with the increase of the inter-layer separation, the AC losses of the segment with small azimuth angle increases gradually, leading to higher total AC losses and more even AC losses distribution. This is mainly because the magnetic field cancellation effect, which dominates the AC losses in areas with small azimuth angles, is undermined. Since the AC losses in areas with higher azimuth angles do not change much, it is inferred that the magnetic field enhancement effect is weak for low current values.

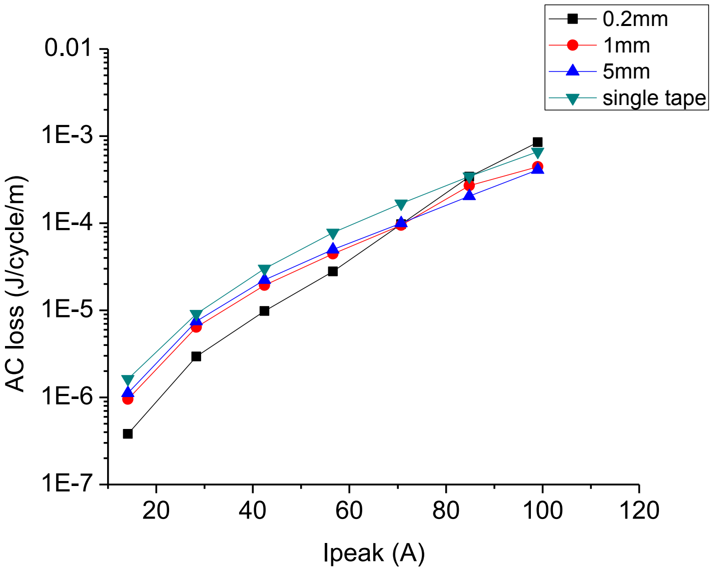

Figure 4.23 Impact of the inter-layer separation to AC losses of the braid type coil at different applied currents (I_{rms} =10…70 A)

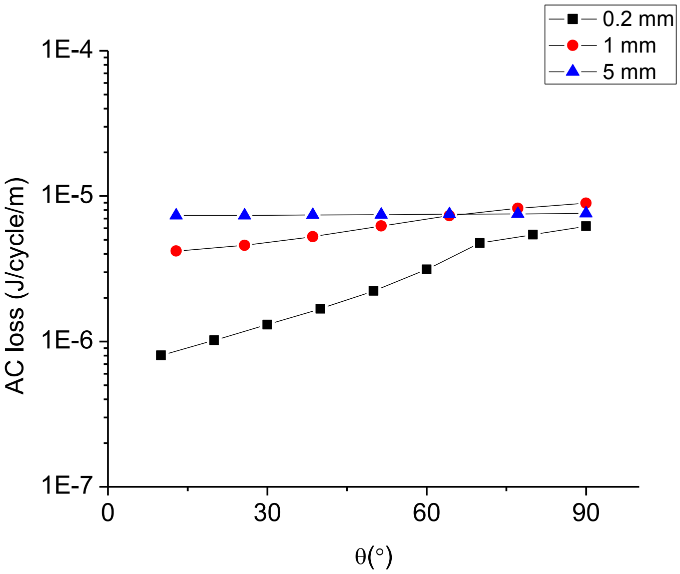

Figure 4.24 AC losses distributions of the braid type coils with different inter-layer separations when the current equals 20 A_{rms}

However, when the applied current is high, the case is quite different. As is shown in Figure 4.25, for an applied current of 70 A_{rms}, the increase of inter-layer separation will lead to the decrease of the AC losses of the segment with azimuth angle higher than 45°, but results in the increase of the AC losses of the segment with azimuth angle lower than 45°. This means, for the case of high applied current, besides the undermining of the magnetic cancellation effect in the low azimuth angle area, the magnetic enhancement effect also begins to play a significant role in the high azimuth angle area. Since the increase of the inter-layer separation will lead to the weakening of the magnetic enhancement effect, lower AC losses are expected in segments with high azimuth angle (Figure 4.10(b)). Generally speaking, since the AC losses in high azimuth angle areas are more significant than that in low azimuth angle areas, the total AC losses will decrease with the increase of the inter-layer separation under high applied current.

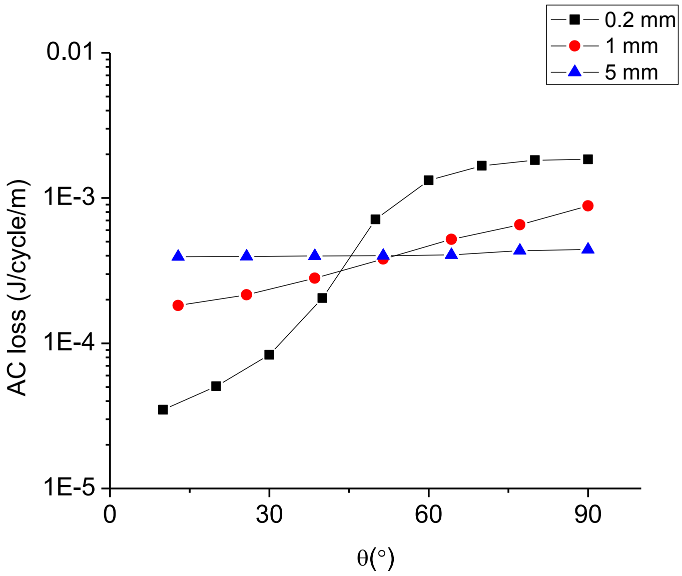

Figure 4.25 AC losses distributions of the braid type coils with different inter-layer separations when the current equals 70 A_{rms}

4.5 Conclusions

In this chapter, a simplified method based on 2-D axi-symmetric models was proposed for simulating the AC loss characteristics of both the non-intersecting type and the braid type coils. Comparison between the experimental and simulation results verified the simulation model proposed for the solenoidal coils.

It was found in experiment that the AC losses of the braid type coil was lower than that of a single tape by about an order of magnitude in low current regions and the

AC losses characteristic of the non-intersecting type coil was quite similar with that of a single tape. Based on the model proposed, the AC loss characteristics, the magnetic field and current density distributions of both types of coils are analysed in detail. Simulation shows that the AC losses of the braid type coil was greatly impacted by the relative position between the inner and outer layer tapes, which determines the magnetic field interaction between the adjacent tapes in the two layers. Additionally, the magnetic field distribution and the current density distribution of the non-intersecting type coil are approximately same as that of the long straight tape.

Furthermore, simulation work concerning the impact of different parameters on the AC losses of both types of non-inductive solenoidal coils showed that, by adjusting the pitch or inter-layer separations, the AC losses of the coils could be effectively decreased. These findings provided indications of how to optimise the design of SFCLs from the point of view of AC losses reduction.

- For the non-intersecting type coil, it was observed that too small of a pitch will increase the AC losses by a significant amount due to the magnetic field enhancement effect (for example, the AC losses double when the pitch decreases from 10 mm to 8.2 mm when current is smaller than 20 A_{rms}). Hence, it is recommended to have a pitch of at least 12 mm, with a distance between adjacent tapes to be of at least 2 mm.
- For the braid type coil, generally speaking, the AC losses were lower for smaller pitches (the smallest pitch of the braid type coil was 4 mm, which corresponded to the limiting case of the width of the tape used). Therefore, it was suggested that the pitch should be smaller than 6 mm from the point of view of decreasing the AC losses.
- Concerning the impact of the inter-layer separation on the AC losses of the braid type coil, it was observed that the AC loss characteristics depended mainly on the magnitude of the current applied. Hence, it was recommended to determine the inter-layer separation based on the specific characteristics of the coil during its normal operational current.

These findings indicated that while applying SFCLs at high-voltage levels, the braid type coil will be a more competitive choice from the point of view of AC loss characteristics. Nonetheless, for the design of SFCLs, there are still some other factors that need to be considered, such as inductance during normal operation, recovery time, equipment size, etc. For example, the increase in pitch of the non-intersecting type coil will lead to the increase of SFCL capacity and the inductance of a solenoidal coil, whilst the decrease of the pitch of the braid type coil will result in the increase of the recovery time. Considering these factors, more comprehensive study is needed for optimising the overall performance of non-inductive solenoidal coils.

In the next chapter, a 220 V/300 A large-scale braid type SFCL will be designed, built and tested to provide a preliminary study concerning the application of the braid type SFCL in high voltage levels. Additionally, in the design process, the optimisation of different parameters of the braid type SFCL will also be discussed in detail.

Chapter 5 Design, fabrication and test of a 220 V/300 A braid type superconducting fault current limiter prototype

In this chapter, to validate the application of braid type coil in practical SFCLs, a 220 V/300 A braid type superconducting fault current limiter prototype is designed, fabricated and tested. Due to the capacity of the testing laboratory, the voltage level of the SFCL prototype is limited to 220 V. This chapter provides a preliminary study concerning the issues to be considered in the SFCL fabrication process as well as the possible solutions for these issues in the development of braid type SFCLs.

The network requirements concerning the 220 V SFCL are firstly described in detail. Following this, the coated conductor used for the SFCL is selected based on the minimum thermal length and minimum limitation length. The basic characteristics of the coated conductors, such as the resistivity versus temperature property, the current limiting property, recovery characteristic and AC loss characteristics, are studied with experimental testing. Subsequently, the impacts of different parameters such as substrate orientation, coil diameter and coil pitch on the working performance of the SFCL are discussed in detail. Finally, based on all these discussions, a lab-scaled braid type SFCL is designed, fabricated and tested.

5.1 Requirements concerning the SFCL prototype

The network requirements concerning the 220 V SFCL prototype are shown in Table 5.1. The SFCL to be designed is a single phase SFCL, which is operated at a

220 V voltage level, with a rated current of 300 A during normal operation. The maximum prospective fault current is chosen based on [12], where the maximum prospective fault current and limited fault current for a 220 kV/300 MVA saturated iron core SFCL are 50 kA and 30 kA respectively. Considering the rated current for the 220 V SFCL prototype is 300 A, the maximum prospective fault current and the limited fault current are 18.75 kA and 11.25 kA respectively. In the case of faults, the SFCL is expected to react in five milliseconds and limit the fault current for a period of 0.1 seconds. After the fault, the SFCL prototype is expected to recover in five seconds.

Table 5.1 Requirements concerning the SFCL prototype

Frequency [Hz]	50
Rated voltage in normal condition [V]	220
Rated current in normal condition [A]	300
Prospective maximum fault current [kA]	18.75
Maximum limited fault current [kA]	11.25
Fault duration [s]	0.1
Maximum recovery time of the SFCL [s]	5

5.2 Selection of 2G HTS tape

For the first step, the tape used for the SFCL should be properly selected. In this work, two kinds of HTS tapes are considered: tape from SuperPower and tape from AMSC. The two kinds of tapes have different manufacturing processes, compositions and structures.

The SuperPower 2G HTS tapes are fabricated by an automated, continuous process using thin film deposition techniques, such as those used in the semiconductor industry, to apply the superconducting material on buffered metal substrates [29]. While a metal organic deposition process is issued for producing the AMSC tapes [111]. Furthermore, the two types of tapes also have different structures and compositions, as shown in Figure 5.1. Figure 5.1 shows that the substrate of the AMSC tape is made of magnetic material Ni-5at%W, whilst that of the SuperPower tape is composed of non-magnetic material Hastelloy C-276. In addition, the stabiliser of the AMSC tape is made of stainless steel (SUS) 316L, whilst that of the SuperPower tape is made of copper. Compared with SUS 316L, copper has a much lower resistivity and heat capacity.

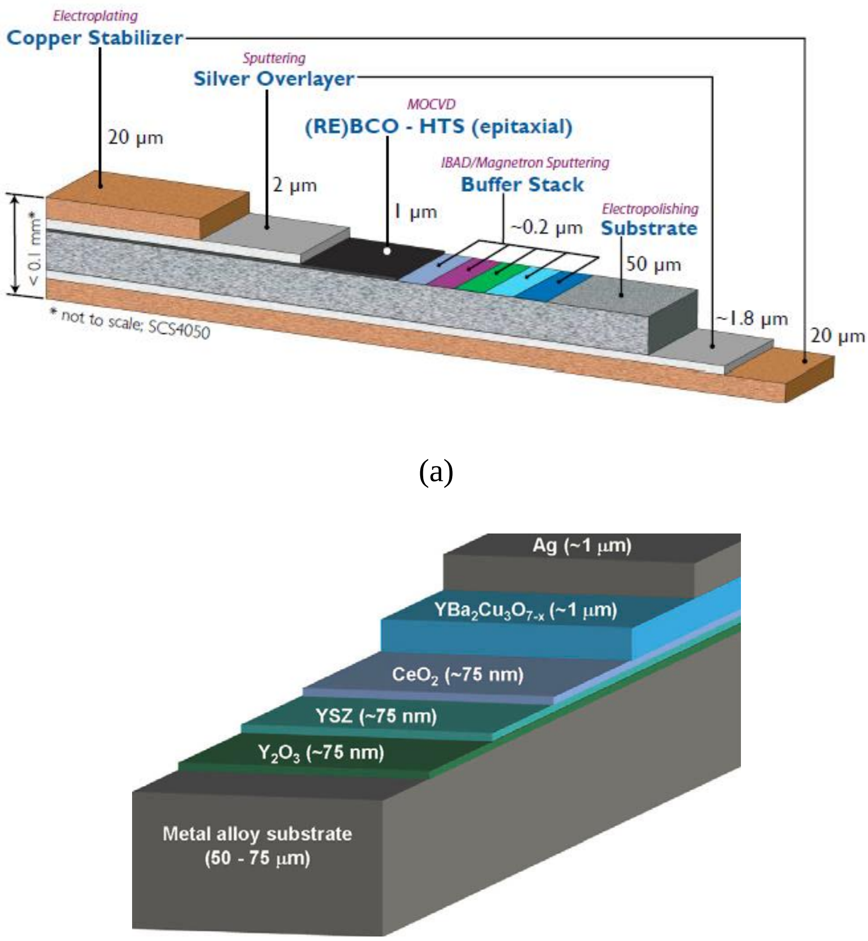

(a)

(b)

Figure 5.1 Comparison between (a) SuperPower tape [29] and (b) AMSC tape [112]. Note: for the AMSC tape used for fault current limiting, stainless steel is generally used as the stabiliser, which is not indicated in (b).

The price of the superconducting element of a SFCL is mainly determined by the superconductor tape length and width. For superconductor width, only 12 mm tape was considered in this work for easy comparison. For superconductor length, the determination of the minimum superconductor length of the 220 V/300 A SFCL is discussed in detail here.

Generally speaking, the superconductor length of a SFCL is determined by two factors: the limitation length ($L_{cond}^{\lim}$) and the thermal length (L_{cond}^{th}) [19]. The maximum of the two lengths will be considered as the minimum length of a superconductor.

Firstly, the limitation length is derived from the current limitation of a SFCL during fault period. In the case of a fault, a superconductor will lose its superconductivity and function as a high resistor, limiting the fault current to a lower value, which is named as the limited fault current ($I_{\lim}$) [19]. Theoretically, the limited fault current should be within the interrupting capability of circuit breaker in the circuit so that the fault can be cleared successfully. This value will be determined before the design of a SFCL, as shown in Table 5.1. With the limited fault current known, the limitation length of a superconductor can be calculated with Equation 5.1. Equation 5.1 indicates that the limitation length of a superconductor is proportional to the cross-section of the superconductor tape and inversely proportional to its resistivity. Therefore, to decrease the length of a superconductor as well as to decrease its cost, a superconductor with higher resistivity and lower cross section is preferred.

$$L_{cond}^{\lim} = \frac{V_{cond}}{R_l^{cond} I_{\lim}} = \frac{V_{cond}}{I_{\lim}} \frac{A_{cond}}{\rho_{cond}} \tag{5.1}$$

where $L_{cond}^{\lim}$ is the limitation length of the superconductor, V_{cond} is the voltage across the superconductor tape, R_l^{cond} is the conductor resistance per unit length, A_{cond} is the cross section of the superconductor tape and ρ_{cond} is the average resistivity of the superconductor tape.

Another factor, the thermal length L_{cond}^{th}, is based on the maximum endurable temperature and the heat balance theory. During the fault period, the maximum temperature of a superconductor should not exceed the maximum endurable temperature, thus no degradation will be generated. As mentioned in [19], a superconductor can be regarded as adiabatic during the fault duration when the thermal exchange between superconducting and the cooling fluid is neglected, thus all the heat generated in the superconductor is used for increasing the temperature of the superconductor. The heat balance is therefore expressed with Equation 5.2 as:

$$\int_0^{\Delta t} v_{cond}(t) i_{cond}(t) dt = \int_{T_0}^{T_{\max}} c_p(T) A_{cond} L_{cond}^{th} dT \tag{5.2}$$

where Δt is the fault period, $v_{cond}(t)$ is the instantaneous voltage across the superconductor tape, $i_{cond}(t)$ is the instantaneous current through the superconductor tape, $T_{\max}$ and T_0 are the maximum and operation temperatures respectively, $c_p(T)$ is the superconductor specific heat per unit volume, and L_{cond}^{th} is the thermal length of the superconductor.

By assuming a homogeneous behaviour along all the superconductors, the thermal balance equation can be expressed with Equation 5.3, as:

$$\frac{v_{cond}(t)^2}{\rho_{cond}(T)\frac{L_{cond}^{th}}{A_{cond}}} = c_p(T)A_{cond}L_{cond}^{th}\frac{dT}{dt} \tag{5.3}$$

Where $\rho_{cond}(T)$ is the average resistivity of the different non-superconducting layers that are connected in parallel. Thus the thermal length L_{cond}^{th} can be derived with Equation 5.4, as:

$$L_{cond}^{th} = \sqrt{\frac{\int_0^{\Delta t} v_{cond}(t)^2 dt}{\int_{T_c}^{T_{\max}} \rho_{cond}(T)c_p(T)dT}} \approx V_{cond}\sqrt{\frac{\Delta t}{\int_{T_0}^{T_{\max}} \rho_{cond}(T)c_p(T)dT}} \tag{5.4}$$

Where V_{cond} is the RMS voltage applied to the superconductor tape.

Based on Equation 5.4, a higher $\rho_{cond}(T)$ and higher c_p^m is preferable for achieving minimum superconductor length $L_{\min}$.

In summary, based on Equations 5.1 and 5.4, for choosing a suitable superconductor tape in the SFCL design, a superconductor with a higher resistivity, smaller cross-section and higher heat capacity is preferred. However, considering the thermal length is in general higher than the limitation length [19], only the resistivity and heat capacity of a superconductor are regarded as the main factors that determine the minimum length of required superconductor.

Concerning resistivity, both the AMSC and SuperPower tape are determined by the stabiliser. Consequently, the resistivity of SUS 316L is much higher than that of copper. Therefore, for stabilizer with the same geometry, the AMSC tape is preferable with aspect of resistivity. Furthermore, the heat capacity of a superconductor is generally determined by the stabiliser and the substrate. It is not difficult to find that the heat capacity of SUS 316L (stabiliser of the AMSC tape) and Ni-5at%W(substrate of the AMSC tape) are much higher than that of copper (stabiliser of the SuperPower tape) and the Hastelloy C-276 (substrate of the Superpower tape) respectively. Therefore, with regards to the heat capacity, the AMSC tape is also preferable. Finally, the 8602 type Amperium wire from AMSC is chosen for building the SFCL prototype, the detailed parameters of the tape are introduced in Section 5.3.

5.3 Characterisation of the AMSC superconductor tape used for the SFCL prototypes

As mentioned above, the 8602 type Amperium wire from AMSC was chosen for building the 220 V/300 A SFCL prototype. This type of tape consists of one HTS/substrate insert structure, which is placed between two layers of 75 μm thick 316L stainless steel laminate. The minimum critical current of the tape is 241 A (77 K) in self field. The geometric parameters of the tape are provided in Table 5.2.

Table 5.2 Geometric parameters of the 8602 type AMSC tape

Layer	Width/mm	Thickness/μm
Stainless steel (top layer)	12	75
Silver	10	2
YBCO	10	1
Substrate	10	75
Stainless steel (bottom layer)	12	75
Solder (left side)	1	78
Solder (right side)	1	78

To properly design the SFCL prototype, it is necessary to test and understand the properties of the AMSC superconductor tape, such as resistivity versus temperature, current limiting properties, recovery and AC loss characteristics. Therefore, in this section, all these properties are characterised based on experiments.

5.3.1 Temperature dependence of resistivity of the 8602 type AMSC tape

During a fault period, the critical current of superconductors is exceeded by the fault current, which leads to heat generation and temperature increase in the superconductor. When the temperature of a superconductor increases above the critical temperature, the superconductor loses superconductivity and its resistivity increases approximately linear with temperature. Considering that the temperature of a superconductor during fault should not exceed 300 K to avoid superconductor degradation [19], it is necessary to measure the trend of superconductor resistivity with temperature, thus the temperature of the superconductor can be estimated.

To measure the resistivity of a superconductor at different temperatures, different temperature (from 77 K to 300 K) conditions need to be realised experimentally. Ideally, this can be achieved with a cryocooler. However, it usually takes hours for the temperature in a cryocooler to stabilise, which makes the experiments very time-consuming.

To speed-up the experimental process, a simple and fast method was used to roughly estimate the resistivity versus the temperature curve. This method is mainly based on the temperature recovery process of a superconductor after being taken out of liquid nitrogen (77 K) or hot water (373 K) and kept at room temperature. The schematic diagram is shown in Figure 5.2. In the experiment, a 10 cm segment of superconductor tape is firstly immersed in liquid nitrogen (or hot water). Then after the superconductor temperature stabilises, the segment is taken out of the liquid nitrogen (or hot water) and kept at room temperature. During the subsequent temperature recovery period, both the temperature and resistance of the superconductor are recorded simultaneously. The temperature of the superconductor is measured with PT 100. To measure the superconductor resistance, a small DC current (0.5 A) is provided to the segment and the superconductor voltage is measured continuously during the experiment. Both the temperature sensor signal and the superconductor voltage signal are recorded with a NI data acquisition card SCXI-1125.

The experimentally measured results are shown in Figure 5.3, which shows that the resistance of the superconductor increases approximately linearly with temperature.

Furthermore, the resistivity is 0.053 Ω/m at 92 K (critical temperature) and 0.123 Ω/m at 300 K (room temperature), which means the resistance approximately doubled when the temperature increases from 92 K to 300 K.

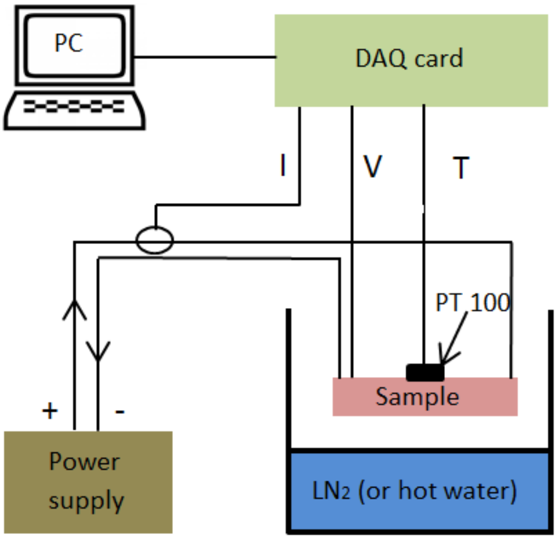

Figure 5.2 Schematic diagram of the resistance measurement system

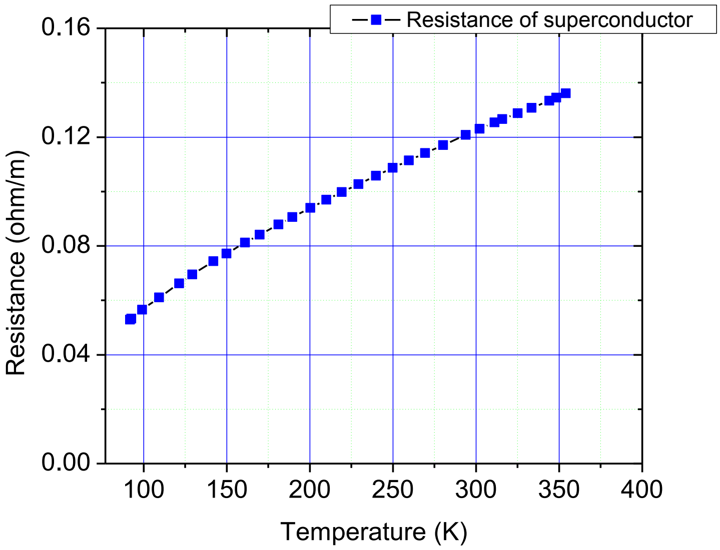

Figure 5.3 Trend of the superconductor tape resistance with temperature

5.3.2 The current limiting property of the 8602 type AMSC tape

The current limiting property of the 8602 type AMSC tape is tested with a 10 cm tape sample by using the fault current test system shown in Figure 3.3. The aim of the test was to find the maximum averaged voltage that the superconductor can withstand during a fault period, which corresponds to the case where the superconductor temperature reaches approximately 300 K at the end of a fault.

The results of the fault current tests are summarised in Table 5.3, which show that with the increase of rated voltage, both the heat generation and the temperature of the superconductor increase gradually. Furthermore, with the increase of rated voltage, the limited current increases gradually.

Table 5.3 Summary of the fault current test results

Rated voltage (output of transformer)/V	Limited current/A	Heat generation in total/J	Maximum resistance reached /ohm/m	Maximum temperature/K
6	398	60.7	0.081	161.15
7	441	81.9	0.088	181.70
8	479	110	0.098	213.03
15	550	133	0.104	233.05
17	578	141	0.107	243.39
20	620	182	0.117	280.19
22	643	210	0.122	297.40

Based on the experimental results presented in Table 5.3, the relationship between the heat generated in a superconductor and the maximum temperature of the superconductor can be extracted, as illustrated in Figure 5.4. From Figure 5.4, the heat generated that causes the superconductor temperature to rise up to 300 K can be derived.

The test results with the rated voltage equaling 22 V are provided in Figure 5.5, Figure 5.6 and Figure 5.7. Figure 5.5 shows that during fault period, the superconductor voltage increases and its current decreases gradually. Both trends can be attributed to the resistance increase of the superconductor, which is caused by the heat generated and the resulting temperature increase in the superconductor. The superconductor resistance rise increases the voltage shared by the superconductor and decreases the current in the circuit. Furthermore, the resistance change of the superconductor during the fault period is also shown in Figure 5.6. In Figure 5.6, the sudden resistance increase in the first cycle is due to the state transition of the superconductor from the superconducting state to a normal sate; the subsequent steady resistance increase is mainly because of the steady increase of temperature. The power dissipation in Figure 5.7 shows that the heat dissipation in the first half cycle is higher than the rest of the cycles.

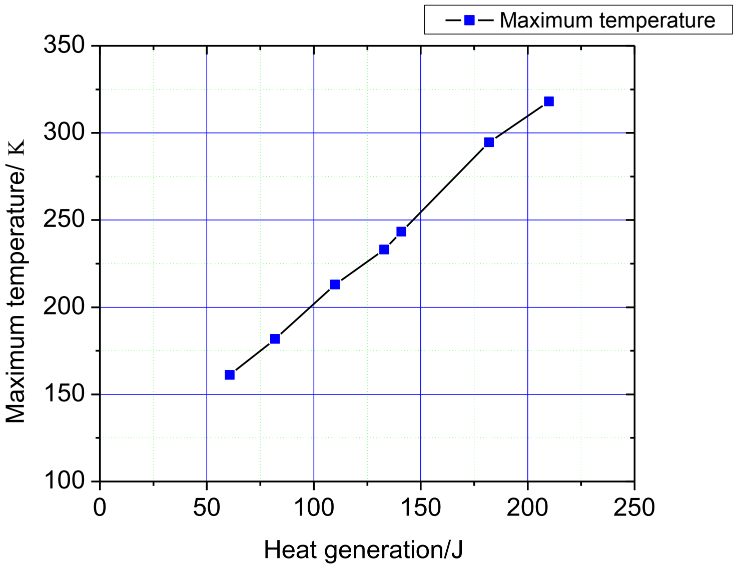

Figure 5.4 Relationship between the heat generated in the superconductor sample and the maximum temperature in the superconductor

To get the rough maximum voltage that the superconductor can withstand during a fault period, the RMS value of the superconductor voltage under a transformer output voltage of 22 V is calculated, which is 4.5 V. Considering the sample length is 10 cm, the electric field that the superconductor tape can withstand should be 45 V/m. This value can be used for a rough calculation of the superconductor length needed for SFCL design [113, 114].

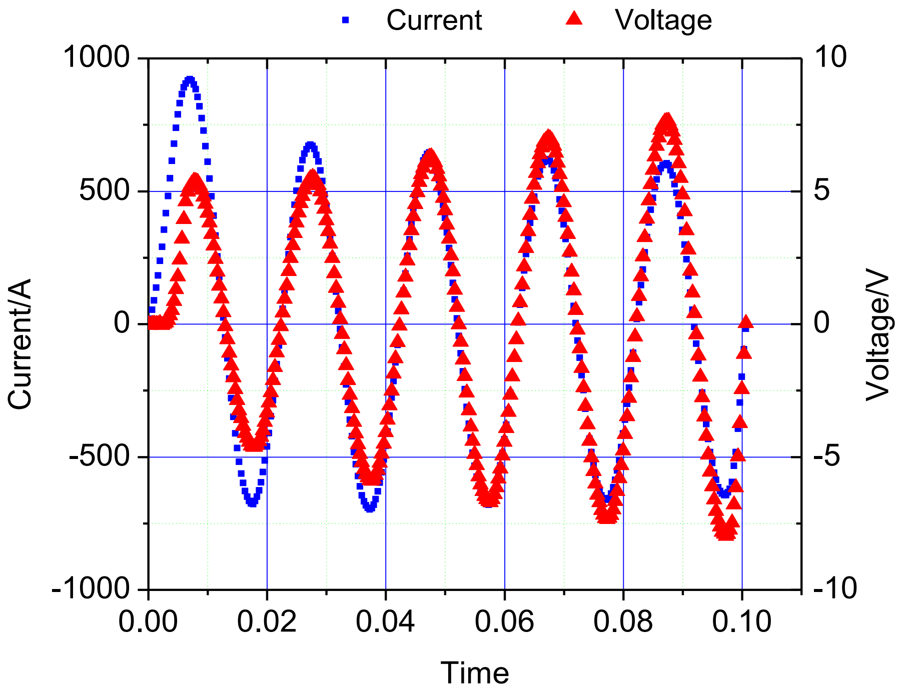

Figure 5.5 Experimental measured voltage and current during the fault period

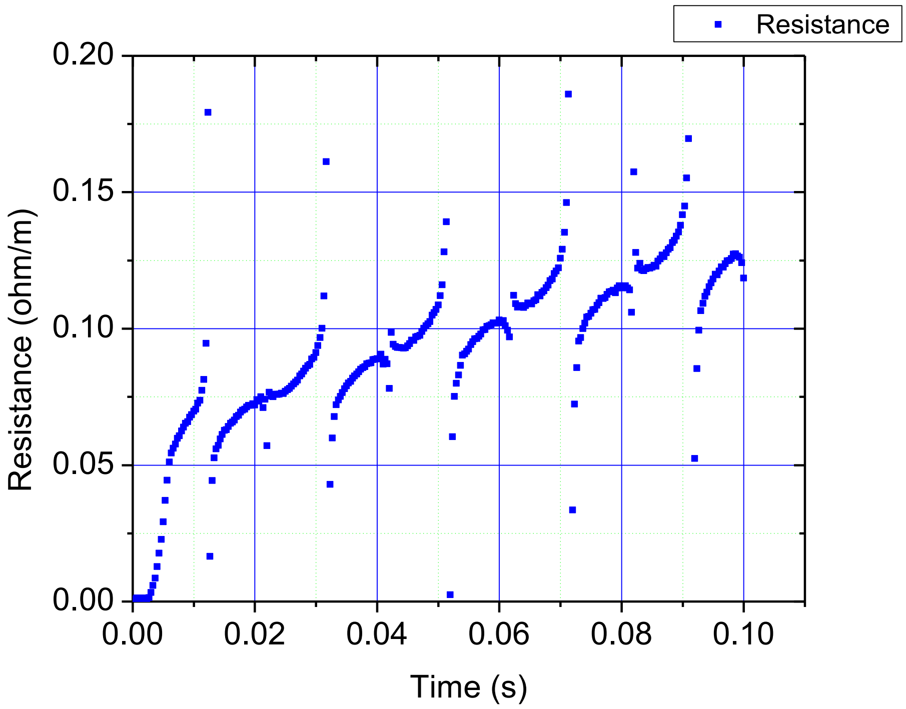

Figure 5.6 Resistance trend during the fault period

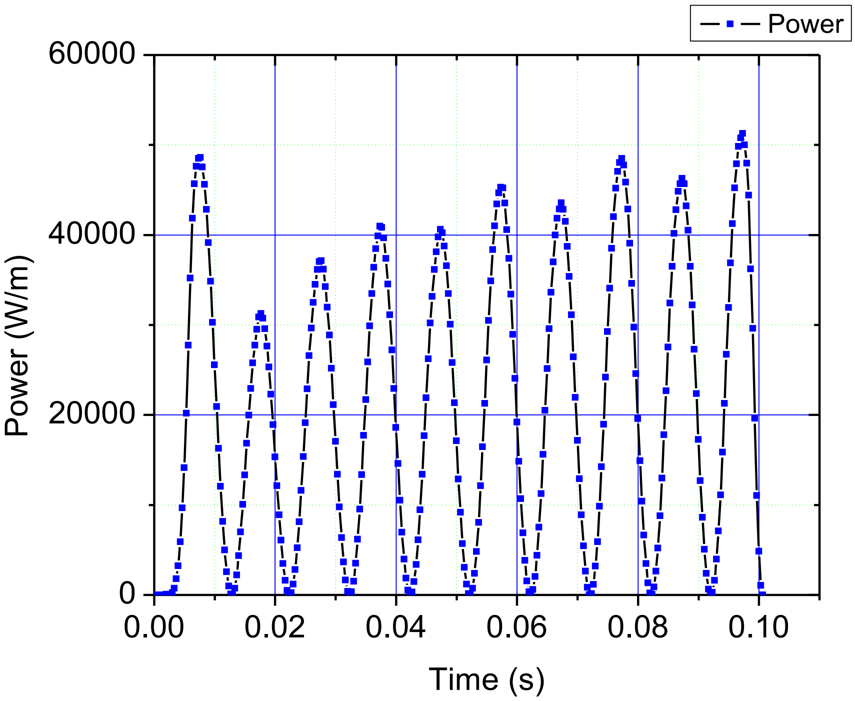

Figure 5.7 Power generated during the fault period of 0.1 s

5.3.3 AC loss characteristics of long straight AMSC tape

AC loss of SFCLs is another important parameter in the evaluation of SFCLs. Therefore, the AC loss characteristics of a 40 cm long straight segment of the 8602 type AMSC tape is measured with the cancellation coil technique (Figure 3.2). The measured AC losses curve is shown in Figure 5.8. The results consistency for different frequencies validates the measurement method. Furthermore, the AC losses curves of the AMSC tape are non-linear. This is quite different from that of the long straight Superpower tape, as shown in Figure 3.9 (c), which shows much better linearity. This can be attributed to the impact of the magnetic substrate, which tends to increase the AC losses of the superconductor in low transport current, thus leading to nonlinearity of the AC losses curve [115].

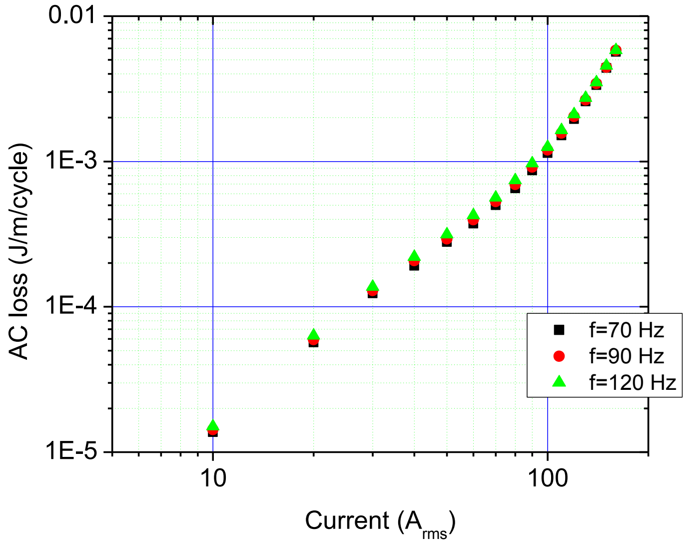

Figure 5.8 AC losses of a long straight tape used for building the SFCL

5.4 Design of the 220 V/300 A braid type SFCL prototype

5.4.1 Calculation of the amount of superconductor required for the SFCL prototype

To determine the superconductor amount required for the SFCL prototype, the tape strand number as well as the tape length in each strand needs to be calculated. As shown in Table 5.1, the rated current during normal operation is 300 A. Considering the minimum critical current of the superconductor tape is 241 A, the minimum tape number N_{sc} (an integer) needed can be calculated with Equation 5.5.

$$N_{sc} = \frac{I_{\max}}{I_c} = \frac{300\sqrt{2}}{241} = 1.76 \le 2 \tag{5.5}$$

where $I_{\max}$ is the maximum current during normal operation, I_c is the critical current of the superconductor tape and N_{sc} is the number of tape strands. Therefore, there should be at least two tapes connected in parallel in the SFCL prototype.

Furthermore, the tape length used for building the SFCL is determined by the maximum electric field the superconductor can withstand during a fault, which is

45 V/m, as calculated in Section 5.3.2. Thus, the minimum tape length needed for building the SFCL is

$$L_{sc} = \frac{220\ V}{45\ V/m} = 4.89\ m \tag{5.6}$$

Based on Equations 5.5 and 5.6, the total length of required superconductor can be obtained with Equation 5.7.

$$L_{tot} = 2 \times 4.89\ m = 9.78\ m \tag{5.7}$$

To sum up, for building a 220 V/300 A braid type SFCL prototype, at least two strands are needed and each strand length is at least 4.89 m.

5.4.2 Design optimisation of the SFCL prototype

To optimise the design of the SFCL, different characteristics of the SFCL design need to be taken into account carefully, such as the normal state impedance, AC losses and SFCL volume, etc. Therefore, the impact of different SFCL parameters such as substrate, coil diameter and tape separations are simulated and discussed in detail.

(1) Discussion concerning the impact of substrate orientation

Previous research shows that for a superconducting stack with a magnetic substrate, the orientation of the magnetic substrate tends to affect the AC losses of the superconductor [115-117]. Therefore, the impact of the substrate orientation on the AC losses of the braid type coil is also studied here. The AC losses of the braid type coils with parameters shown in Table 5.4 are simulated under different transport currents. Three types of magnetic substrate orientations are taken into consideration here and illustrated in Figure 5.9: back-to-back (BTB), back-to-front (BTF) and front-to-front (FTF).

The AC losses of the three types of coils are calculated with 2-D axi-symmetric models, which were introduced in Chapter 4. The simulation results are shown in Figure 5.10. Based on Figure 5.10, when I_{rms} is higher than 100 A, the AC losses of the FTF type coil are higher than that of the BTF type, which is again higher than that of the BTB type. However, when I_{rms} is lower than 100 A, the AC losses of the FTF type coil are far lower than that of the BTB and the BTF type coils.

Table 5.4 The parameters of the SFCL prototype

Parameters	Values
Diameter of SFCL cylinder/mm	80
Pitch of SFCL coil/mm	15
Tape to tape separation/mm	0.3
I_c/A	253
Winding number	2
Inner layer turn	6
Outer layer turn	6

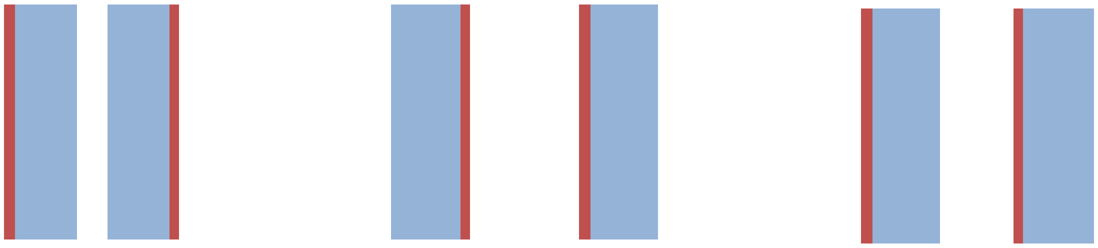
(a) (b) (c)

Figure 5.9 Schematic of the three types of substrate arrangements in the braid type coil: (a) back-to-back (BTB), (b) front-to-front (FTF) and (c) back-to-front (BTF). It is worth noting that the schematic are from the cross-section of the braid type coil, where the inner layer and outer layers are completely overlapped. Furthermore, for all the three schematics, the distances between the superconducting layers in each illustration are the same.

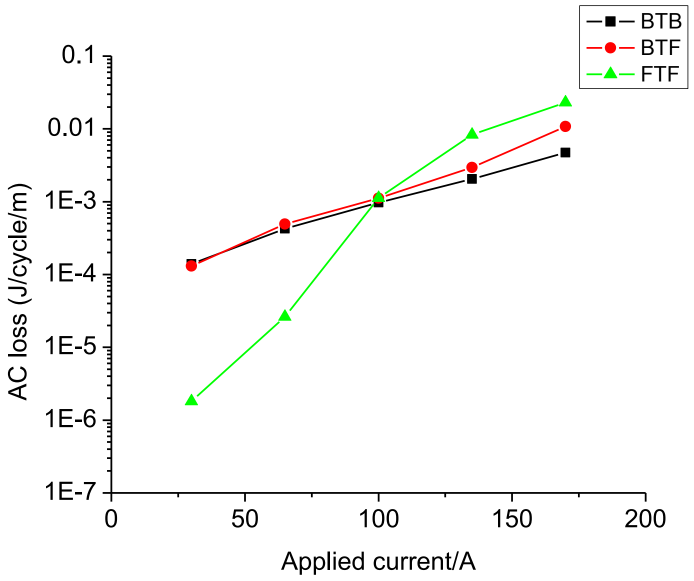

Figure 5.10 Simulated AC losses of the braid type SFCL coils with different substrate orientations of superconductor

To determine the impact of substrate orientation on the AC losses of the braid type SFCL, the AC losses of the SFCL with BTB and FTF type substrate orientation are extracted and analysed in detail. Considering that the BTF type substrate orientation is a mixture of the BTB and FTF type, as shown in Figure 5.9, the impact of the substrate orientation to its AC losses are not discussed here.

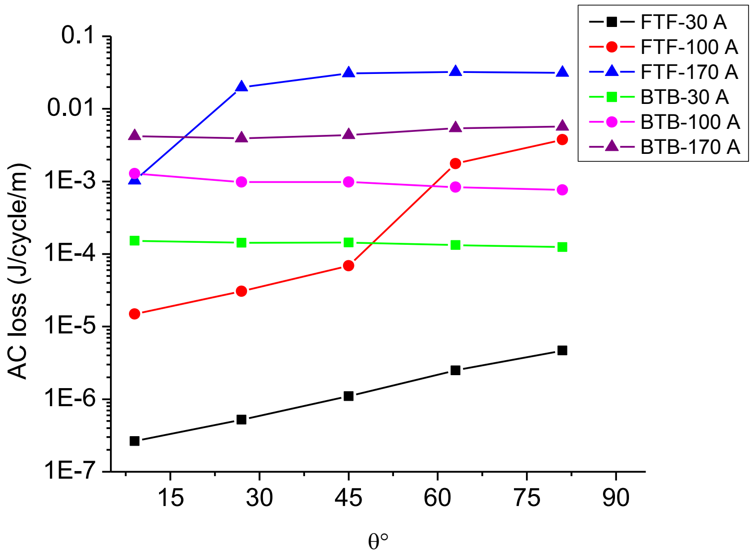

Figure 5.11 AC losses distribution along the different cross-sections of the ¼ part of the braid type coil with different applied currents (30 A, 100 A, 170 A)

As shown in Figure 5.11, for the FTF type coil, the AC losses of the superconductor increase with the increase of θ, and there is a limit for the increase of the AC losses at higher current levels, which increases gradually with the applied current. This AC losses trend is generally the same with that of the SFCL without magnetic substrates (Figure 4.9). The reason for the consistent trend is mainly because the magnetic substrate distributed on the outside of the overlapped superconductors in the FTF type coil, where the magnetic field generated by the inner and outer layer cancel each other. Therefore, the impact of the substrate on the magnetic field distribution is generally negligible, leading to little impact on the AC losses distribution of the braid type SFCL.

Conversely, the AC losses trend of the BTB type SFCL shows quite different characteristics: (1) at higher current levels, the AC losses of the BTB type SFCL are lower than that of the FTF type SFCL; (2) at lower current levels, the AC losses of the BTB type SFCL are higher than that of the FTF type SFCL; and (3) the AC losses of the BTB type SFCL shows little change with the increase of θ. To determine the reason behind this phenomenon, the AC losses in the substrate and superconducting layers in both low and high current excitation are extracted and compared, as shown in Figure 5.12 and 5.14.

Under a low transport current of 30 A_{rms}, as shown in Figure 5.12, the ferromagnetic loss is much higher than that of the HTS loss for both types of coils. Therefore, the AC losses of both coil types are dominated by the substrate ferromagnetic loss. Based on this conclusion, the ferromagnetic losses as well as the total losses of both types of coils are compared in Figure 5.13.

Figure 5.13 shows that the ferromagnetic loss of the BTB type SFCL is much higher than that of the FTF type SFCL. This is mainly because the substrate of the BTB type SFCL locates between the HTS layers, as illustrated in Figure 5.9(a), where the magnetic field is enhanced, leading to a higher ferromagnetic loss. However, for the FTF type SFCL, the substrate locates on the outside of the overlapped superconductors, where the magnetic field generated by the two superconducting layers cancel each other. Therefore, only a small magnetic field penetrates the substrate, which results in lower AC losses.

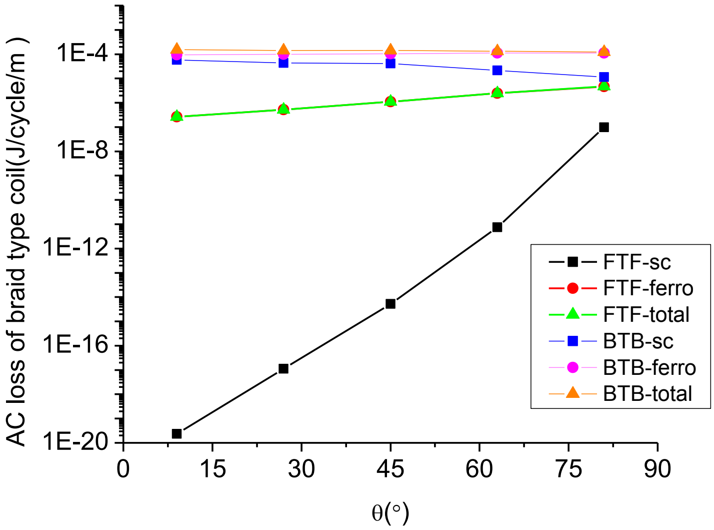

Figure 5.12 AC losses of the braid type coil with different substrate orientation under a transport current of 30 A_{rms} (a) FTF type coil, (b) BTB type coil

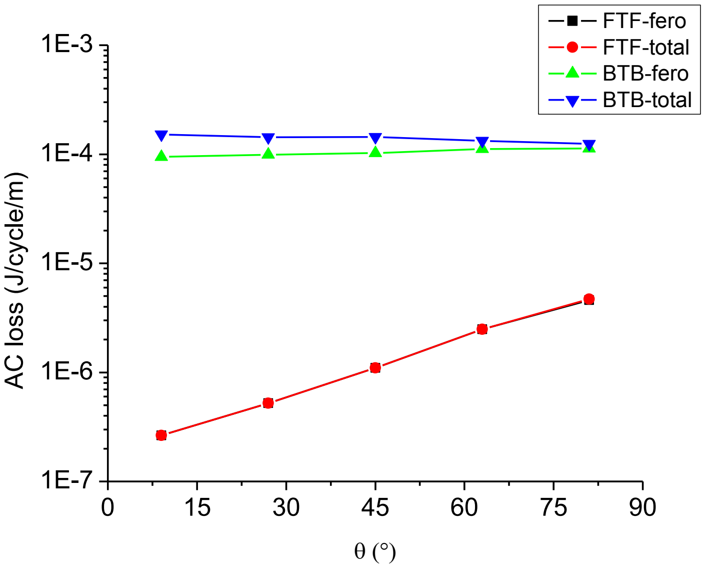

Figure 5.13 Comparison of the AC losses of the FTF type coil and the BTB type coil under a current of 30 A_{rms}

The AC losses of the FTF and BTB type SFCL under a transport current of 170 A are extracted and compared in Figure 5.14. Figure 5.14 shows that for a high current of 170 A, the HTS loss is the dominant loss for both types of SFCLs, which is much higher than that of the ferromagnetic losses for both cases.

Therefore, to determine the impact of the substrate on the superconductor loss of both types of coils under high transport currents such as 170 A_{rms}, the perpendicular magnetic field in the HTS layers are extracted and compared, as shown in Figure 5.15. Figure 5.15 shows that, due to the inhibition effect of the substrate on the magnetic field interactions between adjacent superconductors, the BTB substrate orientation tends to decrease the penetration depth of the perpendicular magnetic field, thus leading to lower HTS losses.

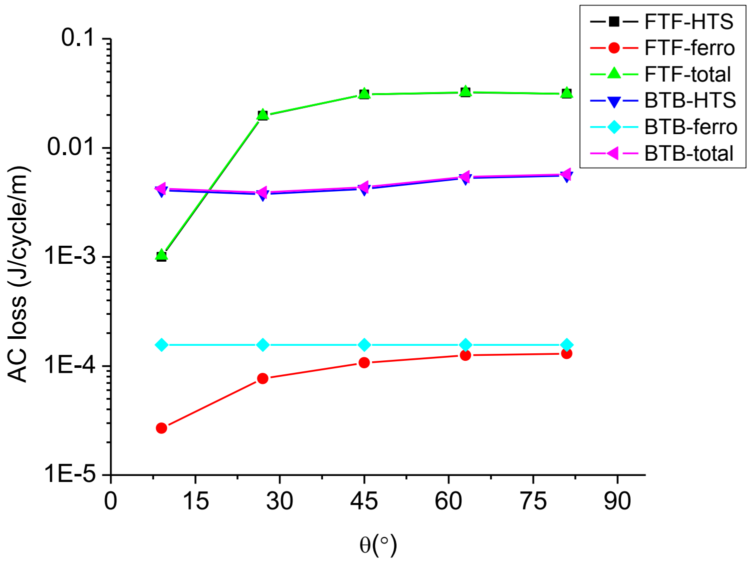

Figure 5.14 Comparison of the HTS loss, ferromagnetic loss and total losses for the FTF and BTB type SFCLs under an applied current of 170 A

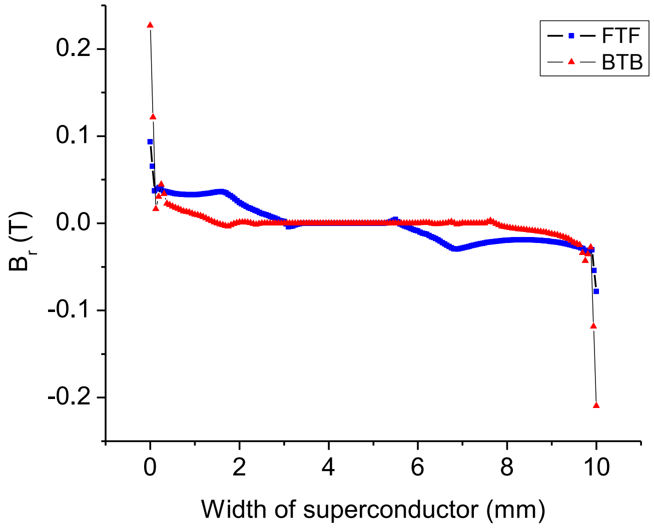

Figure 5.15 Comparison of the perpendicular penetration field in the superconductor layer when θ is 81° of the FTF and BTB type SFCLs

Considering that during normal operation, the current flowing through superconductor is far higher than 100 A_{rms}, the BTB type substrate orientation is chosen for the 200 V/300 A SFCL prototypes.

(2) Discussion concerning the impact of the SFCL prototype diameter

For the SFCL coil, the diameter tends to impact the volume of the SFCL. To determine the coil diameter, there are several aspects to be considered. Firstly, there is a minimum bending diameter limit when a superconductor is bent, which is 70 mm with greater than 95% I_c retention for the 8602 type AMSC tape. Secondly, due to the space limitation in substations, the SFCL diameter should be not too large, so as to satisfy the size requirements concerning the SFCL. It is worth noting here that the SFCL volume includes the low temperature dewar, superconducting element, insulation bushing and shunt resistor. In this work, for the calculation of the SFCL volume, only the superconducting element is considered for simplification.

The relationship between coil diameter and superconducting element volume can be expressed with Equation 5.8. Equation 5.8 is based on two equations: (1) the volume of the SFCL cylinder, which equals the bottom area times the height; (2) the length of superconductor per turn can be calculated with the pitch and the circumference of bottom circle of SFCL cylinder, as shown in Figure 4.1. Furthermore, Equation 5.8 is based on the assumption that the calculated superconducting element volume equals the volume of the SFCL bobbin, neglecting the volume of the superconductor windings. This is a reasonable assumption, because the superconductor thickness as well as the tape separations are far smaller than the diameter of the SFCL bobbin (≥70mm) and thus can be neglected.

$$V_c = \frac{\pi D^2 P_h L_{tot}}{8\sqrt{(\pi D)^2 + P_h^{\,2}}} \tag{5.8}$$

where V_c is the volume of the superconducting element of the SFCL, L_{tot} is the total length of superconductor in the SFCL, D is the diameter of the superconducting coil, P_h is the pitch of the superconducting windings.

Considering the diameter of a coil is generally much larger than the pitch, Equation 5.8 shows that the volume of the SFCL increases almost linearly with its diameter. Therefore, to obtain a lower SFCL volume, a smaller diameter is preferred. However, as mentioned previously, the minimum diameter with less than 5% I_c degradation is 70 mm, which also needs to be taken into account in the design.

(3) Discussion concerning the impact of coil pitch

Pitch is a significant parameter to the braid type coil, since it not only influences the AC losses but also has an impact on the volume as well as the inductance. All these parameters are discussed in detail here.

To study the impact of pitch on the AC losses of the braid type coil made of AMSC tape, a model with the specifications shown in Table 5.5 are simulated. The simulation results are shown in Figure 5.16. Figure 5.16 indicates that the AC losses increase gradually at high currents such as 170 A_{rms}, but shows negligible change in low currents of 100 A_{rms} and 30 A_{rms}. Based on these results, if the current during normal conditions is high enough (≥ 170 A), the pitch should be as small as possible to decrease the AC losses of the SFCL. However, if the normal operating current is far lower than 170 A, then the change of pitch has a negligible impact on its AC losses.

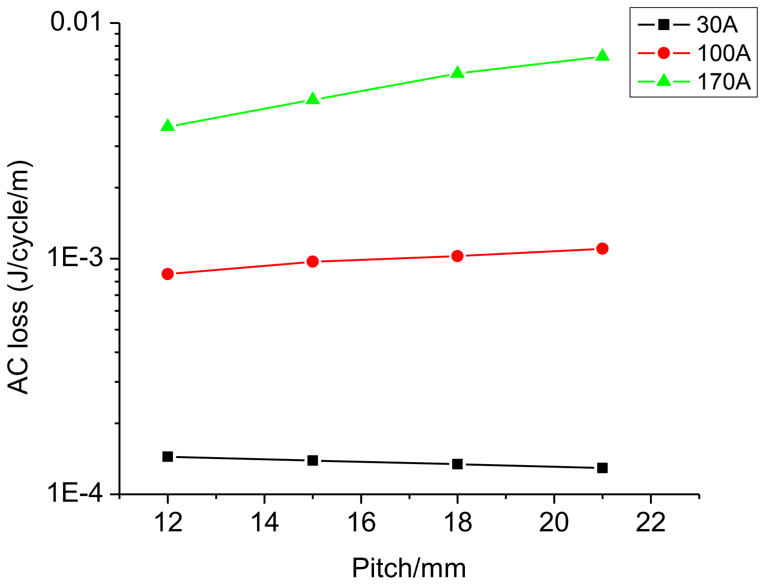

Figure 5.16 Impact of pitch on the AC losses of the BTB type SFCL

Table 5.5 Parameter of the simulation model

Parameters	Values
Diameter of SFCL cylinder/mm	80
Pitch of SFCL coil/mm	12,15,18,21
Tape to tape separation/mm	0.3
I_c/A	253
Winding number	2
Inner layer turn	6
Outer layer turn	6

In addition, the impact of pitch on the SFCL volume can be calculated with Equation 5.8, which shows that the volume of the superconducting coil increases gradually with the increase of pitch. Considering that the diameter *D* is typically much larger than the pitch, the volume of a SFCL increases almost linearly with the pitch of the superconductor. Therefore, from the point of view of decreasing the SFCL volume, the pitch should be as small as possible.

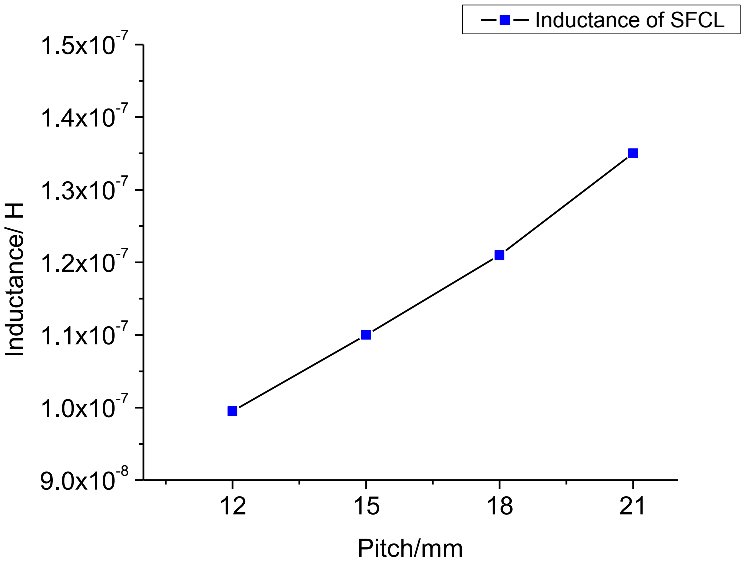

Figure 5.17 Impact of pitch on the inductance of the SFCL under an applied current of 170 A_{rms}

Finally, the impact of coil pitch on the inductance of the SFCL was calculated based on the simulations conducted for calculating the AC losses, and the results are shown in Figure 5.17. Figure 5.17 shows that the inductance of the BTB type SFCL increases with the increase of pitch. Therefore, from the point of view of decreasing the inductance of the SFCL, a lower pitch is preferable.

(4) Discussion concerning the impact of tape separation between adjacent tapes

The tape separation of the braid type coils might have an impact on the AC losses and inductance of the SFCL prototype. To evaluate the impact of pitch on the AC losses, braid type coils with different pitches (0.3, 1.3, 2.3 mm) are studied with the 2-D simulation models proposed in Chapter 4. The specific parameters of the SFCL are shown in Table 5.5 and the calculation results are provided in Figure 5.18. Figure 5.18 shows that there is negligible change in AC losses for the braid type coil with the increase of tape separation under different applied currents (30 A, 100 A, 170 A). This result is quite different from the conclusion reached for the braid type coil made of the SuperPower tape. This can be attributed to the effect of the magnetic substrate of the AMSC tape. With the back-to-back arrangement of the inner layer coil and outer layer coil, the magnetic field interaction between the two layers are weakened greatly by the magnetic substrate, thus leading to a negligible change in AC losses.

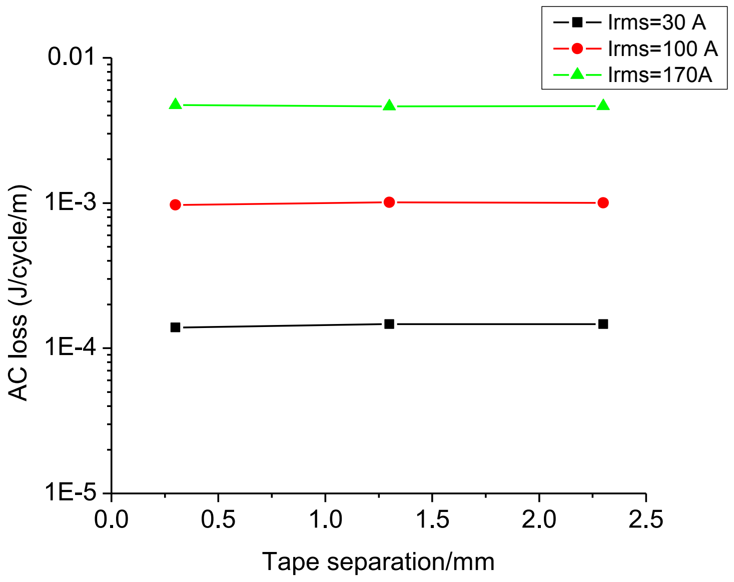

Figure 5.18 AC losses of the braid type coil with different tape separations of 0.3, 1.3, 2.3 mm

Furthermore, for resistive type SFCLs, the inductance of SFCLs should be small enough to reduce the impact of the SFCL on the power grid during normal operation.

To obtain a low inductance, the tape separation between the inner layer and outer layer should be low enough, so that the magnetic field generated by the inner layer and outer layer can be cancelled completely. To provide a quantitative analysis, the impact of tape separation on the SFCL inductance is also studied with the simulations, as shown in Figure 5.19. Figure 5.19 clearly indicates that the increase of tape separation tends to increase the SFCL inductance. Therefore, in the design of a SFCL, the tape separation of the SFCL coil should be low enough.

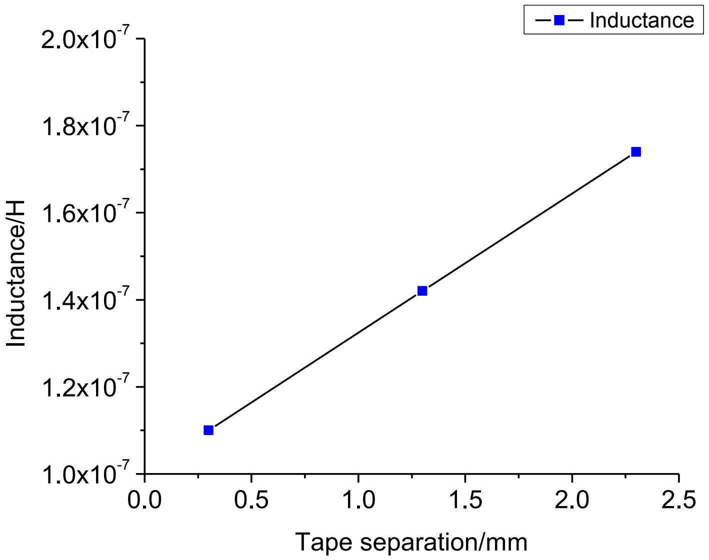

Figure 5.19 Impact of tape separation on the inductance of the SFCL

(5) Impact of different coils arrangements on the SFCL prototype

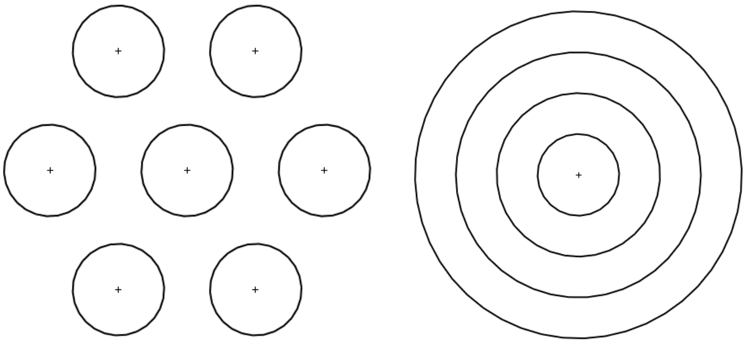

(a) (b)

Figure 5.20 Arrangement methods of the braid type coil: (a) distributed arrangement; (b) nested arrangement

In a practical braid type SFCL, many braid coils need to be arranged and connected together. However, due to the space limitation in substations, these coils should be arranged in a compact way. Generally speaking, for the braid type coil, there are two different arrangement methods, as shown in Figure 5.20.

In the distributed arrangement, different coils of the same dimensions are placed vertically on the same plane, with the axis separations of adjacent coils equaling each other, as shown in Figure 5.20(a). In the nested arrangement, superconducting coils with different diameters but the same axis are nested together, like Russian dolls, as shown in Figure 5.20(b). The distributed arrangement shown in Figure 5.20 (a) has previously been used in the German CURL 10 project, where BSCCO-2212 bulk material was used for building the SFCL [16]. That is mainly because for a modular superconductor element, the distribution arrangement leads to a simpler manufacturing process.

For the application of a braid type coil made of 2G HTS tape, both arrangements can be considered. However, considering the space limitation in substation, the nested arrangement, which occupies less space, is preferable. Therefore, for the SFCL prototype, the nesting structure was used.

5.4.3 Final SFCL prototype design

Based on the discussion in the previous section, the final design of the braid type coil was determined. The SFCL is composed of two solenoidal coils that are arranged in the nested arrangement. Furthermore, the BTB type substrate arrangement was used in both coils. The detailed parameters of the prototype are summarised in Table 5.6.

Table 5.6 Detailed parameters of the braid type coil

	Coil 1	Coil 2
Winding number/mm	2	2
Turn per winding	8 (inner) 8 (outer)	8 (inner) 8 (outer)
Diameter/mm	80 (inner)	113 (inner)

	82 (outer)	115 (outer)
Pitch/mm	18	18
Tape length/m	4.08	5.74
Rated voltage/V	91.5	128.5
Tape separation/mm	1	1
Substrate orientation	BTB	BTB
Coil arrangement	Nested structure	

5.5 Building of the 220 V/300 A SFCL prototype

Based on the design specifications shown in Table 5.6, the SFCL was built, as shown in Figure 5.21. The building of the prototype was mainly composed of three processes: 1) design and 3-D printing of the bobbin; 2) wounding of the coils; 3) soldering of connectors to the superconducting coils.

In the bobbin design, 3-D printing was used, which used acrylonitrile butadiene styrene (ABS) material. To better fix the superconductor tape in the bobbin, two long solenoidal slots were designed in the outside surface of the bobbin. During the fabricating process, the superconductor tapes are fitted into the slot in the bobbin, so as to fix the windings. Furthermore, to guarantee the insulation between the inner winding and outer winding, Kapton tape was placed between them. Finally, the ending connecter was designed to provide a connection between the superconducting winding and the circuit line. Similar to that introduced in Section 3.1, the end connector was also based on the copper plate and copper braid. The copper plate was used as the interconnection between the superconductor and the copper braid. During the fabrication process, both the copper braid and the superconducting windings were soldered onto the copper plate before the copper plate was fixed on the bobbin.

In addition, to avoid the movement of the tape in the liquid nitrogen, which might be generated by the different shrinkage (thermal contraction) of different materials, Kapton tape was also used to fix the outside superconducting wire to the bobbin.

(a) (b) (c) (d)

Figure 5.21 Braid type SFCL: (a) physical picture of coil 1; (2) physical picture of coil 2; (c) schematic diagram of bobbin in coil 1; (d) schematic diagram of bobbin in coil 2.

5.6 Test of the braid type SFCL prototype

After completing the fabrication of the SFCL prototype, different properties of the SFCL were tested experimentally such as critical current, current limiting property, AC losses and recovery characteristics.

5.6.1 The critical current of the SFCL prototype during normal operation

The critical current of the four windings in the SFCL prototype were measured during the experiment. The critical current of the inner winding of coil 1, outer winding of coil 1, inner winding of coil 2, outer winding of coil 2 are 248.7, 251.2, 247.7, 250.1 A respectively. Considering the minimum critical current of the AMSC tape is 241 A, the normal operational current in these winding should still be less than 241 A to reduce the AC losses and guarantee the stability.

5.6.2 The AC losses of the SFCL

The AC losses of the braid type coil were measured experimentally with the method introduced in Chapter 4. The results are shown in Figure 5.22, where the AC losses of a single long straight tape are also presented as a reference. Figure 5.22 shows that the new type SFCL exhibits much higher AC losses than that of single straight tape. This might be caused by the magnetic field interactions between the inner coil and the outer coil. Although each coil is wound to be non-inductive, there are still magnetic fields both in and outside the coil, especially the locations where the inner layer and outer layers have a large misalignment distance. These magnetic fields will penetrate the superconductor tape and thus increase the AC losses. Based on this point, in the design of a braid type SFCL with a nested structure, relatively large coil separation should be considered to avoid the high AC losses.

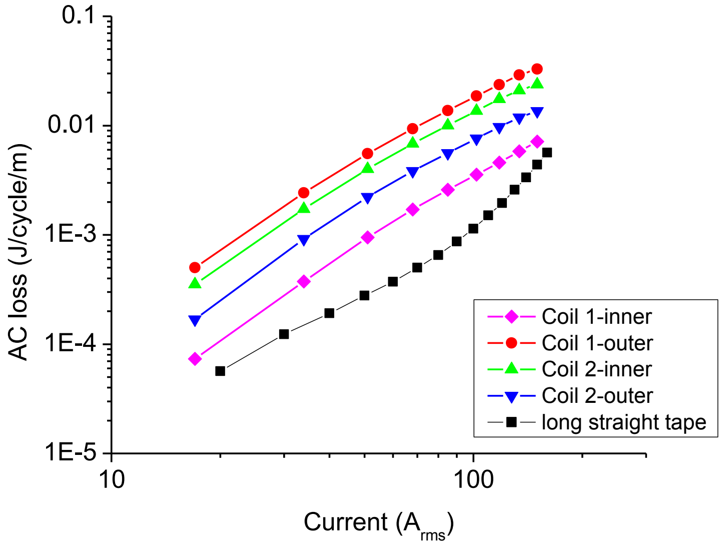

Figure 5.22 Experimentally measured AC losses of the SFCL prototype

5.6.3 Current limiting performance of the SFCL

To measure the current limiting performance of the SFCL prototype, different voltages were applied to the SFCL in fault conditions, as introduced in Section 3.2.2. However, it was found that the experiment system is unable to test the SFCL prototype under rated voltage of 220 V. Therefore, for high voltage fault tests, the prototype had to be separated apart, thus the two coils can be measured separately. There were two specific reasons for the infeasible test of the SFCL prototype under 220 V fault voltage. Firstly, it was mainly because the capacity of the transformer is 80 kVA only. However, the SFCL requires during the fault period is about 160 kVA during a fault period, which greatly exceed the capacity of the designed experiment system. Another limitation was the limitation of vacuum circuit breaker in the line that connected the university substation and the lab transformer, which was designed to be 63 A under voltage 400 V. Although during fault conditions, a load higher than the transformer capacity could be draw from power grid for a short periods, this could only be possible with a low transformer output voltage, instead of voltage level of 220 V. For low voltage ratio such as 440 V/220 V, the fault current in the primary side is higher than 1500 A, which sudden triggers the vacuum circuit breaker.

Considering the series-connection of the two coils and the superconductor length in each coil (4.1 m and 5.7 m for the coil 1 and coil 2 respectively), coil 1 and coil 2 will withstand 91.5 V and 128.5 V, respectively, in the case of a fault with applied voltage 220 V. The experimentally measured current limiting trends of the two coils are summarised in Table 5.7 and Table 5.8. The two Tables show that, for both coil 1 and coil 2, the prospective fault current can be limited to a current lower than 2000 A under different fault voltages (12.5 V, 25 V, 50 V, 100 V or 128.5 V), which are far lower than the maximum limited fault current of 11.25 kA. For example, for coil 1, when the fault voltage was 100 V, the prospective fault current was effectively limited to 963 A, which satisfied the requirements concerning the maximum limited fault current. For coil 2, when the fault voltage is 128.5 V, the prospective fault current is limited to 985 A, which also satisfied the requirements concerning the maximum limited fault current.

Finally, the assembled prototype was tested under several voltage levels that are lower than 220 V, as summarised in Table 5.9. Table 5.9 shows that the prospective fault current could be effectively limited by the prototype under voltage levels lower than or equal to 150 V.

Table 5.7 Current limiting test of coil 1

Rated voltage/V	Prospective fault current/ kA	Limited fault current/A
12.5	3.7	693
25	7.4	650
50	14.8	804
100	29.6	963

Table 5.8 Current limiting test of coil 2

Rated voltage/V	Prospective fault current/ kA	Limited fault current/A
12.5	3.7	532
25	7.4	576
50	14.8	708
100	29.6	920
128.5	38	985

Table 5.9 Current limiting test of the whole coil

Rated voltage/V	Prospective fault current/ kA	Limited fault current/A
50	14.8	414
100	29.6	544.5
150	44.4	623.6

To provide an illustration concerning the current limiting process of the 220 V prototype, the test results under rated voltage of 150 V are shown in Figure 5.23 and 5.24. Figure 5.23 shows that the SFCL begin to limit the fault current in the first fault cycle, where the prospective fault current 44.4 kA_{rms} is limited to 1750 A_{max}. In the final cycle the current is limited to 882 A_{rms}. Figure 5.2.4 shows that for both coil 1 and coil 2 of the prototype, the voltage in the inner winding and that in the outer winding are generally the same, which indicates the quench homogeneity of superconductors in both coils. Furthermore, the ratio of coil 2 voltage to coil 1 voltage is 1.39, which is consistent with the superconductor length ratio of the two coils ($5.7/4.1 \approx 1.39$). This ratio consistency means that the degrees of quench in both coils are also the same.

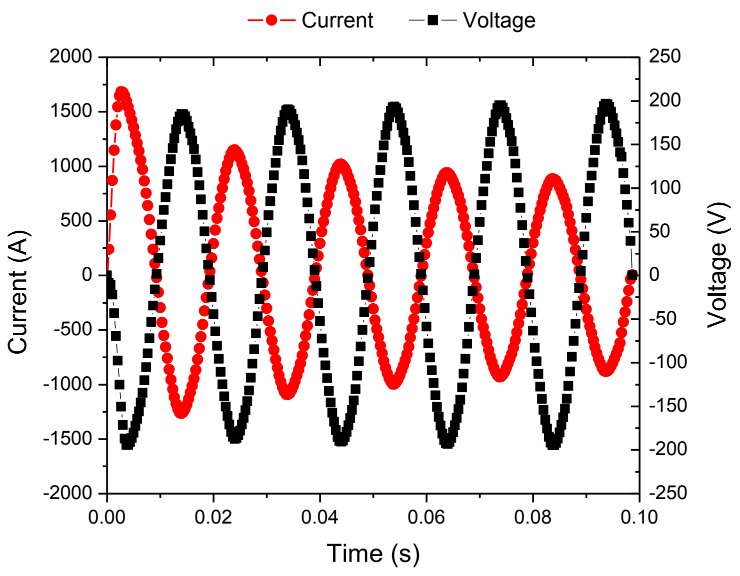

Figure 5.23 The Current and voltage of 220 V SFCL prototype under 150 V voltage test

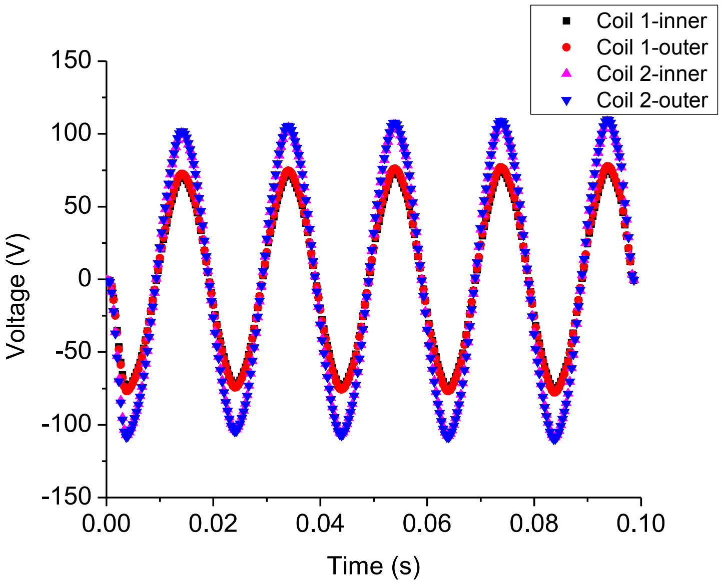

Figure 5.24 The voltages across each winding of the SFCL prototype under 150V voltage test

5.6.4 The recovery characteristics of the SFCL prototype

The recovery time of all the windings in the 220 V SFCL prototype are also extracted and summarised in Figure 5.23 with the method introduced in Section 3.3.2. Figure 5.23 shows that, in the tests concerning the whole prototype, all the windings can recovery in less than 5 seconds under different voltage levels (50 V, 100 V, 150V), which verifies that the built SFCL prototype satisfy the requirement concerning recovery time. However, since the prototype cannot be tested with the experiment system under 220 V, it is still unknown the recovery time in fault under rated voltage.

Furthermore, the experiment results show that the inner layer and outer layer recover almost in the same time in fault cases. This indicates that, for the SFCL prototype built, the overlapping structure has negligible impact to the recovery time for the prototype built.

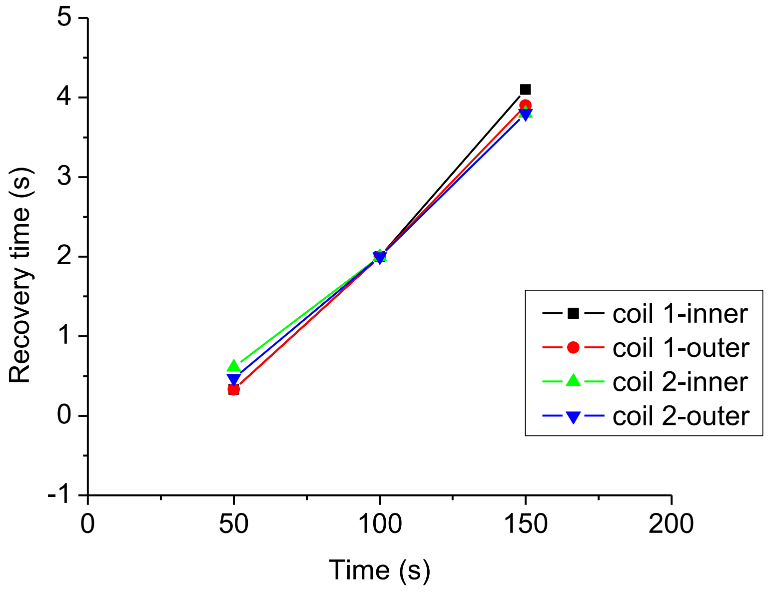

Figure 5.23 Recovery time of the 220 V SFCL prototype under different line voltages (12.5 V, 25 V, 50 V and 100 V)

5.6.5 Summary of the built SFCL prototype

Based on the discussed analysis, the built SFCL prototype can satisfy the requirements concerning current limiting and recovery time, however, the AC losses of the prototype were much higher than expected. This finding indicates in the design of SFCL, the diameter of the coils that are nested together should also be taken into account seriously during the design of the SFCL prototype, since it will greatly increase the AC losses.

Based on the voltage data of all the experiments, the inner winding and outer winding of both coils quench simultaneously, which indicates homogeneous quench of the SFCL prototype. After all the experiments, the I_c of all the windings were measured again, which showed no degradation.

5.7 Conclusions

In this chapter, a 220 V/300 A braid type SFCL was designed, built and tested. As a preliminary test, the performance of a single straight sample was firstly tested to provide guidance for the design of the 220 V prototypes.

To optimise the design, the impacts of different factors on the performance of a SFCL were discussed in detail. Results shows that: (1) both the substrate orientation and coil pitch have a serious impact on the AC losses; (2) the coil diameter, pitch and coil arrangement have a significant influence on the volume of a SFCL; and (3) the pitch and tape separation are the two important factors that determine the inductance of a braid type SFCL.

Subsequently, the 220 V prototype was built based on 3-D printing and manually soldering. The prototype was composed of two cylinders, which were nested together. Experimental tests verified the current limiting and recovery performance of the prototype. However, the AC losses of the prototype were higher than what we expected. Analysis showed that the distance between the inner coil and outer coil is the key reason that increased the AC losses.

The work in this chapter provided a preliminary study concerning the design and building of a braid type coil, which provides valuable and useful reference for any industry SFCLs taking using of braid type solenoid structure.

Chapter 6 Simulation of the current limiting performance of SFCLs

With the increase of electricity demand from a range of sources with higher loads and the changes of the power grid structures, the fault current can be extremely high and may exceed the capacity of circuit breakers. However, with the application of SFCLs, fault currents can be limited by superconductors, which transition from the superconducting state to the resistive state. If a fault current is limited within the capacity of circuit breakers, it can be cut off successfully. Therefore, the current limiting performance of SFCLs is an important aspect to be considered in evaluating whether a SFCL meets the requirements of the power grid or not. An operational SFCL should limit the fault current to a certain range with its temperature not exceeding the upper limit (usually 300 K). Therefore, it is very important to study the transients of a power system with SFCL installed, as well as the characteristics of the SFCL during a fault period.

To date, different models have been proposed for simulating the current limiting performance of SFCLs, which are previously introduced in Chapter 2. In this chapter, an electro-magneto-thermal model is proposed and built by using COMSOL. To validate the proposed model, the current limiting performance of a 220 V resistive type SFCL was simulated.

6.1 Introduction of the electro-magneto-thermal model

The quench process is not only an electro-magnetic process, but also a thermal one. Therefore, the SFCLs need to be simulated by coupling an electro-magnetic model and a thermal model together. This is realised here with the PDE module and thermal module in COMSOL. Furthermore, to simplify the SFCL model, 2D cross-section of superconductor is used. For the electro-magnetic model, the cross-section of a superconductor tapes is simulated based on 2-D *H* formulation. For the thermal model, the heat transfer in the cross-section of the superconductor is simulated with the general heat equation. In both models, it is assumed that the superconductor is infinitely long and homogeneous along in the length. The details of the two models are:

(a) Electro-magnetic model

For the electro-magnetic model, 2-D H formulation was used for solving the electro-magnetic properties of the superconductor. The current was assumed to flow in the length direction only and thus, the magnetic field exists in the cross-section plane only.

For describing the *E-J* relationship of each layer, Equation 6.1 was used.

$$E = \rho * J \tag{6.1}$$

where E and J are the electric field and the current density of the superconductor respectively, and ρ is the resistivity, which is a function of temperature in the model.

By combining Faraday's law, Ampere's law and Equation 6.1, a partial differential equation can be obtained:

$$\mu_0 \frac{\partial \mu_r}{\partial t} H + \mu_0 \mu_r \frac{\partial H}{\partial t} + \nabla \times (\rho \nabla \times H) = 0 \tag{6.2}$$

where μ_0 is the vacuum permeability, μ_r is the relative permeability, and H is the magnetic field strength.

For the superconducting layer, the *E-J* power law is usually used to describe the *E-J* relationship of the superconductor, as shown in Equation 6.3.

$$E = E_0 \left(\frac{J}{J_c} \right)^n \tag{6.3}$$

However, due to the quench state of a superconductor during a fault, the *E-J* power law cannot be used to simulate the superconductor directly. To date, different equations have been proposed to describe the *E-J* relationship of a superconductor during quench. Joseph Duron proposed a black-box model, which took a superconductor as the parallel connection of a non-linear resistor, representing the superconducting material, and a normal resistor, meaning the metallic sheath [80, 118]. François Roy described the electrical properties of superconductor with a non-linear resistivity, which varied with current density and temperature [77]. W. Paul defined the *E-J* relationships of three operating states of superconductor: 1) the superconducting state, 2) flux flow state and 3) the normal conductor state with $E \sim j^{\alpha}$, $E \sim j^{\beta}$ and $E=\rho j$, respectively [119].

For simulation of the *E-J* characteristics of the superconductor used in this work, two equations were considered firstly. One is the modified *E-J* power law with an upper limit, as shown in Equation 6.4, the second one is Duron's black-box model, as shown in Equations 6.5 and 6.6. However, during the calculations, it was found that both equations easily lead to the non-convergence.

In order to improve the convergence of computation, a new *E-J* relationship with a smooth transition from the superconducting state to the normal state is proposed in this work. The new relationship is based on an exponential function, which is shown in Equations 6.7 and 6.8, and two fixed points of the modified *E-J* power law (Equation 6.4)--(J_c, E_0/J_c) and ($\alpha * J_c$, ρ_{norm}), where α is a coefficient that determines the trend of superconductor resistivity with current density. The first is the point where the current density equals the critical current density, whilst the second one corresponds to the point where the resistivity of the superconductor equals normal resistivity.

$$\rho_{sc1} = \min\left(\rho_{norm}, \frac{E_0}{J_c}\left(\frac{J_z}{J_c}\right)^{n\_value-1}\right) \tag{6.4}$$

$$\rho_{cc} = \frac{\rho_{sc} \times \rho_{norm}}{\rho_{sc} + \rho_{norm}} \tag{6.5}$$

$$\rho_{sc} = \frac{E_0}{J_c}\left(\frac{J_z}{J_c}\right)^{n-1} \tag{6.6}$$

where ρ_{cc} is the resistivity of the coated conductor, ρ_{sc} is the resistivity of the superconductor, ρ_{norm} is the resistivity of the superconductor at room temperature, E_0 is 1 μV/cm, J_c is the critical current of the superconducting layer, which is a function of temperature, and J_z is the current that flows through the superconducting layer.

The equations of this new *E*-*J* relationship are shown in Equations 6.7-6.10.

$$E_z = \rho_{sc2} * J_z \tag{6.7}$$

$$\rho_{sc2} = \begin{cases} \rho_{norm} * e^{-\left(\frac{|J_z| - \beta * J_{cx}}{\gamma}\right)^2} & , 0 \le J_z \le \beta * J_{cx} \\ \rho_{norm} & , \beta * J_{cx} \le J_z \end{cases} \tag{6.8}$$

By taking the two points into Equation 6.8, the two coefficients *β* and *γ* can be solved as:

$$\beta = \alpha \tag{6.9}$$

$$\gamma = \frac{(\beta - 1) \times J_{cx}}{\sqrt{-\ln\left(\frac{E_0}{J_{cx} \times \rho_{norm}}\right)}} \tag{6.10}$$

where *β* and *γ* are the coefficients that are used to define the new *E*-*J* relationship of the superconductor. J_{cx} is the critical current density of the superconductor, which is usually taken as a function of temperature and magnetic field.

As shown in Equations 6.7-6.10, the only variable of the new *E*-*J* relationship is *α*. The physical basis of this new *E*-*J* relationship is that the quench process is basically a process of heat dissipation. When the current is smaller than the critical current, the electric field on the superconductor is very small, which can be derived from the point of (J_c, E_c / J_c) and Equations 6.7 and 6.8, therefore the heat dissipation can be neglected. However, when the current increases above the critical current, the electric field will increase exponentially, which leads to more heat generation. Nevertheless, the electric field will not always increase exponentially, because finally the normal resistivity of superconductor will be reached, after which the electrical field increases linearly with current density. In this work, to express the *E-J* relationship of the superconductor more accurately, α of the new *E-J* relationship was chosen to make the *E-J* relationship as close as the modified *E-J* power law. The coefficient α of the new *E-J* relationship is taken as:

$$\alpha = 1.15 * \left(\frac{\rho_{norm} * J_{cx}}{E_0} \right)^{\frac{1}{n\_value - 1}} \tag{6.11}$$

where *n*_value is taken as 31, which is also used in the simulations.

To better illustrate the new *E-J* relationship, ρ-*J* curves of the new *E-J* relationship are compared with that of the modified *E-J* power law and Duron's equation. As shown in Figure 6.1, there is only a minor difference between the three curves when the current is lower and slightly higher than the critical current J_{cx}. Then with the increase of the current density, the slope of the new *E-J* relationship curve and Duron's equation curve become smaller to that of the *E-J* power law curve. Considering the fact that the superconducting layer is sandwiched between non-superconducting layers, most current shunts to the non-superconducting layer when the resistivity of the superconductor increases to a high value, which leads to little heat dissipation in the superconductor layer. Therefore, the reduced slope of the new *E-J* curve has little influence on the quench simulation.

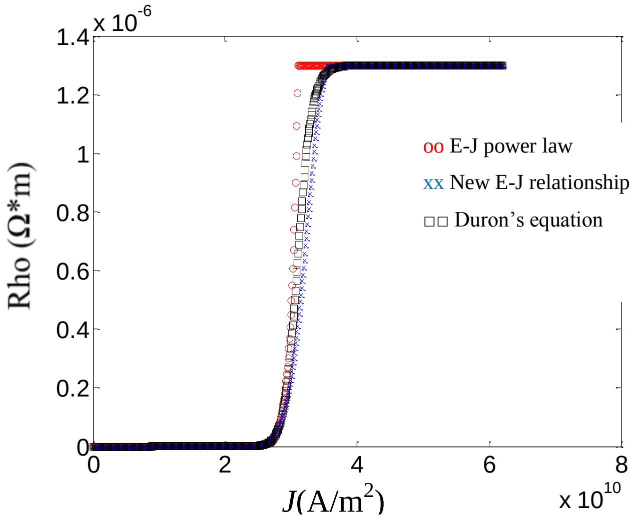

(a) $J_c(T)=J_{c0}$

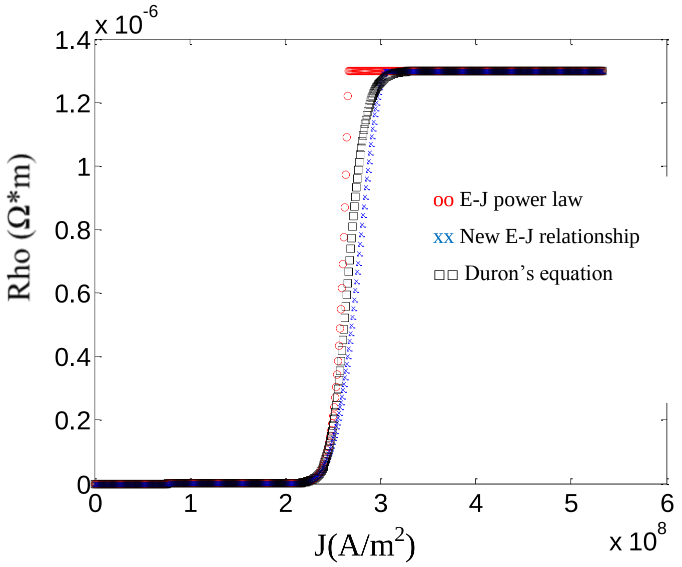

(b) $J_c(T)=J_{c0}/10^2$

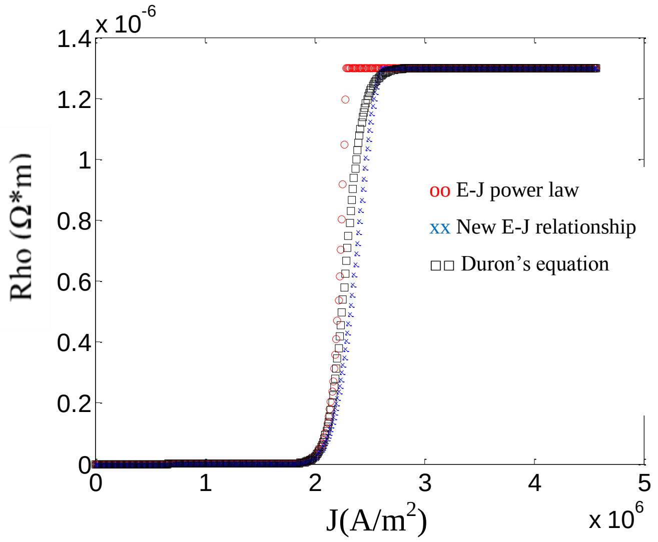

(c) $J_c(T)=J_{c0}/10^4$

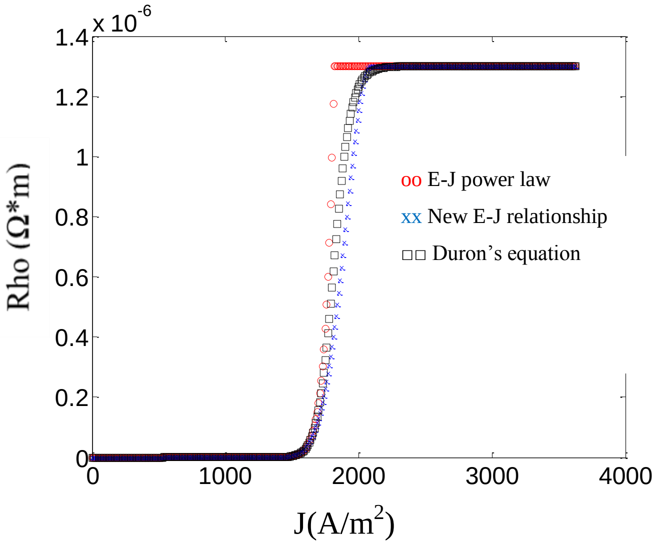

(d) $J_c(T)=J_{c0}/10^7$,

Figure 6.1 Comparison of different *E-J* equations

Furthermore, it is worth noting that J_c is a function of temperature and is expressed with Equation 6.12 as:

$$J_c(T) = J_{c0} * \left(\frac{T_c - T}{T_c - T_0} \right)^{1.5} \tag{6.12}$$

where T_c is the critical temperature of the superconductor, which is regarded as 92 K, T_0 is the temperature of liquid nitrogen, which is taken as 77 K.

(b) Thermal model

To calculate the heat transfer process during quench, a thermal equilibrium equation was built, as shown in Equation 6.13,

$$Q = \rho_m C_p \frac{\partial T}{\partial t} - \nabla(-k\nabla T) = E_z J_z \tag{6.13}$$

where Q is the power density in the superconductor, ρ_m is the density, C_p is the heat capacity, k is the thermal conductivity.

In order to simulate the physical process of heat transfer from the superconductor tape to the liquid nitrogen, where the SFCL is placed, a heat transfer equation (Equation 6.14) is applied to the surface of the superconductor [77].

$$\hat{n} \cdot (k_i \nabla T) = h(T_S - T_0) \tag{6.14}$$

where h is the convective heat transfer coefficient, which can be found in detail from [77], and T_s is the temperature of the superconductor surface.

(c) Coupling of the electro-magnetic model and thermal model

During the simulations, the electro-magnetic model and the thermal model were coupled together for calculating the characteristics of superconductors during quench. As shown in Figure 6.2, the calculation results of the electro-magnetic model E_z and J_z were used as the inputs of thermal model. Also, the calculation results of the thermal model *T* was used as an input parameter of the electro-magnetic model. Due to the powerful ability of COMSOL in solving the coupled problems, the two models can be coupled and calculated simultaneously, which produces more precise results compared with the method based on a fast-forward scheme [80].

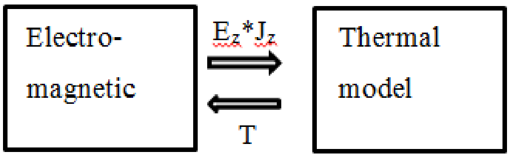

Figure 6.2 Coupling between the electro-magnetic model and the thermal model

6.2 Coupling of the SFCL model with the power system model

To simulate the performance of a SFCL in a power system, the SFCL model needs to be coupled into a power system model. Two different methods are considered. One is coupling the SFCL built with COMSOL and a power system model built with MATLAB/Simulink, the other one is using multiple modules in COMSOL.

Considering the accuracy of simulation, the second method was used, as illustrated in Figure 6.3. In each calculation step, the current flowing through the superconductor tapes of the SFCL prototype is transferred from the system model to the superconductor model to calculate the electrical and thermal characteristics of the superconductor tapes. Also, the resistance of the YBCO layers and the resistance of the metal layers are transferred from the superconductor model to the power system model to continuously calculate the response of the power system.

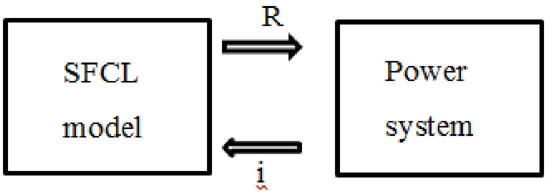

Figure 6.3 Coupling of the SFCL model and power system model

6.3 Validation of the proposed model

To validate the proposed model, it is used for simulating a 220 V resistive SFCL prototype built with 2G HTS and the simulation results are compared with the experimental results. The details of the prototype, the fault experiment, the simulation model and comparison between experimental and simulation results are provided below.

(a) Introduction of the SFCL prototype

The SFCL prototype, which is shown in Figure 6.4, consists of 16 elements connected in series. Each element contains four superconductor tapes and an external 180 mΩ shunt resistor, which are connected in parallel, as illustrated in Figure 6.5 [120]. The tape used in the SFCL prototype is American Superconductor’s 344S tape, with a critical current of 72±2A, a width of 4.4 mm and a thickness of 0.15 mm. The parameters of the tape are shown in Table 6.1 [121]. The effective length of each tape is 0.4 m, therefore, the total length of tape used in the SFCL prototype is 25.6 m.

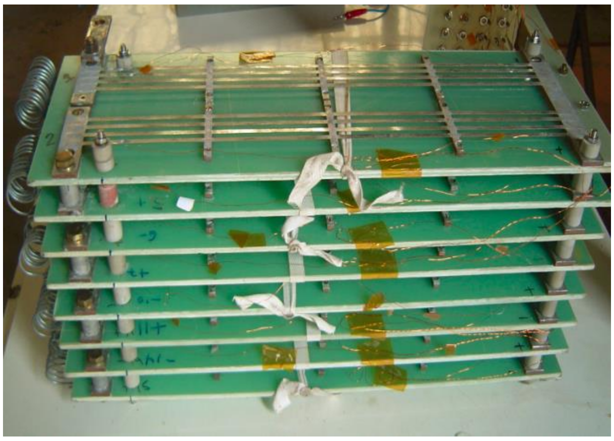

Figure 6.4 SFCL prototype

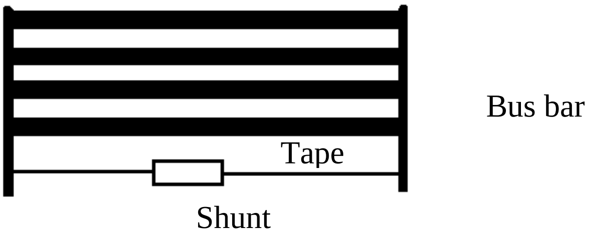

Figure 6.5 Schematic diagram of each element of the SFCL prototype

Table 6.1 Parameters of the AMSC 344S tape [80]

Substrate	Ni-5at%W (75μm)
HTS	YBCO (1μm)
Protective	Ag (4μm)
Solder	Mixture (Sn, Pb, Ag) (3+3μm)
Stabiliser	Stainless steel 316L (SUS 316L) (25+25μm)

(b) Introduction of fault experiments

To test the current limiting performance of the SFCL prototype discussed in Figure 6.4, fault current tests were carried out using the experimental system shown in Figure 6.6. The experimental system consists of a 3 MVA/15 kV/380 V transformer, a main switch, the SFCL prototype, variable resistors R1 and R2 and a switch for short circuits, as shown in Figure 6.6 [120]. The SFCL was tested under the voltage between phase and ground of the transformer, which was 220 V/60 Hz. During the fault current test, R1 and R2 could be adjusted to obtain suitable pre-fault currents and prospective fault currents, which varies from 0 kA to 10 kA. During the experiments, a steady current of 300 A flowed in the circuit before the occurrence of a short circuit and the fault lasted for five cycles [120].

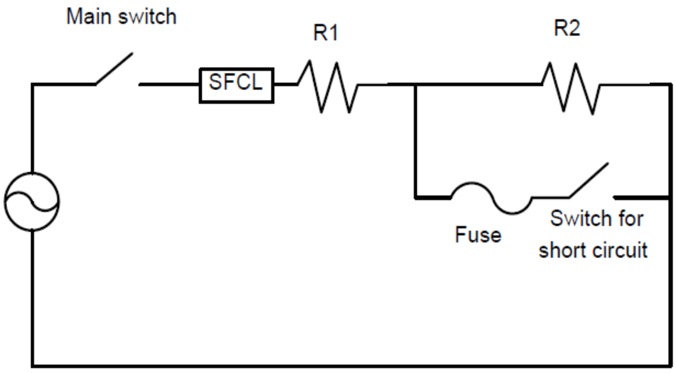

Figure 6.6 Experimental system

In the fault experiment, the current limiting performance of the SFCL prototype was tested under different prospective fault currents from 0.8 kA to 7.4 kA. The test results are summarised in Table 6.2.

Table 6.2 Summary of applied fault currents

Prospective fault current/kA_{rms}	Limited current/A_{rms}	SFCL voltage/V_{rms}	Voltage per element /V_{rms}
0.8	357.8	87	4.9
1.0	390.3	113	5.9
2.0	437.0	153	8.0
3.4	448.3	176	9.9
4.2	475.9	187	10.5
5.7	475.9	194	11.0
6.2	489.3	201	11.3
7.0	492.1	203	11.5
7.4	491.4	202	11.4

(c) Introduction of the simulation model

To simulate the SFCL prototype, a 2-D finite element model was built in COMSOL, where the cross-section of the four superconductor tapes were used to express the superconductor tapes of each element of the SFCL prototype, as shown in Figure 6.7. Considering that the shunt in each element of the SFCL prototype was difficult to simulate in the 2-D superconductor model, it was simulated in the experimental circuit model. For the simulation of the 344S tape, the real superconductor tape structure and geometry were used, as shown in Figure 6.8. Each tape is consisted of seven layers: two SUS 316L layers, two solder layers, a Ni-5at%W layer, a YBCO layer, and a silver layer, with the geometry of each tape shown in Table 6.3.

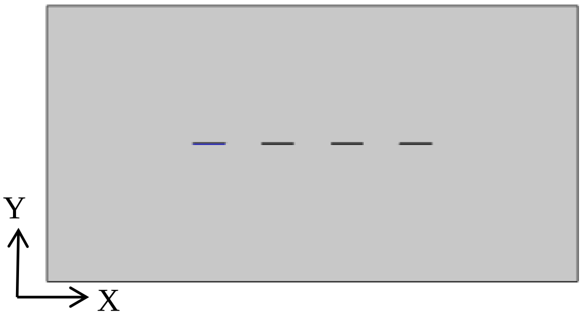

Figure 6.7 2-D model of four parallel 344S tape

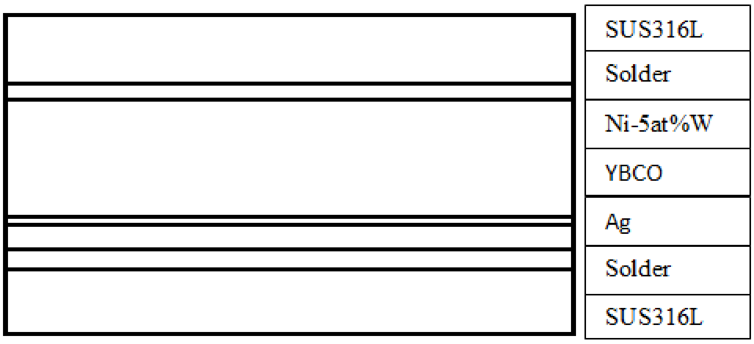

Figure 6.8 Schematic diagram of each 344S tape (not to scale)

The electrical and thermal parameters of the substrate, HTS, protective, solder and stabiliser used in the simulation are listed in Table 6.3 [121]. Further detailed temperature dependent variables are provided in the Appendix.

Table 6.3 Electrical and thermal parameters

layer	Density	Resistivity	Heat capacity	Thermal conductivity
	kg/m^3	Ω·m	J/(kg·K)	W/(m·K)
SUS316L	8000	Figure 0.1[122]	Figure 0.2 [123]	Figure 0.2 [124]
Solder	8410[125]	1.40e-7[125]	167[126]	50[125]
Ni-5at%W	10400[127]	2.68e-7[128]	440	Figure 0.3[129]
YBCO	5900	Eq.(5)	Figure 0.4 [130]	17[78]
Ag	10500	1.59e-8*(1+0.0038*(u3-293))[131]	235	Figure 0.5 [132, 133]

Note: due to the fact that the heat capacity and thermal conductivity of SUS 316L are not found, the corresponding parameters of SUS 316 are used instead.

To simulate the performance of the SFCL prototype during a fault, an experimental circuit model was built and combined with the superconductor model, as shown in Figure 6.9. The experimental system shown in Figure 6.6 was simulated with an electrical circuit built in the Electric Circuit interface of the AC/DC Module of COMSOL, as shown in Figure 6.9 (a). Two variable resistors R1 and R2 were used to simulate the line resistor and load resistor separately.

As shown in Figure 6.9 (b), the SFCL is expressed with a series connection of 16 elements in the electrical circuit. Each one is consisted of three resistors, which are the YBCO layers, metal layers (metal layers mean a combination of the Ni-5at%W layer, Ag layer, mixture layer and SUS 316L layer), and shunt.

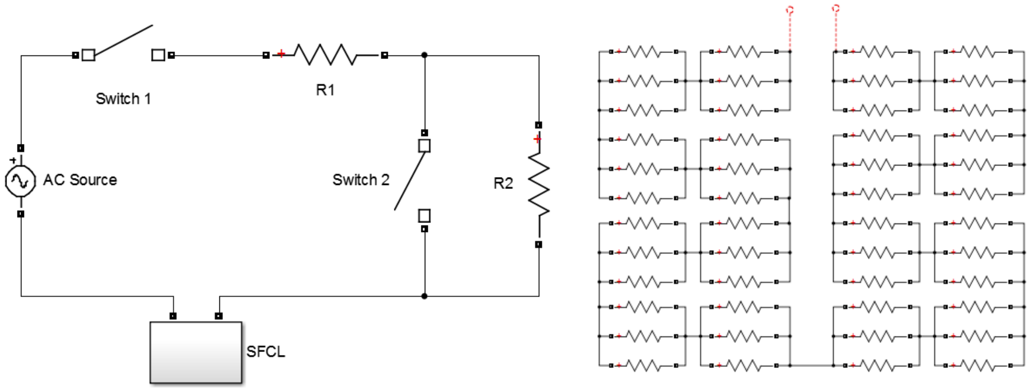

(a) (b)

Figure 6.9 Simulated electrical circuits: (a) the schematic diagram of the electrical circuit; (b) the schematic diagram of superconductor tape of the SFCL

The extraction of the current of the superconductor tapes from the experimental circuit model can be easily realised by summing up the current of the two resistors, which represent the YBCO layers and the metal layers in an element shown in Figure 6.9 (b). The extractions of the resistances of the YBCO layers and the resistance of the metal layers from the superconductor model are introduced below.

(1) Extraction of the resistance of metal layers

The resistance of the metal layers of a superconductor tape is regarded as the resistance of the six metal layers connected in parallel, which can be calculated with Equations 6.15 and 6.16. As shown in Equation 6.16, the resistivity of each metal layer is defined as a function of its average temperature.

$$R_{metal} = \frac{1}{\sum_{i=1}^{i=6} \frac{1}{R_i(\overline{T})}} \tag{6.15}$$

$$R_i(\overline{T}) = \rho_i(\overline{T}) \times \frac{l}{S} \tag{6.16}$$

(2) Extraction of resistance of the YBCO layers

The resistance of the YBCO layers is calculated based on the assumption that the YBCO layers and the metal layers are connected in parallel, meaning that the voltage drop on the two elements are the same. Therefore, the resistance of YBCO can be calculated by Equation 6.17.

$$R_{ybco} = \begin{cases} \min(\frac{R_{metal} \times I_{metal}}{I_{ybco}}, 29.544(\Omega)), T_{ybco} < T_c \\ 29.544(\Omega) \qquad\qquad\qquad\qquad , T_{ybco} > T_c \end{cases} \tag{6.17}$$

where 29.544 is the normal resistance of the YBCO layers at room temperature. If the temperature of YBCO is higher than the critical temperature, the superconductor completely loses its superconductivity and thus the resistivity of YBCO increases to the normal resistivity. Although the normal resistivity of YBCO is temperature dependent, it is taken as a constant (130e-8 Ω·m) here due to that the resistance of YBCO of each element is far larger than that of the metal layers and shunt resistor after quench. When the temperature of YBCO is lower than the critical temperature, the resistance of YBCO depends on the current density, temperature and magnetic field, with a maximum value of 29.544 Ω.

(d) Comparison of experimental and simulation results

In this work, different prospective fault current tests were simulated using the developed model. The details of the fault experiment with a prospective current of 7.4 kA, which contains the current limiting characteristics of the SFCL prototype, the temperature trend and the current distribution, are provided here. Then, to further validate the model, simulation results of the SFCL at different prospective fault currents are summarised and compared with the experimental results.

1) Simulation of the fault current test with prospective fault current 7.4 kA

As shown in Figure 6.10 and Figure 6.11, the simulated SFCL current and SFCL voltage with a prospective fault current of 7.4 kA are presented separately, which are compared with those in the experiments. The two simulated currents are mostly consistent with the experiment. However, in the first half cycle of SFCL current, the simulated peak current is a bit smaller than that in experiment, which also occurs in the simulation of other fault current tests. This might be because of the cooling effect of the copper bus bar and the intermediate copper bars were not considered in the simulation. The cooling effect of the copper bars can limit the temperature increase of the superconducting layers to some extent, which again limits the increase of the SFCL resistance, thus resulting in a higher current peak. Figure 6.11 shows that the simulated SFCL voltage agrees quite well with the experimental SFCL voltage.

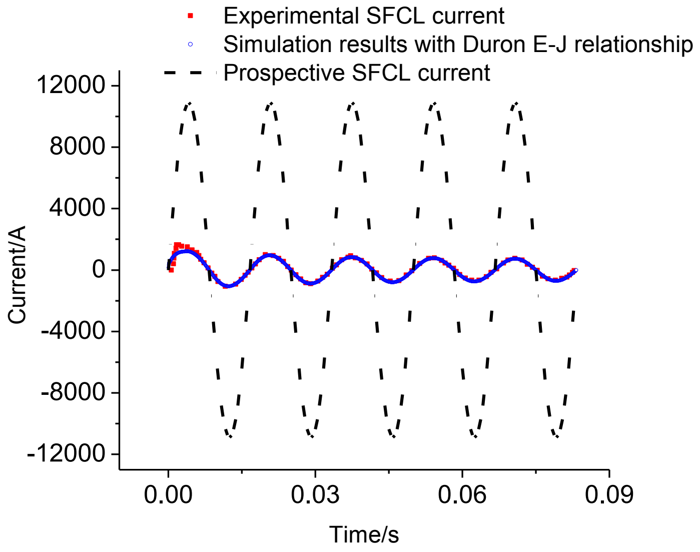

(a)

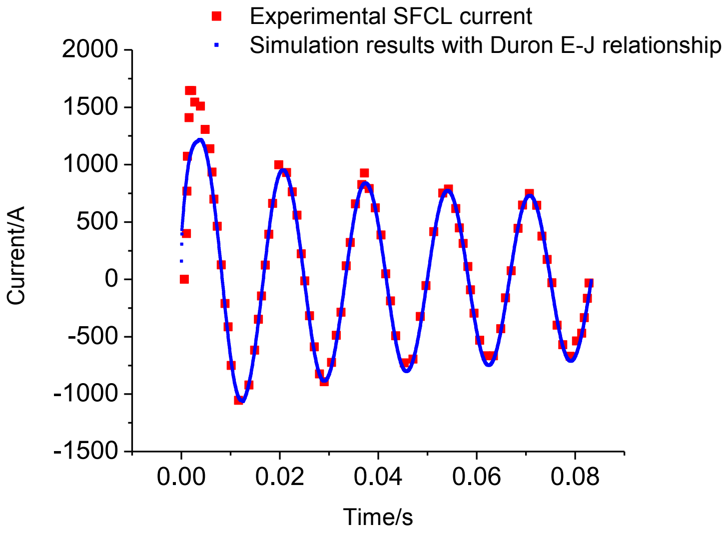

(b)

Figure 6.10 Comparison between experimental and simulated SFCL current

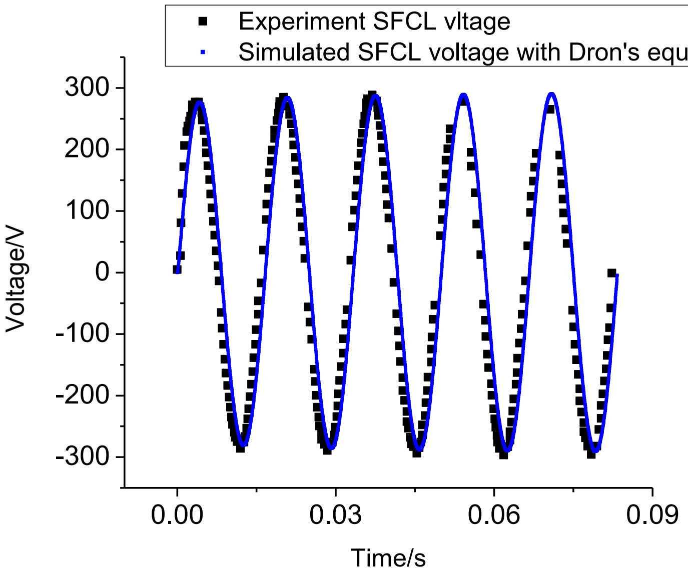

Figure 6.11 Comparison of experimental and simulated SFCL voltage

As shown in Figure 6.12, the average temperature of the superconductor tapes increases with fluctuations in the test. This is mainly because the power supply is AC, which means the heat dissipated in the superconductor tape is proportional to the current squared (I^2 - if the resistance of superconductor tape is regarded as a constant). Therefore, when the current is crossing zero, the heat generated in the superconductor is little, which leads to a small temperature increase of the superconductor. Moreover, when the current is at its peak value, whether it is positive or negative, the heat generated is very high, leading to a rapid temperature increase.

The resistances of the SFCL both in the simulation and in the experiment are also compared, as shown in Figure 6.13. It clearly shows that the trends of both SFCL resistances are almost the same. Due to the fact that the temperature increases with fluctuation (see Figure 6.12) and that the resistivity of Ag, SUS 316L and YBCO increase with the temperature, the resistance of the SFCL also increases with fluctuations after quench.

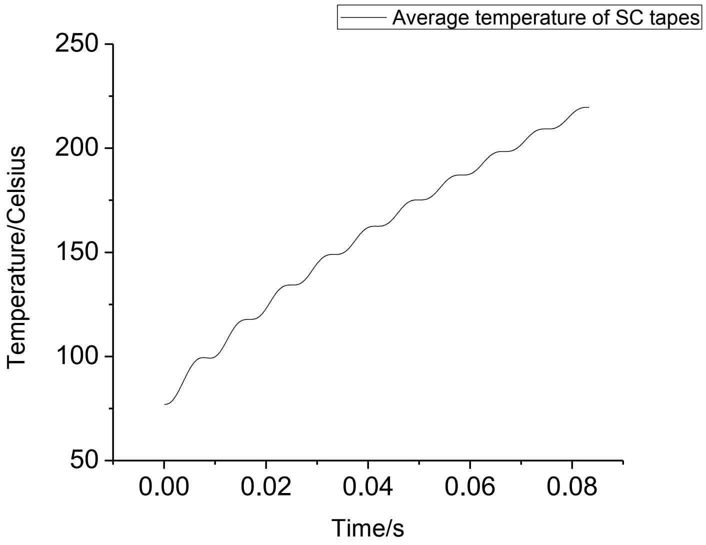

Figure 6.12 Trend of average temperature during quench

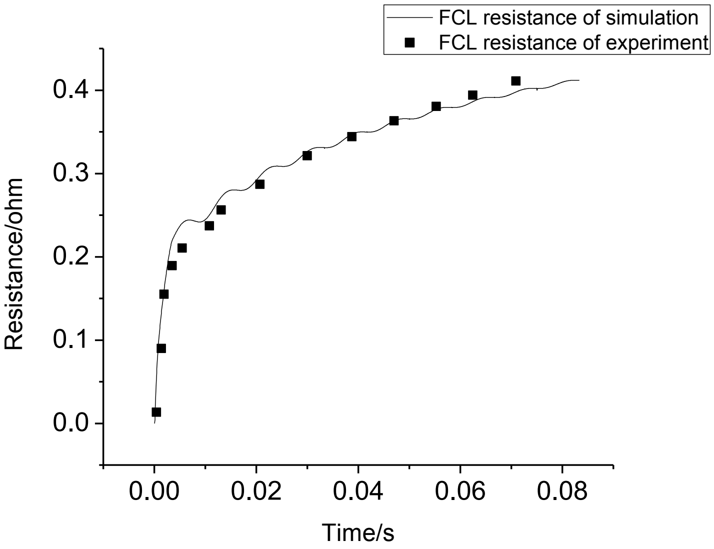

Figure 6.13 Comparison between experimental and simulated SFCL resistance

Also, the current distribution in different layers of the superconducting tapes is provided in Figure 6.14. It is clearly shown that the current mainly flows through the YBCO before quench and shunts to the metal layer and shunts with a resistance of 180 mΩ after quench. Furthermore, due to the fact that the metal layers resistance is far smaller than that of the shunt, the current in the metal layers is higher than that in the 180 mΩ shunt.

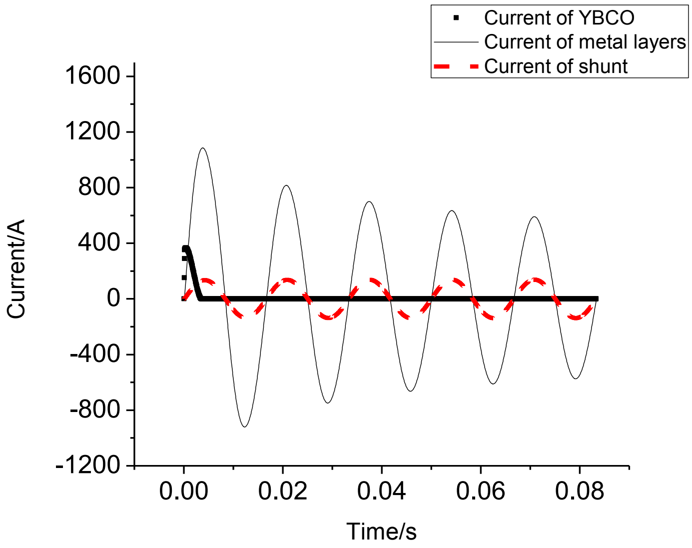

Figure 6.14 Distribution of current in different layers

2) Comparison of general trend of fault current tests

To further validate the simulation, the current limiting performance of the SFCL during different fault tests were simulated and compared with the experimental results shown in Table 6.2.

As shown in Figure 6.15, the limited SFCL currents during simulation under different prospective fault currents were compared with that of the experiments. The maximum calculation error was only 4.4% of the experimental results, which is very small when it is compared with the prospective current. The current limiting ratio, which is defined as the ratio of the prospective current to the limited current, was calculated and is summarised in Figure 6.16. It is clearly shown that the simulated current limiting ratios are almost the same as those in the experiment.

The SFCL voltages corresponding to the limited SFCL current in the experiment and in the simulation are also compared in Figure 6.17, which suggests that the simulated SFCL voltage is almost the same as that in the experiment. All these results show that the model performs well in simulating the performance of the SFCL prototype.

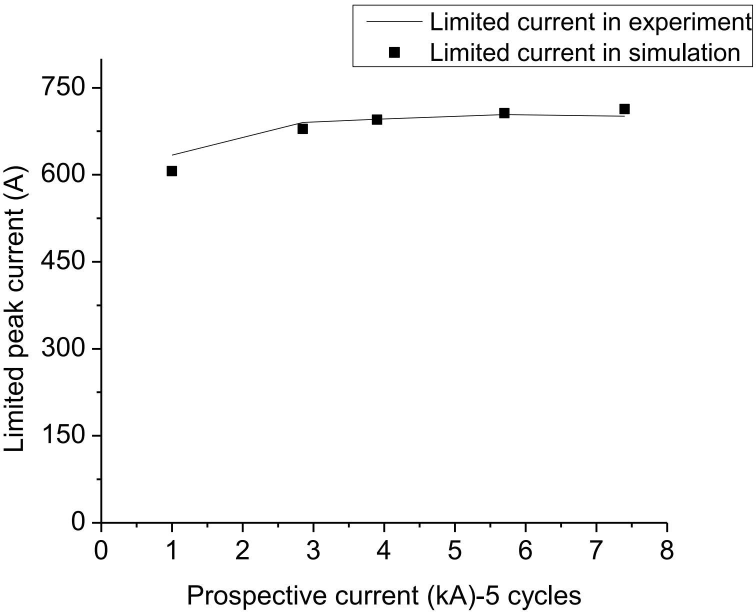

Figure 6.15 Comparison of limited peak current in the experiment and in the simulation

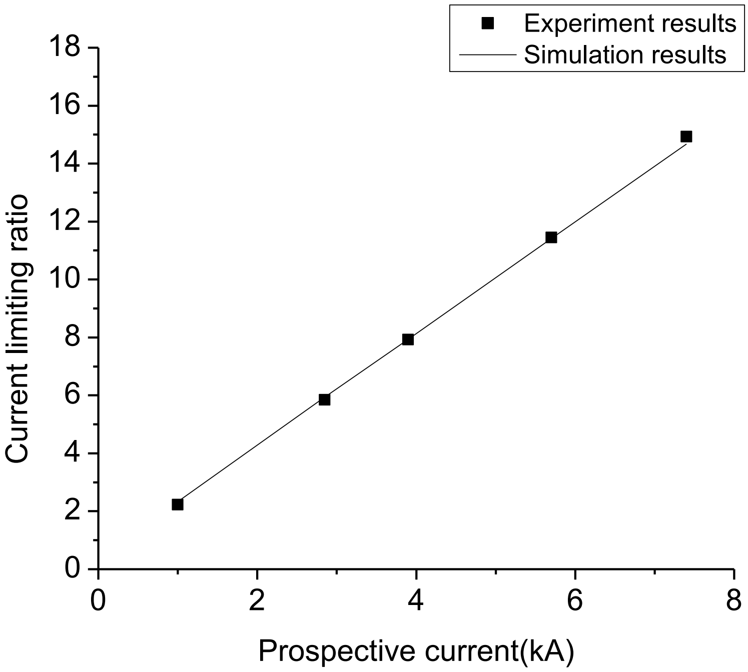

Figure 6.16 Comparison of the current limiting ratio in the experiment and in the simulation

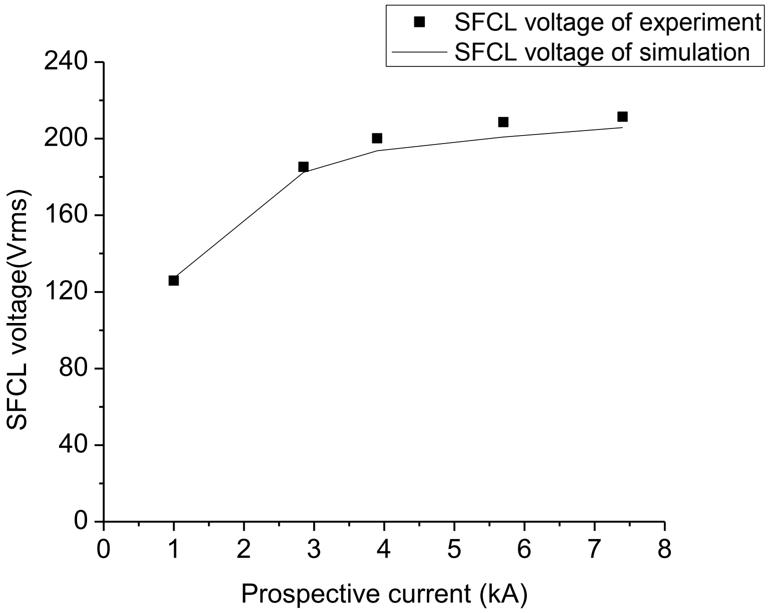

Figure 6.17 Comparison of the SFCL voltages in the experiment and in the simulation

(e) Discussion concerning the simulation model

In the simulation, it was found that convergence problem was a main challenge for the calculation, especially when the temperature of the superconductor approached 92 K (critical temperature of the superconductor). The convergence problem can be attributed to the extreme non-linearity of the *E-J* curve. To overcome this problem, it was necessary to decrease the slope of the *E-J* curve of the superconductor when the current density of the superconductor is higher than the critical current density whilst keeping the basic characteristics of the superconductor: negligible electrical field when the current is smaller than the critical current density. The decrease of the slope of *E-J* curve when $J > J_c$ can effectively limit the resistivity change of a local superconductor resulting from the temperature vibration, thus enhance the convergence. Therefore, in this chapter, a new *E-J* curve with a smaller slope was introduced.

Another method that can enhance the convergence of the calculation is that the temperature rise rate of each element should be decreased during the calculation. This can be realised by increasing the mesh density of the superconductor tape, especially in the thickness direction. This is because, according to the simulations, the temperature gradient in the thickness direction is far larger than that in the width direction.

Furthermore, calculation speed is another problem in the calculation of the proposed model. Generally speaking, it usually takes about 40-70 hours to calculate five cycles with a computer with an Intel Core i5 3.4 GHz processor and 8 GB of memory. Therefore, the calculations are quite time-consuming. This is mainly because of the fact that the real geometry of the superconductor tape is used, which leads to large number of mesh element and cumbersome calculation.

6.4 Conclusions

To simulate the macroscopic characteristics of the SFCL prototype, a finite element model coupling a superconductor model and an experimental circuit model is proposed in this chapter. To validate the proposed model, a 220 V resistive SFCL prototype that was built and tested under different fault currents are simulated with the model and the experimental and simulated results are compared accordingly.

The simulation realises the real-time data exchange between the coupled models during calculations, thus leading to precise calculation results. The simulated results of different fault current tests were compared with those in the experiments, which showed that the proposed model performs well in simulating the current limiting performance of the SFCL prototype. However, due to the fact that the real geometry of the superconductor tapes was used, the calculation was time-consuming, taking about 40-70 hours. The increase of the calculation speed is an important task for future research. This might be realised by using the symmetry boundary conditions, considering the symmetrical distribution of the simulated superconductors.

Furthermore, the model proposed can also be extended to simulate the performance of SFCLs in real power grids, considering that the simulated experimental circuit can be regarded as a simple power grid.

Chapter 7 Impact of different factors on the quench process of a resistive type superconducting fault current limiter

7.1 Experimental study of I_c inhomogeneity on the quench process

The hot spot problem is one of the main challenges for SFCL applications. It is mainly caused by the critical current inhomogeneity, which can be attributed to the limitation of the manufacturing technology and the non-uniform distribution of the self-field critical current density of a superconductor. It is very difficult to produce 2G HTS tape with homogeneous critical current density distribution [134].

Previous research shows that in the operation of SFCLs, the I_c inhomogeneity may lead to the excursion of maximum temperature for a high impedance fault [18, 19], which is detrimental to the operation of a fault current limiter. Therefore, the influence of critical current inhomogeneity of the 2G HTS tape during the quench process is studied with experiment.

To study the quench homogeneity of the superconductor, different I_c distribution along superconducting tape should be realised. However, for short samples (<1 m) the critical current density is generally homogeneous, which makes it difficult to study the impact of I_c inhomogeneity experimentally. Therefore, an artificial defect is made by using a permanent-magnet to create a local $\mathrm{I_c}$ degradation based on the magnetic field dependence of $\mathrm{I_c}$.

7.1.1 Experiment setup

In the experiments, samples made of 2G HTS tape from SuperPower were used, with minimum critical current of 83 A at 77 K, a width of 4 mm, thickness of 0.054 mm and length of 15 cm. The tape consists of a Hastelloy substrate, buffer stack, YBCO layer and silver layer, with a thickness of 0.05 mm, 0.2 µm, 1 µm and 3.6 µm respectively. There is no copper stabiliser in this tape.

Different fault currents were provided to the experiment sample to study the quench homogeneity in different fault cases. In the experiment, the current in the superconducting tape was measured with a Rogowski coil and the voltage distribution in the tape was measured with four voltage taps. Three of voltage taps are distributed in equal intervals along the sample and one voltage tap distribute with a variable tape distance, as shown in Figure 7.1(a) and (b).

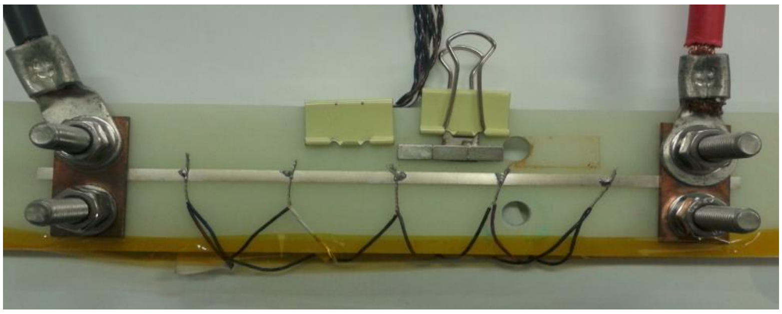

(a)

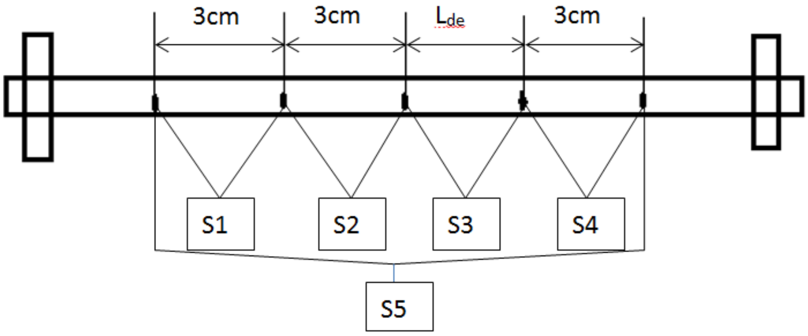

(b)

Figure 7.1 Experimental sample: (a) Picture of the actual HTS sample, (b) Schematic of the sample

Note: S1, S2, S3, S4 means segment 1, segment 2, segment 3 and segment 4 respectively and S5 means the sum of the four segments. In the experiment, the lengths of S1, S2, S4 are all 3 cm and the length of S3 (Lde) is set to be 1.5 cm or 3 cm to change I_c degraded segment length.

To control the critical current at S3, a N42 neodymium permanent-magnets (PM) was placed near the S3 to produce an external magnetic field, as is shown in Figure 7.1 (a). The dimensions of the PM used were 10 × 5 × 2 mm^3.

In order to verify the effect of the PM, experiments were conducted to measure the relationship between I_c variation of the tape and the positioning of the PM. The critical current of the sample without the influence of the PM was measured to be 93 A. Figure 7.2 demonstrates that by adjusting the direction and distance of the PM to the HTS tape, the critical current at 77 K at S3 can be controlled.

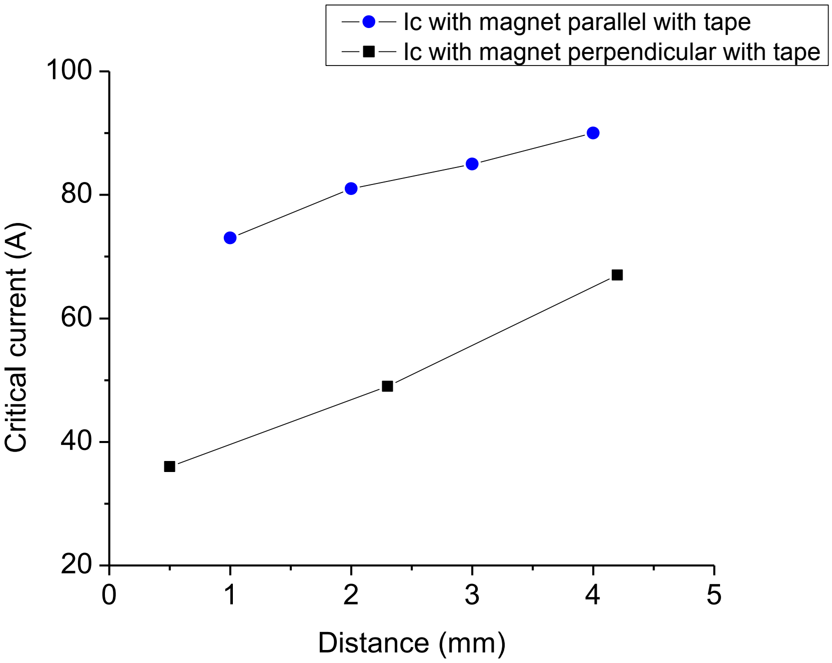

Figure 7.2 The relationship between critical current of the experiment sample and the placement of PM

Note: the curve with blue circles corresponds to the case where the PM is placed on the side of the tape, as shown in Figure 7.1(a) and the curve with black squares corresponds to the case where the PM is placed on top of the tape.

To provide different fault currents for the experimental sample, the experimental setup shown in Figure 3.3 was used. Considering that it is more difficult to change the line resistor to get different prospective fault currents, the method of varying the source voltage with an autotransformer whilst keeping the line resistor constant was implemented. The fault duration was set to be 0.1 s in the experiment, which was achieved by remotely controlling the on/off state of the circuit breaker. The line resistor R_1 and the load resistor R_L were 0.011 Ω and 1 Ω respectively.

7.1.2 Experimental results and analysis

(1) The impact of local I_c degradation on the quench process of the superconducting tape

To clearly indicate the impact of localized I_c degradation on the quench process of the HTS tape for different fault cases, a typical set of experimental results of a sample with 10% I_c degradation are provided. Segment S3 of length 1.5 cm was used for creating the localized I_c degradation. An electric field criterion of 1 µV/cm was used for establishing the I_c values.

The I_c distribution of the sample was measured before the fault experiment and the corresponding I_c values of different segments are shown in Table 7.1.

Table 7.1 Ic distribution among different segments of the experimental sample

Segment	S1	S2	S3	S4	S5
I_c/A	88.14	89	75.63	87.02	84.27
Length/cm	3	3	1.5	3	10.5

Note: S1 S2 S3 S4 and S5 correspond to different segments, as shown in Figure 7.1 (b).

When the source voltage was set to be 0.5 V, the current of the sample was observed to be 43 A_{rms} in all the five fault cycles. The voltage in the experiment sample was too small to measure, as shown in Figure 7.3, which indicates that there was no quench in the experiment sample. This is mainly because the magnitude of the current applied was smaller than the critical current of all the segments. Therefore, the superconductor tape did not quench in this process and still operated in the superconducting state.

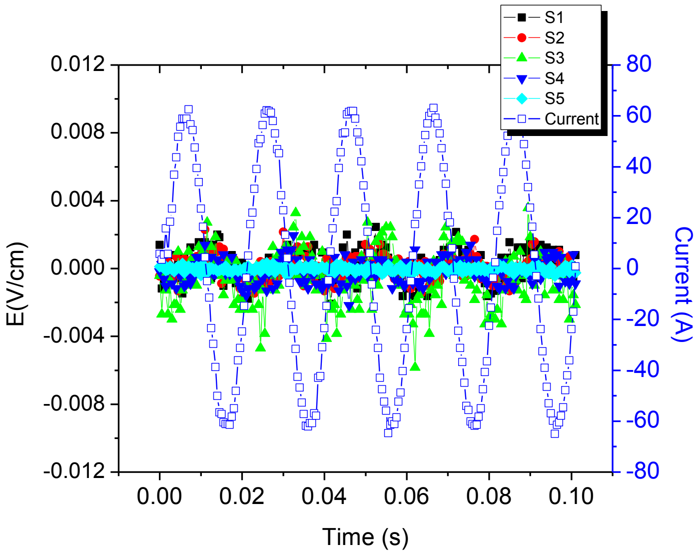

Figure 7.3 Current and electric field distribution of the experiment sample when the source voltage equals 0.5 V/m.

Note: In Figure 7.3-7.6, the phase of the current is reversed in order to make the figure easy to read.

When the source voltage was set to be 1 V, there was an obvious current decrease in the fourth and fifth fault cycles, as shown in Figure 7.4, which indicated the current limiting effect of the experiment sample. In this case, complete quench occured in S3 only, demonstrated by the green curve. The resistance of S3 limits the fault current from 88.4 A to 50.2 A during the fault period, with a limiting current ratio (I_{lim}/I_{prosp}) of 0.57.

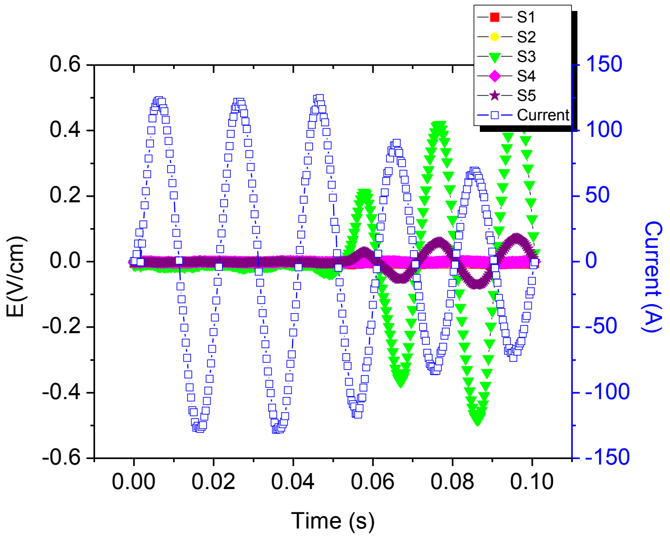

Figure 7.4 Current and electric field distribution of the experiment sample when the source voltage equals 1 V

The results in Figure 7.4 show that for the case of low fault currents, the quench tends to occur firstly in the segment with the lowest I_c. This is because the applied current reaches the degraded I_c value first in the fault period, which generates an electric field in this local area. Thus, the resulting heat generated in the S3 leads to a rise in temperature, which again quenches the local superconductor.

When the voltage is further increased to 1.4 V, the fault current is limited from the first cycle, which decreases from 114 A in the first half cycle to 32.6 A in the final cycle, as shown in Figure 7.5. In this case, three segments (S1 S3 and S4) quench, which shows that the fault current increase results in the quench of more segments. This can be easily understood with the heat generation in these segments, which are high enough to increase the temperature above the critical temperature.

An interesting finding in this experiment case is that after quench, the electric field in S4 decreases slowly and the electric field in S3 has a trend of increase during the current limiting process. This phenomenon is mainly because the heat generated in S4 is not sufficient to maintain its high temperature, thus leading to the decrease of its temperature and the recovery of its superconducting property. Furthermore, the heat generation in S3 is still high enough to increase its temperature, thus leading to the increase of its voltage. Furthermore, the convective cooling coefficient might be another factor for this phenomenon. For S4, the temperature increase might be higher than that of S3, which means more heat is transferred to the liquid nitrogen during the fault. Therefore, more heat generation is needed to keep the high temperature for S4.

When the source voltage equals 5 V, the quench process of all the segments are almost the same, as shown in Figure 7.6. This indicates that with a high voltage, the I_c degradation in S3 has almost no influence on the quench process of the superconductor. This is mainly because the fault current is increased to 195 A in 3 ms, leading to the appearance of a high electric field in every segment according to the E-J relationship of the HTS superconductor in the over-current range [135]. This leads to simultaneous heat generation in every segment and a sharp increase of superconductor resistivity.

As clearly shown in the experimental results, the quench modes for different fault voltage levels are quite different. When the superconductor is operated under low voltage, the prospective fault current is lower than the I_c of the sample, no quench occurs in the superconductor. When operated under high voltage, the fault current is far higher than the I_c of all segments, all segments quenched simultaneously and the electric field was distributed evenly all along the sample. For both cases, the impact of local I_c degradation was negligible and the superconductor was very safe, which was because the temperature increase in the superconductor was even and was in control.

However, for faults where the voltage is between the two extreme levels, the influence of I_c degradation in local segments is quite dominant in determining which segments to quench and at what time to quench. The problem that this pose is that the local quench will lead to an increase of local temperature, which may exceed the maximum temperature that the superconductor can withstand [18, 19]. Therefore, in the following sub-section, the influence of I_c inhomogeneity on the maximum temperature of the superconductor will be analysed further.

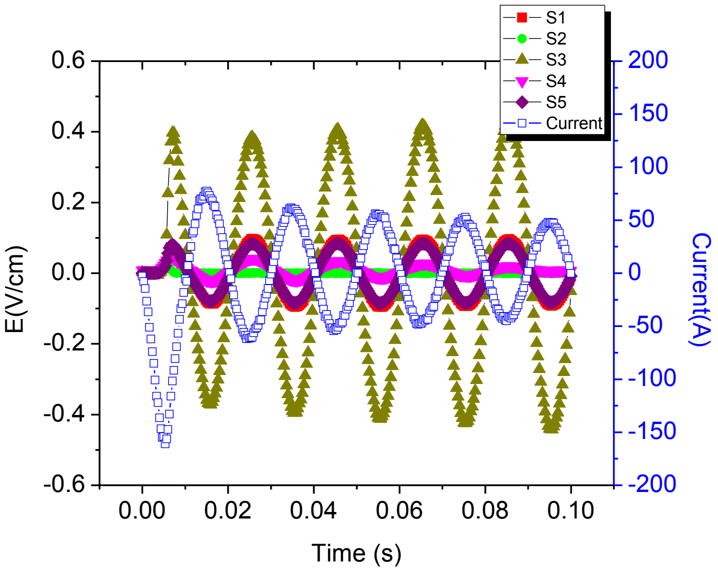

Figure 7.5 Current and electric field distribution of the experiment sample when the source voltage equals 1.4 V

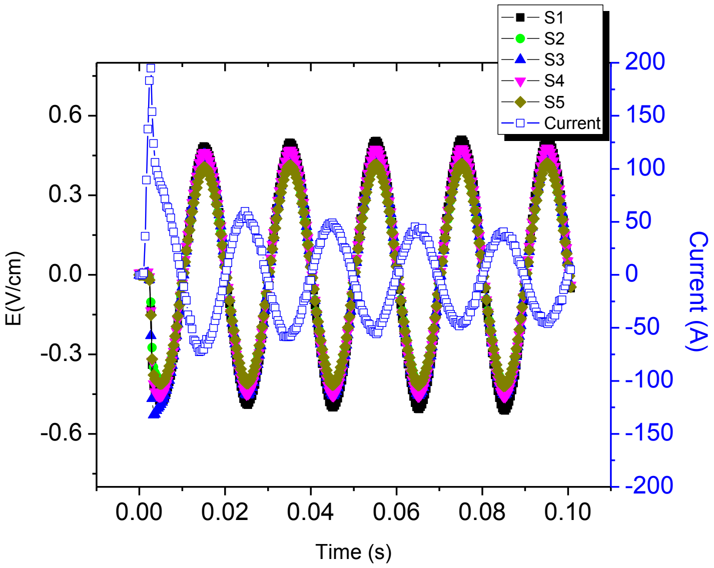

Figure 7.6 Current and electric field distribution of the experiment sample when the source voltage equals 5 V

(2) The impact of I_c inhomogeneity on the maximum segment temperature generated

In the operation of the SFCLs, the superconductor tape might be damaged or even burned if the local temperature generated exceeds the maximum temperature it can withstand. Usually a maximum temperature of 300 K is set to guarantee safe operation of the HTS tapes [19].

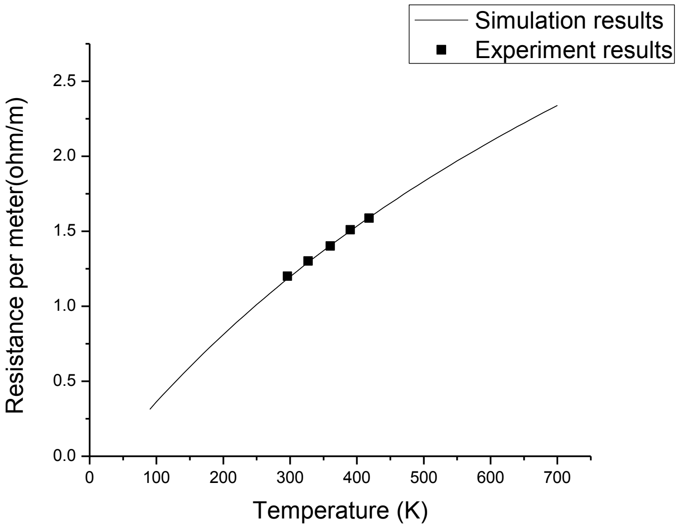

Figure 7.7 Relationship between sample resistance and temperature

As the experiment duration was only 0.1 s, it was difficult to measure the temperature of the superconductor directly. Therefore, the temperature of the superconductor was derived from a simulated resistivity-temperature curve, as shown in Figure 7.7. The simulated curve is based on the assumption that the temperature of the superconductor is constant in the thickness direction and that the tape is taken as a combination of an YBCO layer, substrate layer and the silver layer connected in parallel. Thus the resistivity-temperature curve of the tape was derived from the resistivity-temperature relationship of each separate layer directly. In order to verify the simulated curve, the resistivity of the superconductor tape between room temperature 296.15 K and 420 K is measured, as shown in Figure 7.7. It is worth noting that the temperature of each segment calculated with this method was basically the average temperature of each segment.

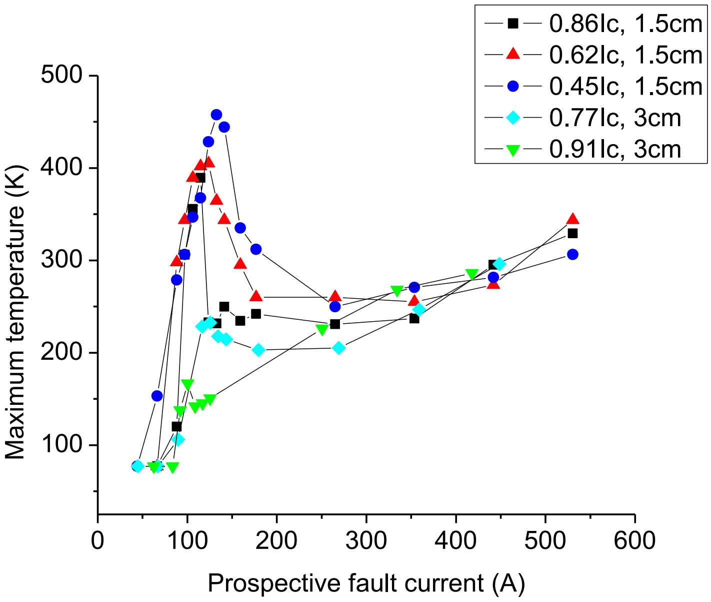

Figure 7.8 The relationship between prospective current and maximum temperature

Note: In the legend of Figure 7.8, the first expression means the fraction of remnant critical current value after applying the PM, and the second expression means the length of S3 along which the PM is applied.

To better evaluate the impact of I_c degradation and I_c degraded segment, samples with different I_c degradation and different I_c degraded segments were tested under different fault voltages. As shown in Figure 7.8, for a 0.1 s fault test with different samples, the increase in the maximum temperature are observed to be nonlinear and there was always a peak temperature appearing around 1.13 I_c to 1.51 I_c.

The experimental results show that when the peak temperature appears under low prospective fault current, only the PM degraded segment shows obvious quench. This shows that in these cases, only the PM degraded segment quenches and withstands all the voltage, leading to a fast temperature increase in S3. As shown in Figure 7.8, in some cases, the maximum temperature even reached more than 450 K, which greatly endangers the superconducting experimental sample.

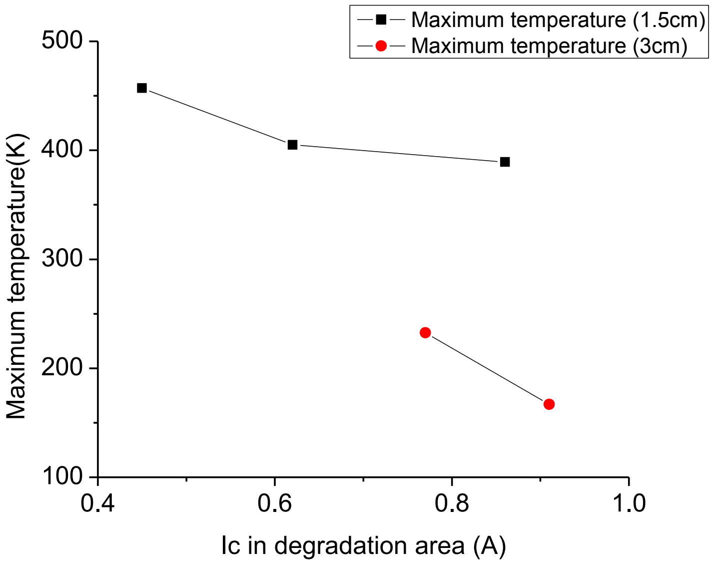

Figure 7.9 The relationship between I_c in the PM degraded segment and the maximum temperature in the degraded segment

The experimental results in Figure 7.9 show that with the decrease of I_c in S3, the maximum temperature increases gradually. To clearly illustrate this phenomenon, the power dissipated on the 1.5 cm PM degraded segment (S3) under different I_c degradation cases where the maximum temperature appears are compared in detail in Figure 7.10. According to Figure 7.10, there are two possible reasons for the maximum temperature increase. With a lower I_c, the PM degraded segment quenches earlier, which can be observed by comparing the power curve of the samples with 0.45 I_c and 0.62 I_c in local area with that of 0.86 I_c in the local area. The earlier quench of the PM degraded segment leads to a longer time for heat dissipation in the degraded segment. Furthermore, Figure 7.11 shows that with the decrease of I_c in S3, the voltage of S3 in fault period also increases. A Higher fault voltage leads to higher heat generation in the PM degraded segment if the resistance is taken as constant.

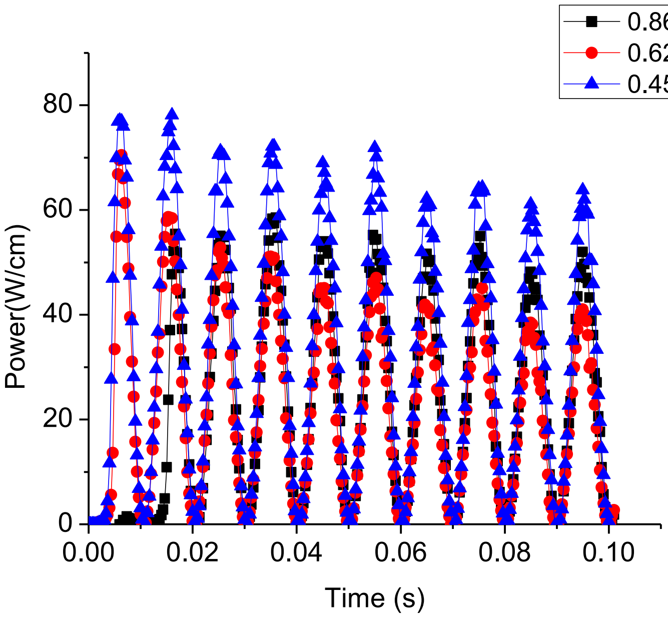

Figure 7.10 The trend of the power density when maximum temperature appears in different fault cases

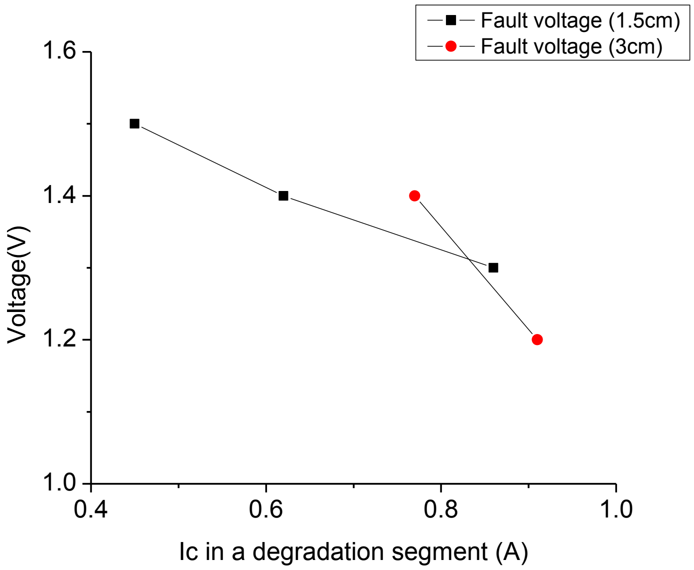

Figure 7.11 The relationship between I_c in the PM degraded segment and the fault voltage when the maximum temperature appears

Another phenomenon is that with the decrease of degraded segment size, the maximum temperature in the quench process increases, as shown in Figure 7.9. This is mainly because of the electric field of the shorter PM degraded segment being much higher than that on a longer PM degraded segment, which can be derived from

Figure 7.11. A higher electric field corresponds to more heat generation and a higher temperature.

Figure 7.11 clearly shows the lower the critical current of the PM degraded segment, the higher the fault voltage when maximum temperature appears. This is mainly because a lower critical current results in an earlier quench of S3 due to massive heat dissipation, which can be derived from the *E-J* power law. The early quench of S3 then results in the early limitation to fault current, which in turn delays the quench of other segments compared with the case of a higher critical current in the degraded segment S3, thus leading to the increase of the fault voltage when the maximum temperature appears.

7.2 Numerical study of the impact of stabiliser thickness on the current limiting process

For SFCLs, the stabiliser thickness is an important parameter to be determined in the design process, which not only determines the resistance of a superconductor, but also has a significant impact on the temperature rise in the fault period.

To study the impact of stabiliser thickness on the current limiting process of SFCLs, the electro-magneto-thermal model introduced in Chapter 6 was used again.

The current limiting process of a 0.4 m, AMSC 344s tape was simulated by changing the thickness of the stabiliser. The specific parameters of the tape are shown in Table 7.2. A 2-D cross section model was built for simulating the electro-magnetic and thermal process of the sample during the fault period, as shown in Figure 7.12.

In the calculation, the electro-magnetic model and thermal model were coupled together. The heat generated in the electro-magnetic-model was transferred to the thermal model and the temperature calculated in the thermal model was transferred back to the electro-magnetic model (see Section 6.1 for further details).

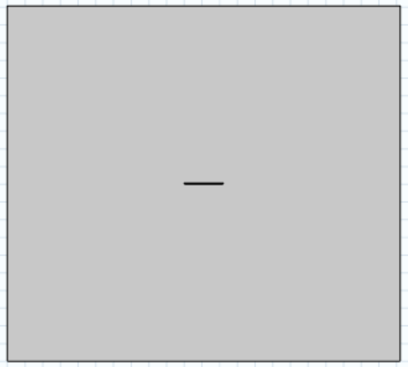

Figure 7.12 2-D cross-section model of the simulated SFCL

Furthermore, the circuit model used for providing fault current to the SFCL is shown in Figure 7.13. As shown in Figure 7.13, the fault current test circuit is composed of three components--AC source, the line resistor R1 and the superconductor equivalent model. In the superconductor model, the superconductor is approximated with a superconducting-layer resistor (Rsc) and a metal-layer resistor (Rmetal), which are connected in parallel.

To couple the electro-magneto-thermal model and the circuit model, the values of the resistors Rsc and Rmetal are transferred from the electro-magnetic model to the circuit model and the current in the superconducting layer and non-superconducting layers are then transferred back, as shown in Figure 6.3.

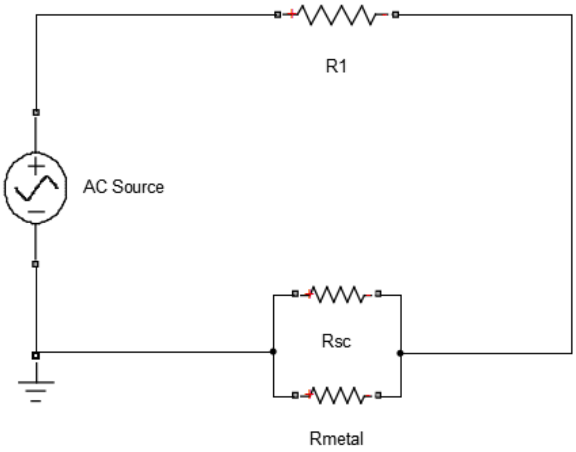

Figure 7.13 The schematic diagram of the electric circuit model

Table 7.2 Parameters of the AMSC 344s tape

Length [m]	0.4
Width [mm]	4.4
Critical current [A]	72
Ni-5at%W [µm]	75
YBCO[µm]	1
Ag [µm]	4
Solder Mixture (Sn, Pb, Ag) [µm]	6
Stainless steel 316L (SUS 316L)[µm]	variable

The AC voltage applied to the circuit during a fault period is $30 * \sin(2\pi f t)$, where f is 60 Hz. The fault lasts for five cycles. Furthermore, the line resistor R_1 is 0.004 Ω. The resistors Rmetal and Rsc are shown in Equations 6.15 and 6.17 respectively. In the experiment, three different cases are tested, with stabiliser thickness 50 µm, 100 µm, 150 µm respectively.

As shown in Figure 7.14, under the same fault voltage, the resistance of the superconductor increases slower with the increase of stabiliser thickness. This phenomenon seems to be contradictory to the fact that the heat generated in superconductor increases with the tape thickness, as shown in Figure 7.15.

However, this contradiction can be explained with the impact of stabiliser thickness on the heat capacity of the superconductor. With the increase of stabiliser thickness, the heat capacity of the superconductor will also increase. As shown in Figure 7.16, although the power generated in the superconductor increases with the stabiliser thickness, the temperature increase is slower, which shows that the gradual increase of specific heat.

Based on the comparison of limited fault current in Figure 7.17, it can be concluded that the increase of stabiliser thickness tends to decrease the current limiting ability of superconducting tape. Therefore, to limit the fault current to the same level, longer tapes are required if tape with a higher stabiliser thickness is used. The increase of tape length will increase the SFCL cost.

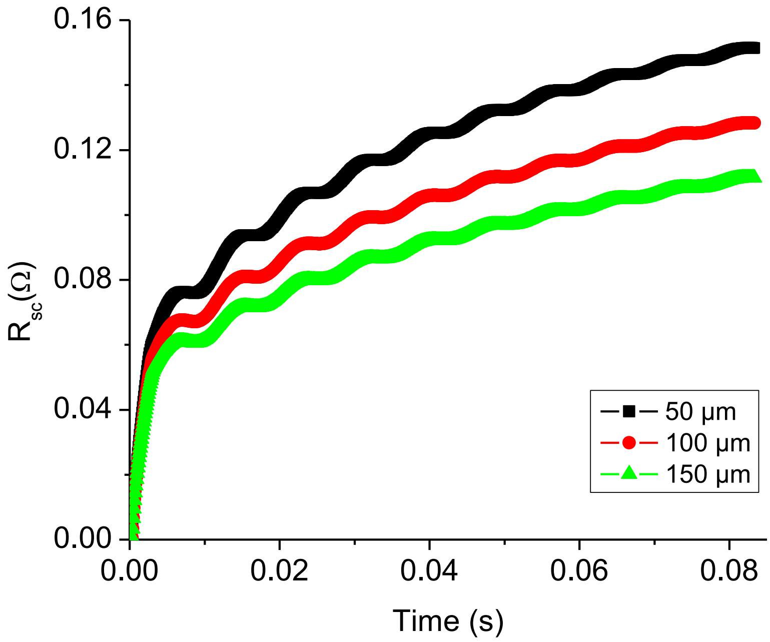

Figure 7.14 The trend of superconductor sample resistance during a quench period

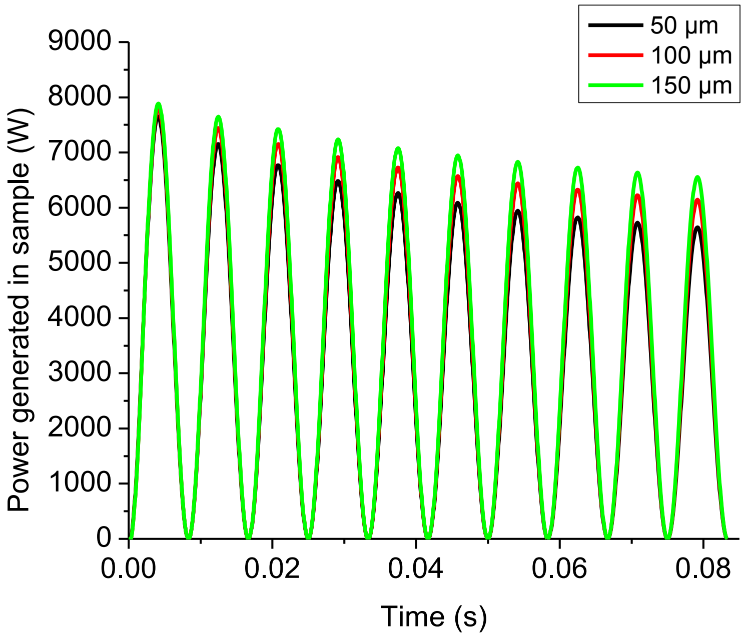

Figure 7.15 Comparison of the power generated in the superconducting samples with different stabiliser thicknesses

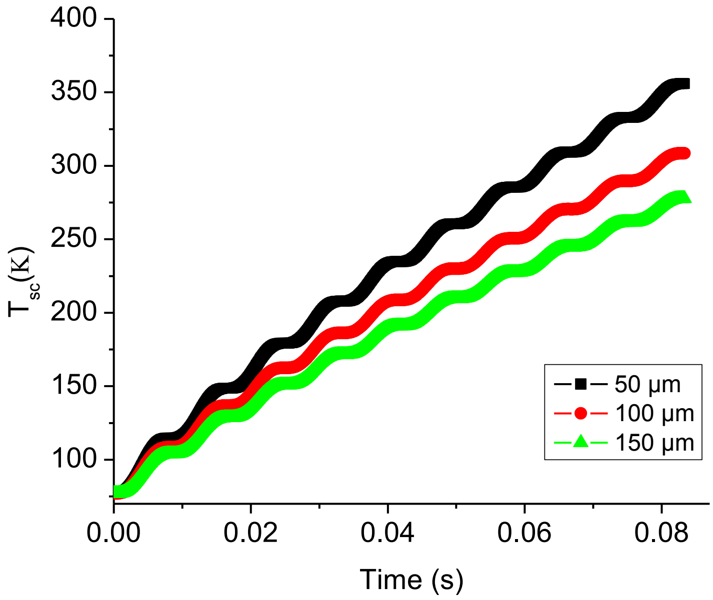

Figure 7.16 The trend of average temperature of the superconductor during a quench period

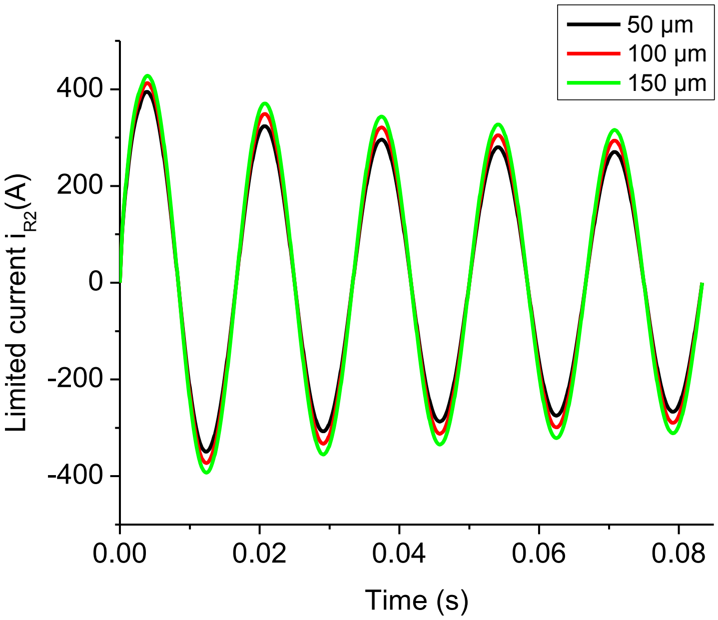

Figure 7.17 Comparison of limited current during a fault period

7.3 Impact of shunt resistor on the current limiting process of SFCLs

In SFCLs, a shunt resistor is usually used to adjust the limited fault current during a fault period and also to provide a current flow path in case of superconductor failure or removal of a SFCL element. Based on the model built in Section 7.2, the impact of the shunt resistor to the current limiting process is studied by adding a shunt resistor in parallel with the superconductor element. The new schematic diagram is shown in Figure 7.18.

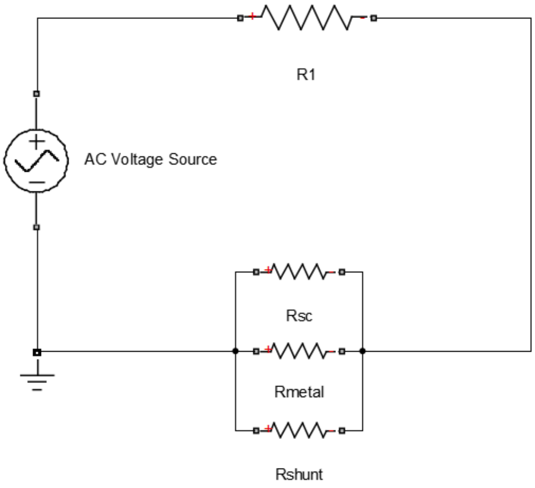

Figure 7.18 The schematic diagram of the electric circuit model

In the simulation, the shunt resistor is varied (0.02 Ω, 0.1 Ω, 0.5 Ω) to study its impact on the limited current and the quench of the superconductors. The load resistor is 0.004 Ω. The parameters of the AMSC tape are same with that used in Section 7.2, with a stabiliser thickness of 100 µm.

Firstly, the limited fault current in the circuit with different shunt resistors values are shown in Figure 7.19, which indicates that the increase of shunt resistance tends to decrease the limited fault current. This can be explained based on analysis concerning the total resistance in the circuit. After quench of the superconductor, the higher the shunt resistance, the higher the total resistance in the circuit. This therefore results in a lower current flowing through the circuit.

However, the increase of shunt resistance also increases the maximum resistance and the maximum temperature of the superconductor reached during a fault period, as shown in in Figure 7.20 and Figure 7.21 respectively. This is mainly because the lower fault current, which is generated by the higher shunt resistance, leads to more voltage drop across the superconductor (Figure 7.22), thus leading to more heat generated in the superconductors.

Based on these results, it can be derived that the decrease of shunt resistance decreases the current limiting ability of SFCLs. However, it also decreases the maximum temperature reached in the superconductors. Therefore, the shunt resistance can be a tool to adjust the limited fault current of SFCLs in power grids, as well as to control the maximum temperature in a quench period under temperature limit. Furthermore, considering a higher temperature reached in a superconductor will leads to a longer recovery time, the shunt can also be used to accelerate the recovery of the superconductor after quench.

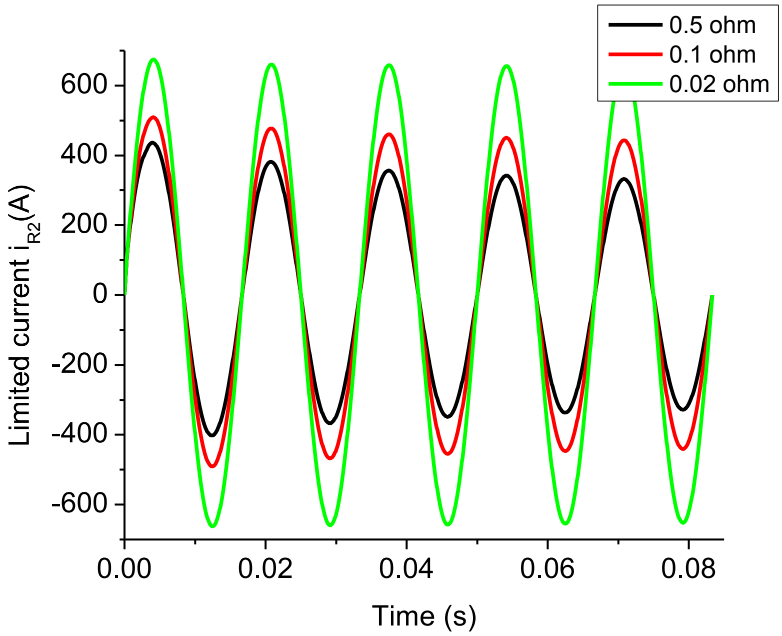

Figure 7.19 Limited fault current in fault cases with different shunt resistor (0.02 Ω, 0.1 Ω, 0.5 Ω)

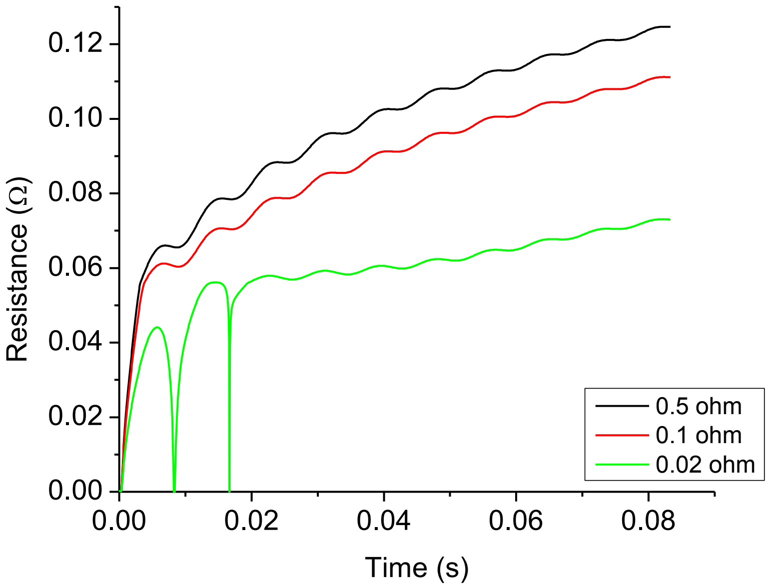

Figure 7.20 Resistance trend in fault cases with different shunt resistor (0.02, 0.1, 0.5 Ω)

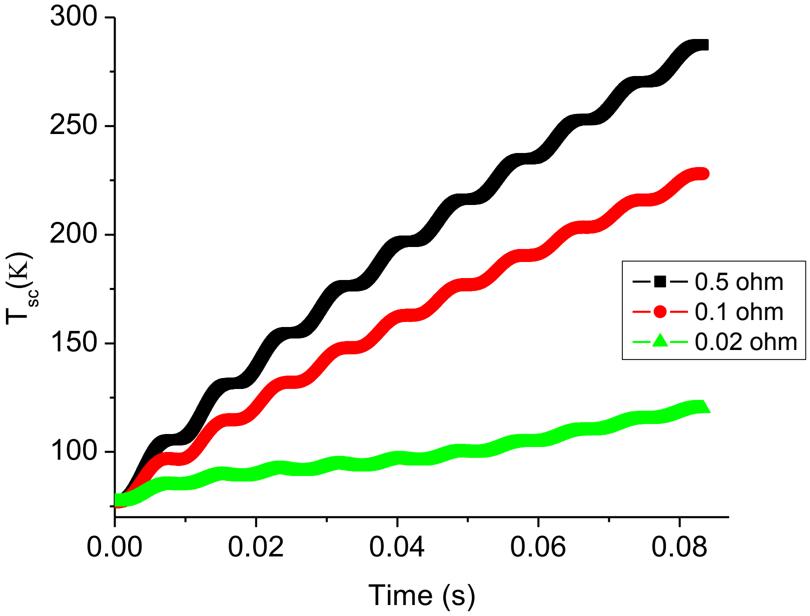

Figure 7.21 Average temperature of the superconductor in fault cases with different shunt resistor (0.02 Ω, 0.1 Ω, 0.5 Ω)

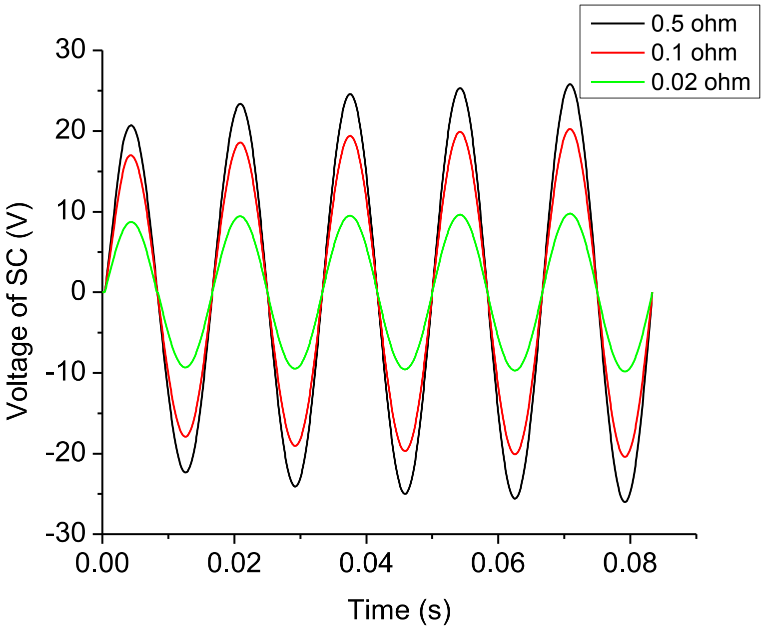

Figure 7.22 Voltage of the superconductor in fault cases with different shunt resistor (0.02 Ω, 0.1 Ω, 0.5 Ω)

7.4 Conclusions

In this chapter, the impact of different factors such as critical current inhomogeneity, stabiliser thickness and the shunt resistor on the quench period of SFCLs was studied. All these factors have a significant impact on the current limiting performance and the safe operation of SFCLs. Therefore, it is paramount to study their impact during the fault period.

For the critical current inhomogeneity impact, the quench processes of samples with different local I_c degradations were investigated, which showed that the deterioration of local I_c degradation will increase the maximum temperature in the degradation segment and the decrease in size of the I_c degraded segment will increase the maximum temperature reached in the I_c degraded segment.

Investigation concerning the stabiliser thickness impact shows that for the AMSC tape, although the increase of stabiliser thickness can undermine the current limiting property of SFLCs, it can also decreases the maximum temperature reached in the superconductor as well.

A study concerning the impact of shunt resistance indicates that the shunt resistors can be used to adjust the limited fault current, to control the maximum temperature reached in the superconductor and also to accelerate the recovery time of SFCLs after a quench period.

Chapter 8 Conclusions

8.1 Summary of conclusions

Due to the negligible impact to power grid and fast reaction in case of fault, SFCLs have been an attractive and promising devices for current limiting in power grids. The commercialisation of high-temperature superconductors, especially 2G HTS, has also provided an objective condition for the large-scale and widespread application of superconductivity technology. In this thesis, the comprehensive characteristics of non-inductive solenoidal coils based on 2G HTS for SFCLs were studied both numerically and experimentally. The main accomplishments of this thesis can be summarised as followings;

- Considering that there is still no systematic research work concerning the AC losses of non-inductive solenoidal type coils, an innovative method was proposed for simulating the AC losses of solenoidal type coils. Experimental works shows that the AC losses of a braid type coil is lower than that of the single tape by approximately an order of magnitude in the low current regions and the AC losses of the non-intersecting type coil was similar to that of a single tape. Further discussion revealed that the pitch and inter-layer separation are the two key parameters that determine the AC losses of non-inductive solenoidal coils.
- A comprehensive and in-depth comparison study was conducted concerning the application of the two types of non-inductive solenoidal coils in SFCLs. Experimental studies showed that the non-intersecting type coil performs well in current limiting property and recovery time, but has an insulation problem with the increase of voltage level. However, the braid type coil performs well in AC losses, current limiting property and insulation, which make it a much more suitable choice for high voltage SFCL use.
- A 220 V/300 A braid type SFCL prototype based on 2G HTS was designed, built and tested in this work. Deep analysis concerning design optimisation

showed that: (1) magnetic substrate orientation and the coil pitch have a serious impact on the AC losses of SFCLs; (2) coil diameter, pitch and coils structure have a significant influence on the volume of SFCLs; (3) the inductance of SFCLs is mainly determined by the pitch and tape separations.

- To simulate the current limiting properties of SFCLs, an electro-magneto-thermal model was proposed in this work, which could not only provide the microscopic characteristics of a superconductor during the quench period, but also simulate the performance of large-scale SFCLs in power grids. Furthermore, simulation work concerning a 220 V prototype validated the proposed model.
- Finally, the impact of different factors such as the critical current inhomogeneity, stabiliser thickness and shunt resistance on the quench process of SFCLs was studied. The studies showed that (1) the deterioration of local I_c degradation and the decrease in the size of the I_c degraded segment will increase the maximum temperature under low fault voltage; (2) for a SFCL made of the AMSC tape, a stabiliser thickness increase will decrease the maximum temperature reached in the superconductor; (3) the shunt resistors can be used for adjusting the maximum temperature and recovery time of the SFCL.

8.2 Future work

This work can be potentially improved in several aspects in the future.

Firstly, the simulation works concerning the AC losses of the 220 V/300 A SFCL prototype (described in Chapter 5) shows that the magnetic substrate has a significant impact to the AC losses of the braid type coil. Therefore, more detailed work can be conducted to compare the AC loss characteristics of braid type SFCLs with and without magnetic substrates, which will provide a more comprehensive guidance for practical applications of braid type SFCLs. Furthermore, the AC losses of the tape with double HTS layers produced by AMSC would also be interesting for further investigation and comparison.

Secondly, study in Chapter 5 shows that the coil parameters and structures might greatly increase the AC losses of the 220 V SFCL prototype. However, it is still not clear the key reason that leads to the AC losses increment. Therefore, further simulation work is needed in the future to figure out the reason. In addition, based on the study, more optimisation work can be proposed, which might include the minimum and maximum coil diameter, and optimal distance between adjacent coils.

In Chapter 7, the I_c inhomogeneity impact on the quench process is investigated experimentally, which provided a good reference for research concerning hot spot problems. However, for applying a practical SFCL in a power grid, the experimental work is not possible and realistic. Consequently, more numerical work including the longitudinal I_c distribution needs to be done to investigate the I_c inhomogeneity impact on the quench process of SFCLs.

Finally, to implement the SFCL in a power grid, simulation work concerning a SFCL in a power system need to be done. This can be realised by extending the simulation model proposed in Chapter 6 to practical devices. However, the disadvantage of the FEM model lies in the slow and time-consuming calculation. Furthermore, with 2D cross-section model, the $\mathrm{I_c}$ inhomogeneity cannot be taken into consideration. Therefore, to develop more fast and practical models, a lumped circuit model could be explored and developed.

Appendix

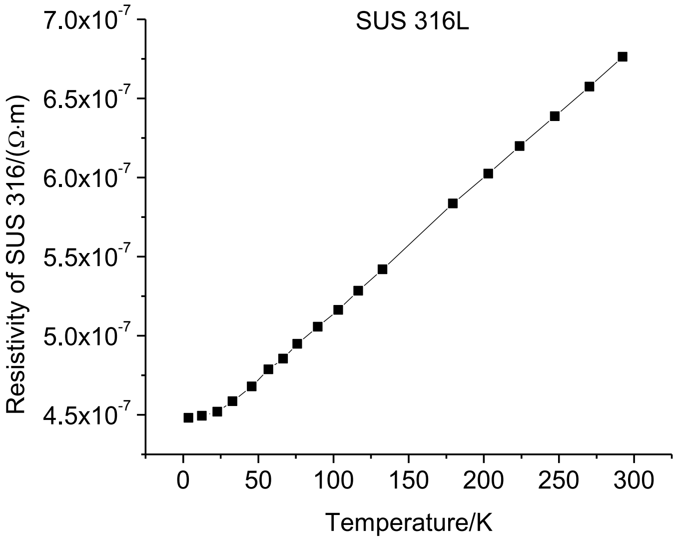

Figure 0.1 Resistivity of SUS 316L under different temperature [122]. The figure shows that with the increase of temperature, the resistivity of SUS 316 also increase gradually.

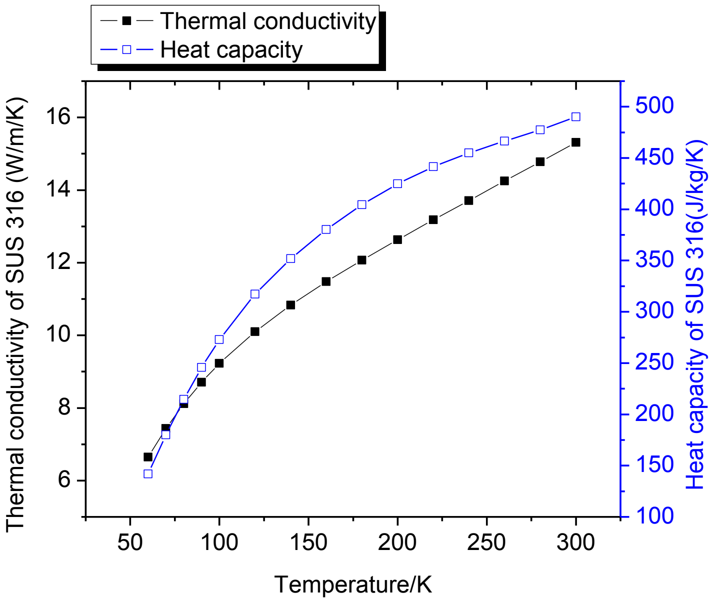

Figure 0.2 Thermal conductivity and heat capacity of SUS 316 under different temperatures [123, 124]. The figure shows that both the thermal conductivity and heat capacity of SUS 316 increase gradually with temperature

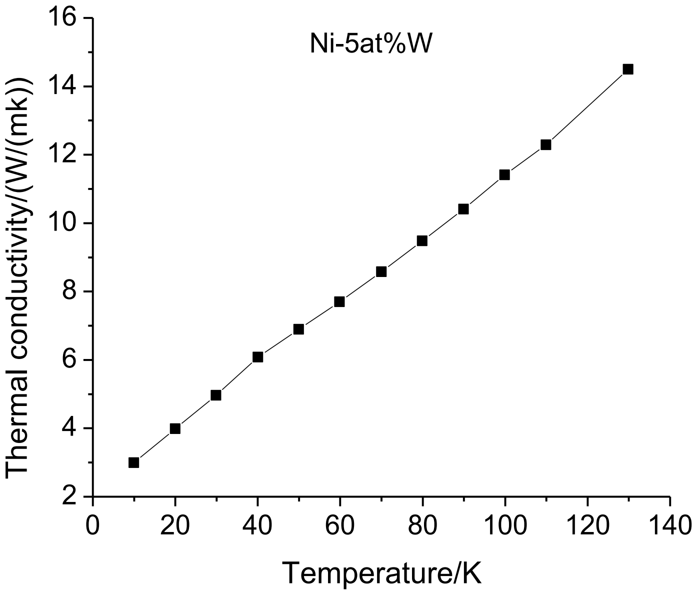

Figure 0.3 Thermal conductivity of Ni-5at%W under different temperature [129]. As shown in the figure, the thermal conductivity of Ni-5at% W increases linearly with the increase temperature.

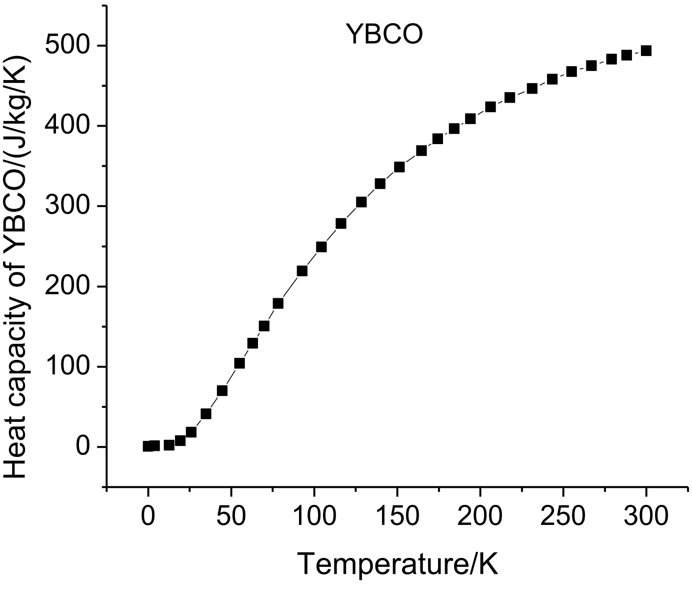

Figure 0.4 Heat capacity of YBCO under different temperatures [130]. This figure shows that the heat capacity of YBCO increases gradually with temperature.

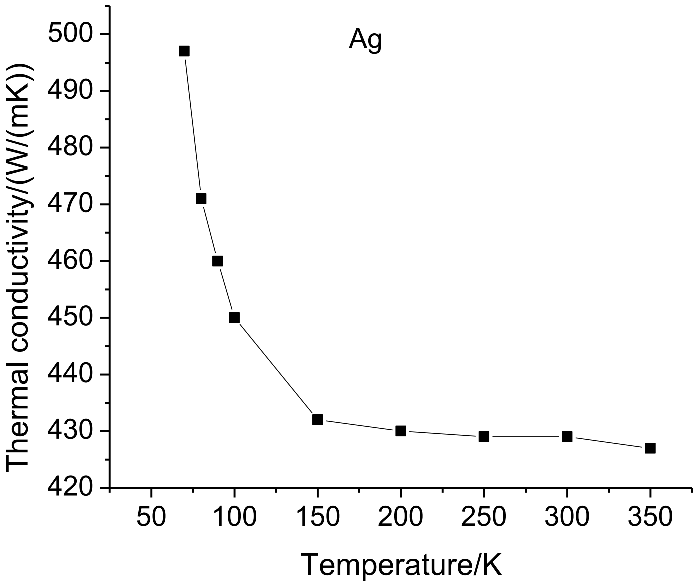

Figure 0.5 Thermal conductivity of silver under different temperatures [132, 133]. The figure shows that the thermal conductivity of silver decreases gradually with temperature.

Reference

[1] I. E. Commission, "'Efficient Electrical Energy Transmission and Distribution," *Report, Switzerland,* 2007.

[2] D. Van Delft and P. Kes, "The discovery of superconductivity," *Physics Today,* vol. 63, pp. 38-43, 2010.

[3] J. G. Bednorz and K. A. Müller, "Possible high T c superconductivity in the Ba—La—Cu—O system," in *Ten Years of Superconductivity: 1980–1990,* ed: Springer, 1986, pp. 267-271.

[4] P. Dai, B. Chakoumakos, G. Sun, K. Wong, Y. Xin, and D. Lu, "Synthesis and neutron powder diffraction study of the superconductor HgBa2Ca2Cu3O8+ δ by Tl substitution," *Physica C: Superconductivity,* vol. 243, pp. 201-206, 1995.

[5] A. Drozdov, M. Eremets, I. Troyan, V. Ksenofontov, and S. Shylin, "Conventional superconductivity at 203 kelvin at high pressures in the sulfur hydride system," *Nature,* vol. 525, pp. 73-76, 2015.

[6] W. Meissner and R. Ochsenfeld, "Ein neuer effekt bei eintritt der supraleitfähigkeit," *Naturwissenschaften,* vol. 21, pp. 787-788, 1933.

[7] T. Masuda, H. Yumura, M. Watanabe, H. Takigawa, Y. Ashibe, C. Suzawa, *et al.*, "High-temperature superconducting cable technology and development trends," *SEI Technical Review,* vol. 59, p. 13, 2005.

[8] Z. Zhang, "Electrical characterizing of superconducting power cable consisted of Second-Generation High-temperature superconducting tapes," Doctor of Philosophy, University of Bath, 2016.

[9] A. Morandi, L. Trevisani, P. Ribani, M. Fabbri, L. Martini, and M. Bocchi, "Superconducting transformers: key design aspects for power applications," in *Journal of Physics: Conference Series*, 2008, p. 012318.

[10] Z. Melhem, *High temperature superconductors (HTS) for energy applications*: Elsevier, 2011.

[11] M. Noe and M. Steurer, "High-temperature superconductor fault current limiters: concepts, applications, and development status," *Superconductor Science and Technology,* vol. 20, p. R15, 2007.

[12] Y. Xin, W. Gong, H. Hong, Y. Gao, X. Niu, J. Zhang, *et al.*, "Development of a 220 kV/300 MVA superconductive fault current limiter," *Superconductor Science and Technology,* vol. 25, p. 105011, 2012.

[13] Z. Hong, J. Sheng, J. Zhang, B. Lin, L. Ying, Y. Li, *et al.*, "The development and performance test of a 10 kV resistive type superconducting fault current limiter," *Applied Superconductivity, IEEE Transactions on,* vol. 22, pp. 5600504-5600504, 2012.

[14] L. Martini, M. Bocchi, M. Ascade, A. Valzasina, V. Rossi, C. Ravetta, *et al.*, "The first Italian Superconducting Fault Current Limiter: Results of the field testing experience after one year operation," in *Journal of Physics: Conference Series*, 2014, p. 032003.

[15] Y. Xin, W. Gong, X. Niu, Y. Gao, Q. Guo, L. Xiao, *et al.*, "Manufacturing and test of a 35 kV/90 MVA saturated iron-core type superconductive fault current limiter for live-grid operation," *Applied Superconductivity, IEEE Transactions on,* vol. 19, pp. 1934-1937, 2009.

[16] J. Bock, F. Breuer, H. Walter, S. Elschner, M. Kleimaier, R. Kreutz, *et al.*, "CURL 10: Development and field-test of a 10 kV/10 MVA resistive current limiter based on bulk MCP-BSCCO 2212," *Applied Superconductivity, IEEE Transactions on,* vol. 15, pp. 1955-1960, 2005.

[17] S. Elschner, F. Breuer, H. Walter, and J. Bock, "Magnetic field assisted quench propagation as a new concept for resistive current limiting devices," in *Journal of Physics: Conference Series*, 2006, p. 917.

[18] P. Tixador, T. Nguyen-Nhat, H. Okada-Vieira, and R. Ponceau, "Impact of conductor inhomogeneity on fcl transient performance," *Applied Superconductivity, IEEE Transactions on,* vol. 21, pp. 1194-1197, 2011.

[19] P. Tixador and N. T. Nguyen, "Design of ReBaCuO-coated conductors for FCL," *Superconductor Science and Technology,* vol. 25, p. 014009, 2012.

[20] D. Colangelo and B. Dutoit, "Analysis of the influence of the normal zone propagation velocity on the design of resistive fault current limiters," *Superconductor Science and Technology,* vol. 27, p. 124005, 2014.

[21] Z. Zhong, H. Ruiz, L. Lai, Z. Huang, W. Wang, and T. Coombs, "Experimental Study of the Normal Zone Propagation Velocity in Double-layer 2G-HTS wires by Thermal and Electrical Methods," *Applied Superconductivity, IEEE Transactions on*, vol. 25, pp. 1-5, 2015.

[22] R. Kreutz, J. Bock, F. Breuer, K.-P. Juengst, M. Kleimaier, H.-U. Klein, *et al.*, "System technology and test of CURL 10, a 10 kV, 10 MVA resistive high-Tc superconducting fault current limiter," *Applied Superconductivity, IEEE Transactions on*, vol. 15, pp. 1961-1964, 2005.

[23] J. Bock, M. Bludau, R. Dommerque, A. Hobl, S. Kraemer, M. Rikel, *et al.*, "HTS fault current limiters—First commercial devices for distribution level grids in Europe," *Applied Superconductivity, IEEE Transactions on,* vol. 21, pp. 1202-1205, 2011.

[24] S. Elschner, A. Kudymow, J. Brand, S. Fink, W. Goldacker, F. Grilli, *et al.*, "ENSYSTROB–Design, manufacturing and test of a 3-phase resistive fault current limiter based on coated conductors for medium voltage application," *Physica C: Superconductivity,* vol. 482, pp. 98-104, 2012.

[25] S. Elschner, A. Kudymow, S. Fink, W. Goldacker, F. Grilli, C. Schacherer, *et al.*, "ENSYSTROB—Resistive fault current limiter based on coated conductors for medium voltage application," *Applied Superconductivity, IEEE Transactions on,* vol. 21, pp. 1209-1212, 2011.

[26] L. Martini, M. Noe, P. Tixador, M. Bocchi, and A. Hobl, "he ECCOFLOW project: Design and simulations results of a Superconducting Fault Current Limiter for

Operation in Electricity Networks," in *21st International Conference on Electricity Distribution*, 2011.

[27] A. Hobl, W. Goldacker, B. Dutoit, L. Martini, A. Petermann, and P. Tixador, "Design and production of the ECCOFLOW resistive fault current limiter," *IEEE transactions on applied superconductivity,* vol. 23, pp. 5601804-5601804, 2013.

[28] H.-W. Neumueller, W. Schmidt, H.-P. Kraemer, A. Otto, J. Maguire, J. Yuan*, et al.*, "Development of resistive fault current limiters based on YBCO coated conductors," *IEEE Transactions on Applied Superconductivity,* vol. 19, pp. 1950-1955, 2009.

[29] Available: http://www.amsc.com/solutions-products/hts_wire.html

[30] Z. Hong, J. Sheng, L. Yao, J. Gu, and Z. Jin, "The Structure, Performance and Recovery Time of a 10 kV Resistive Type Superconducting Fault Current Limiter," *Applied Superconductivity, IEEE Transactions on,* vol. 23, pp. 5601304-5601304, 2013.

[31] K. Yasuda, A. Ichinose, A. Kimura, K. Inoue, H. Morii, Y. Tokunaga*, et al.*, "Research & development of superconducting fault current limiter in Japan," *IEEE transactions on applied superconductivity,* vol. 15, pp. 1978-1981, 2005.

[32] T. Yazawa, K. Koyanagi, M. Takahashi, K. Toba, H. Takigami, M. Urata*, et al.*, "Development of 6.6 kV/600A superconducting fault current limiter using coated conductors," *Physica C: Superconductivity,* vol. 469, pp. 1740-1744, 2009.

[33] Y. Xin, W. Gong, X. Niu, Z. Cao, J. Zhang, B. Tian*, et al.*, "Development of saturated iron core HTS fault current limiters," *IEEE Transactions on Applied Superconductivity,* vol. 17, pp. 1760-1763, 2007.

[34] F. Moriconi, F. De La Rosa, A. Singh, B. Chen, M. Levitskaya, and A. Nelson, "An innovative compact saturable-core HTS Fault Current Limiter-development, testing and application to transmission class networks," in *Power and Energy Society General Meeting, 2010 IEEE*, 2010, pp. 1-8.

[35] H. Boenig and D. Paice, "Fault current limiter using a superconducting coil," *IEEE Transactions on Magnetics,* vol. 19, pp. 1051-1053, 1983.

[36] T. Yazawa, E. Yoneda, J. Matsuzaki, M. Shimada, T. Kuriyama, S. Nomura*, et al.*, "Design and test results of 6.6 kV high-Tc superconducting fault current limiter," *IEEE transactions on applied superconductivity,* vol. 11, pp. 2511-2514, 2001.

[37] D. Hui, Z. Wang, J. Zhang, D. Zhang, S. Dai, C. Zhao*, et al.*, "Development and test of 10.5 kV/1.5 kA HTS fault current limiter," *IEEE transactions on applied superconductivity,* vol. 16, pp. 687-690, 2006.

[38] T. Ise, N. H. Nguyen, and S. Kumagai, "Reduction of inductance and current rating of the coil and enhancement of fault current limiting capability of a rectifier type superconducting fault current limiter," *IEEE transactions on applied superconductivity,* vol. 11, pp. 1932-1935, 2001.

[39] H. Kang, M. C. Ahn, Y. K. Kim, D. K. Bae, Y. S. Yoon, T. K. Ko*, et al.*, "Design, fabrication and testing of superconducting DC reactor for 1.2 kV/80 A inductive fault current limiter," *IEEE transactions on applied superconductivity,* vol. 13, pp. 2008-2011, 2003.

[40] J. Kozak, T. Janowski, S. Kozak, H. Malinowski, G. Wojtasiewicz, and B. Kondratowicz-Kucewicz, "Design and testing of 230 V inductive type of superconducting fault current limiter with an open core," *IEEE Transactions on applied superconductivity,* vol. 15, pp. 2031-2034, 2005.

[41] W. Paul, M. Lakner, J. Rhyner, P. Unternährer, T. Baumann, M. Chen*, et al.*, "Test of 1.2 MVA high-superconducting fault current limiter," *Superconductor Science and Technology,* vol. 10, p. 914, 1997.

[42] W. Paul, T. Baumann, J. Rhyner, and F. Platter, "Tests of 100 kW High-T/sub c/superconducting fault current limiter," *IEEE Transactions on applied superconductivity,* vol. 5, pp. 1059-1062, 1995.

[43] M. Ichikawa and M. Okazaki, "A magnetic shielding type superconducting fault current limiter using a Bi2212 thick film cylinder," *IEEE Transactions on Applied Superconductivity,* vol. 5, pp. 1067-1070, 1995.

[44] H. Kado and M. Ickikawa, "Performance of a high-Tc superconducting fault current limiter-design of a 6.6 kV magnetic shielding type superconducting fault current limiter," *IEEE transactions on applied superconductivity,* vol. 7, pp. 993-996, 1997.

[45] M. Steurer, H. Brechna, and K. Frohlich, "A nitrogen gas cooled, hybrid, high temperature superconducting fault current limiter," *IEEE transactions on applied superconductivity,* vol. 10, pp. 840-844, 2000.

[46] M. Endo, T. Hori, T. Koyama, K. Kaiho, I. Yamaguchi, K. Arai*, et al.*, "Development of a superconducting fault current limiter using various high-speed circuit breakers," *IET electric power applications,* vol. 3, pp. 363-370, 2009.

[47] J. B. Na, Y. J. Kim, J. Y. Jang, K. S. Ryu, Y. J. Hwang, S. Choi*, et al.*, "Design and tests of prototype hybrid superconducting fault current limiter with fast switch," *IEEE Transactions on Applied Superconductivity,* vol. 22, pp. 5602604-5602604, 2012.

[48] G.-H. Lee, K.-B. Park, J. Sim, Y.-G. Kim, I.-S. Oh, O.-B. Hyun*, et al.*, "Hybrid superconducting fault current limiter of the first half cycle non-limiting type," *IEEE Transactions on Applied Superconductivity,* vol. 19, pp. 1888-1891, 2009.

[49] B. Lee, K. Park, J. Sim, I. Oh, H. Lee, H. Kim*, et al.*, "Design and experiments of novel hybrid type superconducting fault current limiters," *IEEE transactions on applied superconductivity,* vol. 18, pp. 624-627, 2008.

[50] O.-B. Hyun, J. Sim, H.-R. Kim, K.-B. Park, S.-W. Yim, and I.-S. Oh, "Reliability enhancement of the fast switch in a hybrid superconducting fault current limiter by using power electronic switches," *IEEE Transactions on Applied Superconductivity,* vol. 19, pp. 1843-1846, 2009.

[51] H.-R. Kim, S.-E. Yang, S.-D. Yu, H. Kim, W.-S. Kim, K. Park*, et al.*, "Installation and testing of SFCLs," *IEEE Transactions on Applied Superconductivity,* vol. 22, pp. 5602704-5602704, 2012.

[52] M. J. Kim, W. Choe, S.-H. Bang, H. Y. Park, G.-H. Lee, J. Sim*, et al.*, "Development of a fault current limiter for 22.9 kV distribution power line," in *Electric Power Equipment-Switching Technology (ICEPE-ST), 2013 2nd International Conference on*, 2013, pp. 1-4.

[53] C. Lacroix and F. Sirois, "Concept of a current flow diverter for accelerating the normal zone propagation velocity in 2G HTS coated conductors," *Superconductor Science and Technology,* vol. 27, p. 035003, 2014.

[54] M. C. Ahn, D. K. Bae, S. E. Yang, D. K. Park, T. K. Ko, C. Lee, *et al.*, "Manufacture and test of small-scale superconducting fault current limiter by using the bifilar winding of coated conductor," *Applied Superconductivity, IEEE Transactions on,* vol. 16, pp. 646-649, 2006.

[55] J. Šouc, F. Gömöry, and M. Vojenčiak, "Coated conductor arrangement for reduced AC losses in a resistive-type superconducting fault current limiter," *Superconductor Science and Technology,* vol. 25, p. 014005, 2011.

[56] D. N. Nguyen, F. Grilli, S. P. Ashworth, and J. O. Willis, "AC loss study of antiparallel connected YBCO coated conductors," *Superconductor Science and Technology,* vol. 22, p. 055014, 2009.

[57] D. Hu, M. D. Ainslie, J. P. Rush, J. H. Durrell, J. Zou, M. Raine, *et al.*, "DC characterization and 3D modelling of a triangular, epoxy-impregnated high temperature superconducting coil," *Superconductor Science and Technology,* vol. 28, p. 065011, 2015.

[58] W. Norris, "Calculation of hysteresis losses in hard superconductors carrying ac: isolated conductors and edges of thin sheets," *Journal of Physics D: Applied Physics,* vol. 3, p. 489, 1970.

[59] E. H. Brandt and M. Indenbom, "Type-II-superconductor strip with current in a perpendicular magnetic field," *Physical review B,* vol. 48, p. 12893, 1993.

[60] J. R. Clem, J. Claassen, and Y. Mawatari, "AC losses in a finite Z stack using an anisotropic homogeneous-medium approximation," *Superconductor Science and Technology,* vol. 20, p. 1130, 2007.

[61] W. Yuan, A. Campbell, and T. Coombs, "A model for calculating the AC losses of second-generation high temperature superconductor pancake coils," *Superconductor Science and Technology,* vol. 22, p. 075028, 2009.

[62] W. Yuan, A. Campbell, and T. Coombs, "Ac losses and field and current density distribution during a full cycle of a stack of superconducting tapes," *Journal of Applied Physics,* vol. 107, p. 093909, 2010.

[63] W. Yuan, A. Campbell, Z. Hong, M. Ainslie, and T. Coombs, "Comparison of AC losses, magnetic field/current distributions and critical currents of superconducting circular pancake coils and infinitely long stacks using coated conductors," *Superconductor Science and Technology,* vol. 23, p. 085011, 2010.

[64] L. Prigozhin and V. Sokolovsky, "Computing AC losses in stacks of high-temperature superconducting tapes," *Superconductor Science and Technology,* vol. 24, p. 075012, 2011.

[65] E. Pardo, "Calculation of AC loss in coated conductor coils with a large number of turns," *Superconductor Science and Technology,* vol. 26, p. 105017, 2013.

[66] E. Pardo, "Modeling of coated conductor pancake coils with a large number of turns," *Superconductor Science and Technology,* vol. 21, p. 065014, 2008.

[67] E. Pardo, J. Šouc, and J. Kováč, "AC loss in ReBCO pancake coils and stacks of them: modelling and measurement," *Superconductor Science and Technology,* vol. 25, p. 035003, 2012.

[68] A. Stenvall and T. Tarhasaari, "An eddy current vector potential formulation for estimating hysteresis losses of superconductors with FEM," *Superconductor Science and Technology,* vol. 23, p. 125013, 2010.

[69] F. Gömöry, M. Vojenčiak, E. Pardo, and J. Šouc, "Magnetic flux penetration and AC loss in a composite superconducting wire with ferromagnetic parts," *Superconductor Science and Technology,* vol. 22, p. 034017, 2009.

[70] N. Amemiya, S.-i. Murasawa, N. Banno, and K. Miyamoto, "Numerical modelings of superconducting wires for AC loss calculations," *Physica C: Superconductivity,* vol. 310, pp. 16-29, 1998.

[71] N. Enomoto and N. Amemiya, "Electromagnetic field analysis of rectangular high T c superconductor with large aspect ratio," *Physica C: Superconductivity,* vol. 412, pp. 1050-1055, 2004.

[72] Z. Hong, A. Campbell, and T. Coombs, "Numerical solution of critical state in superconductivity by finite element software," *Superconductor Science and Technology,* vol. 19, p. 1246, 2006.

[73] R. Brambilla, F. Grilli, and L. Martini, "Development of an edge-element model for AC loss computation of high-temperature superconductors," *Superconductor Science and Technology,* vol. 20, p. 16, 2007.

[74] H. Z. M. Z. W. Yuan. (2016). *An efficient 3D FEM model based on T-A formula for superconducting coated conductors*. Available: http://www.die.ing.unibo.it/pers/morandi/didattica/Temporary-HTSModelling2016/Zhang.pdf

[75] M. Z. Huiming Zhang, Weijia Yuan, "An efficient 3D finite element method model based on the T–A formulation for superconducting coated conductors," *Superconductor Science and Technology,* vol. 30, p. 024005, 2017.

[76] F. Roy, S. Pérez, M. Therasse, B. Dutoit, F. Sirois, M. Decroux, *et al.*, "Quench propagation in coated conductors for fault current limiters," *Physica C: Superconductivity,* vol. 469, pp. 1462-1466, 2009.

[77] F. Roy, B. Dutoit, F. Grilli, and F. Sirois, "Magneto-thermal modeling of second-generation HTS for resistive fault current limiter design purposes," *Applied Superconductivity, IEEE Transactions on,* vol. 18, pp. 29-35, 2008.

[78] M. Zhang, K. Matsuda, and T. Coombs, "New application of temperature-dependent modelling of high temperature superconductors: Quench propagation and pulse magnetization," *Journal of Applied Physics,* vol. 112, p. 043912, 2012.

[79] M. Zhang, J.-H. Kim, S. Pamidi, M. Chudy, W. Yuan, and T. Coombs, "Study of second generation, high-temperature superconducting coils: Determination of critical current," *Journal of Applied Physics,* vol. 111, p. 083902, 2012.

[80] J. Duron, F. Grilli, L. Antognazza, M. Decroux, B. Dutoit, and Ø. Fischer, "Finite-element modelling of YBCO fault current limiter with temperature dependent parameters," *Superconductor Science and Technology,* vol. 20, p. 338, 2007.

[81] K. S. Chang, D. K. Park, S. E. Yang, Y. J. Kim, S. Y. Chu, M. C. Ahn, *et al.*, "Characteristic comparison of the superconducting fault current limiter with various bypass reactors," *Applied Superconductivity, IEEE Transactions on,* vol. 20, pp. 1190-1193, 2010.

[82] W. K. Chan, P. J. Masson, C. Luongo, and J. Schwartz, "Three-Dimensional Micrometer-Scale Modeling of Quenching in High-Aspect-Ratio Coated Conductor Tapes—Part I: Model Development and Validation," *Applied Superconductivity, IEEE Transactions on,* vol. 20, pp. 2370-2380, 2010.

[83] W. K. Chan and J. Schwartz, "Three-Dimensional Micrometer-Scale Modeling of Quenching in High-Aspect-Ratio Coated Conductor Tapes—Part II: Influence of Geometric and Material Properties and Implications for Conductor Engineering and Magnet Design," *Applied Superconductivity, IEEE Transactions on,* vol. 21, pp. 3628-3634, 2011.

[84] A. Badel, L. Antognazza, M. Therasse, M. Abplanalp, C. Schacherer, and M. Decroux, "Hybrid model of quench propagation in coated conductors for fault current limiters," *Superconductor Science and Technology,* vol. 25, p. 095015, 2012.

[85] S. M. Blair, C. D. Booth, and G. M. Burt, "Current–time characteristics of resistive superconducting fault current limiters," *Applied Superconductivity, IEEE Transactions on,* vol. 22, pp. 5600205-5600205, 2012.

[86] W. De Sousa, A. Polasek, R. Dias, C. Matt, and R. de Andrade, "Thermal–electrical analogy for simulations of superconducting fault current limiters," *Cryogenics,* vol. 62, pp. 97-109, 2014.

[87] C.-H. Bonnard, F. Sirois, C. Lacroix, and G. Didier, "Multi-scale model of resistive-type superconducting fault current limiters based on 2G HTS coated conductors," *Superconductor Science and Technology,* vol. 30, p. 014005, 2016.

[88] A. Kalinov, I. Voloshin, and L. Fisher, "SPICE model of high-temperature superconducting tape: application to resistive fault-current limiter," *Superconductor Science and Technology,* vol. 30, p. 054002, 2017.

[89] M. F. Antono Morandi, Babak Gholizad, "Modeling of the Resistive Type Superconducting Fault Curent Limiter for Power System Analysis and Optimization," in *HTS Modelling 2014*, 2014.

[90] L. Kovalsky. (2005). *Matrix Fault Current Limiter Project Update*. Available: http://www.superpower-inc.com/files/T361+Peer+Rev+MFCL+Update.pdf

[91] J. Llambes, C. Weber, and D. Hazelton, "Testing and demonstration results for the transmission-level (138 kV) 2G superconducting fault current limiter at SuperPower," in *Applied Superconducting Conf., Chicago, Illinois, USA*, 2008.

[92] J. Maguire and J. Yuan, "Status of high temperature superconductor cable and fault current limiter projects at American Superconductor," *Physica C: Superconductivity,* vol. 469, pp. 874-880, 2009.

[93] H. Kim, J.-Y. Lee, H.-R. Kim, S.-E. Yang, S.-D. Yu, W.-S. Kim, *et al.*, "An Effect of HTS Wire Configuration on Quench Recovery Time in a Resistive SFCL," *Applied Superconductivity, IEEE Transactions on,* vol. 23, pp. 5604104-5604104, 2013.

[94] W. Schmidt, B. Gamble, H. Kraemer, D. Madura, A. Otto, and W. Romanosky, "Design and test of current limiting modules using YBCO-coated conductors," *Superconductor Science and Technology,* vol. 23, p. 014024, 2010.

[95] F. Liang, W. Yuan, M. Zhang, Z. Zhang, S. Venuturumilli, and J. Patel, "The Impact of Critical Current Inhomogeneity in HTS Coated Conductors on the Quench Process for SFCL Application," *IEEE Transactions on Applied Superconductivity,* vol. 26, pp. 1-5, 2016.

[96] M.-J. Park, S.-Y. Kwak, W.-S. Kim, S.-W. Lee, J.-K. Lee, J.-H. Han*, et al.*, "AC loss and thermal stability of HTS model coils for a 600 kJ SMES," *Applied Superconductivity, IEEE Transactions on,* vol. 17, pp. 2418-2421, 2007.

[97] D. N. Nguyen, S. P. Ashworth, and J. O. Willis, "Numerical analysis of ac loss in bifilar stacks and coils of ion beam assisted deposition YBCO coated conductors," *Journal of Applied Physics,* vol. 105, p. 063917, 2009.

[98] J. R. Clem, "Field and current distributions and ac losses in a bifilar stack of superconducting strips," *Physical Review B,* vol. 77, p. 134506, 2008.

[99] D. Nguyen, J. Coulter, J. Willis, S. Ashworth, H. Kraemer, W. Schmidt*, et al.*, "AC loss and critical current characterization of a noninductive coil of two-in-hand RABiTS YBCO tape for fault current limiter applications," *Superconductor Science and Technology,* vol. 24, p. 035017, 2011.

[100] F. Liang, W. Yuan, C. A. Baldan, M. Zhang, and J. S. Lamas, "Modeling and Experiment of the Current Limiting Performance of a Resistive Superconducting Fault Current Limiter in the Experimental System," *Journal of Superconductivity and Novel Magnetism,* vol. 28, pp. 2669-2681, 2015.

[101] A. Smith, A. Oliver, X. Pei, M. Husband, and M. Rindfleisch, "Experimental testing and modelling of a resistive type superconducting fault current limiter using MgB2 wire," *Superconductor Science and Technology,* vol. 25, p. 125018, 2012.

[102] X. Pei, "Superconducting fault current limiter with integrated vacuum interrupter," 2012.

[103] K. H. Víctor M. R. Zermeño, Mariusz Stępień, Francesco Grilli (2016). *A collection of methods to extract local Jc(B) models from experimental data: From brute force fitting to regularization-free strategies*. Available: https://events.unibo.it/htsmodelling2016/program

[104] V. M. Zermeño, K. Habelok, M. Stępień, and F. Grilli, "A parameter-free method to extract the superconductor's $ J_c (B,\ theta) $ field-dependence from in-field current-voltage characteristics of HTS tapes," *arXiv preprint arXiv:1608.08378,* 2016.

[105] M. Solovyov, E. Pardo, G. Fedor, M. Skarba, P. Konopka, and J. Janovec, "Non-uniformity of coated conductor tapes," *Superconductor Science and Technology,* vol. 26, p. 115013, 2013.

[106] N. Amemiya, T. Tsukamoto, M. Nii, T. Komeda, T. Nakamura, and Z. Jiang, "Alternating current loss characteristics of a Roebel cable consisting of coated conductors and a three-dimensional structure," *Superconductor Science and Technology,* vol. 27, p. 035007, 2014.

[107] N. Amemiya, O. Maruyama, M. Mori, N. Kashima, T. Watanabe, S. Nagaya, *et al.*, "Lateral J c distribution of YBCO coated conductors fabricated by IBAD/MOCVD process," *Physica C: Superconductivity and its applications,* vol. 445, pp. 712-716, 2006.

[108] N. Amemiya, Q. Li, R. Nishino, K. Takeuchi, T. Nakamura, K. Ohmatsu, *et al.*, "Lateral critical current density distributions degraded near edges of coated conductors through cutting processes and their influence on ac loss characteristics of power transmission cables," *Physica C: Superconductivity,* vol. 471, pp. 990-994, 2011.

[109] J. Hänisch, F. Mueller, S. Ashworth, J. Coulter, and V. Matias, "Measurement of the transverse Jc profiles of coated conductors using a magnetic knife of permanent magnets," *Superconductor Science and Technology,* vol. 21, p. 115021, 2008.

[110] N. Amemiya, Y. Shinkai, Y. Iijima, K. Kakimoto, and K. Takeda, "Experimental determination of two-dimensional critical current density distribution in YBCO coated conductors," *Superconductor Science and Technology,* vol. 14, p. 611, 2001.

[111] M. W. Rupich, X. Li, S. Sathyamurthy, C. L. Thieme, K. DeMoranville, J. Gannon, *et al.*, "Second generation wire development at AMSC," *IEEE transactions on applied superconductivity,* vol. 23, pp. 6601205-6601205, 2013.

[112] S. Fleshler, D. Buczek, B. Carter, P. Cedrone, K. DeMoranville, J. Gannon, *et al.*, "Scale-up of 2G wire manufacturing at American Superconductor Corporation," *Physica C: Superconductivity,* vol. 469, pp. 1316-1321, 2009.

[113] W. Schmidt, H.-P. Kraemer, H.-W. Neumueller, U. Schoop, D. Verebelyi, and A. P. Malozemoff, "Investigation of YBCO coated conductors for fault current limiter applications," *IEEE Transactions on Applied Superconductivity,* vol. 17, pp. 3471-3474, 2007.

[114] C. A. Baldan, L. C. Guedes, J. S. Lamas, C. Y. Shigue, and E. Ruppert, "Development and test of resistive superconducting fault current limiter; acting time and its recovery conditions," in *Journal of Physics: Conference Series*, 2014, p. 032004.

[115] D. N. Nguyen, S. P. Ashworth, J. O. Willis, F. Sirois, and F. Grilli, "A new finite-element method simulation model for computing AC loss in roll assistedbiaxially textured substrate YBCO tapes," *Superconductor Science and Technology,* vol. 23, p. 025001, 2009.

[116] M. Zhang, J. Kvitkovic, S. Pamidi, and T. Coombs, "Experimental and numerical study of a YBCO pancake coil with a magnetic substrate," *Superconductor Science and technology,* vol. 25, p. 125020, 2012.

[117] M. D. Ainslie, V. M. Rodriguez-Zermeno, Z. Hong, W. Yuan, T. J. Flack, and T. A. Coombs, "An improved FEM model for computing transport AC loss in coils made of RABiTS YBCO coated conductors for electric machines," *Superconductor Science and Technology,* vol. 24, p. 045005, 2011.

[118] J. Duron, F. Grilli, B. Dutoit, and S. Stavrev, "Modelling the< i> E</i>–< i> J</i> relation of high-< i> T</i>< sub> c</sub> superconductors in an arbitrary current range," *Physica C: Superconductivity,* vol. 401, pp. 231-235, 2004.

[119] W. Paul, M. Chen, M. Lakner, J. Rhyner, D. Braun, W. Lanz, *et al.*, "Superconducting fault current limiter: applications, technical and economical benefits, simulations and test results," *CIGRÉ session 2000*, 2000.

[120] C. A. Baldan, J. S. Lamas, and C. Y. Shigue, "Test of a modular fault current limiter for 220 V line using YBCO coated conductor tapes with shunt protection," *Applied Superconductivity, IEEE Transactions on*, vol. 21, pp. 1242-1245, 2011.

[121] N. Nguyen and P. Tixador, "A YBCO-coated conductor for a fault current limiter: architecture influences and optical study," *Superconductor Science and Technology*, vol. 23, p. 025008, 2010.

[122] O. Umezawa and K. Ishikawa, "Electrical and thermal conductivities and magnetization of some austenitic steels, titanium and titanium alloys at cryogenic temperatures," *Cryogenics*, vol. 32, pp. 873-880, 1992.

[123] X. Wang, U. Trociewitz, and J. Schwartz, "Self-field quench behaviour of YBa2Cu3O7− δ coated conductors with different stabilizers," *Superconductor Science and Technology*, vol. 22, p. 085005, 2009.

[124] (2014-2015). *Handbook of Chemistry and Physics*. Available: http://www.hbcpnetbase.com/

[125] *Sn 62 Sn-Pb-Ag Solder Alloy*. Available: http://www.matweb.com/search/datasheet.aspx?matguid=703a13aad9d444bc988c4d6f96675045&ckck=1

[126] *Sn 63 Sn-Pb solder alloy*. Available: http://www.matweb.com/search/datasheet.aspx?MatGUID=c1d1b91a360748bf9944a0c771e8d5b2

[127] E. J. W, *Experimental Techniques for Low-Temperature Measurements*. Oxford: Oxford University Press, 2006.

[128] D. K. Park, J. S. Bang, S. E. Yang, T. K. Ko, Y. S. Yoon, M. C. Ahn, *et al.*, "Theoretical and experimental analysis of AC loss characteristic of bifilar pancake coil with coated conductor," *Applied Superconductivity, IEEE Transactions on*, vol. 18, pp. 1232-1235, 2008.

[129] C. Hoffmann, N. Strickland, D. Pooke, J. Gannon, B. Carter, and A. Otto, "Thermal conductivity of 2G HTS wires for current lead applications," in *Journal of Physics: Conference Series*, 2010, p. 022015.

[130] A. Junod, T. Graf, D. Sanchez, G. Triscone, and J. Muller, "Specific heat of the superconductor Yba2Cu4O8 from 1.5 to 300K," *Physica B: Condensed Matter*, vol. 165–166, Part 2, pp. 1335-1336, 8// 1990.

[131] *Electrical resistivity and conductivity*. Available: http://en.wikipedia.org/wiki/Electrical_resistivity_and_conductivity

[132] D. J. Griffiths and R. College, *Introduction to electrodynamics* vol. 3: Prentice hall Upper Saddle River, NJ, 1999.

[133] R. A. Serway, "Principles of Physics . Fort Worth, Texas; London: Saunders College Pub," ISBN 0-03-020457-71998.

[134] D. Colangelo and B. Dutoit, "Inhomogeneity effects in HTS coated conductors used as resistive FCLs in medium voltage grids," *Superconductor science and technology,* vol. 25, p. 095005, 2012.

[135] J. Duron, F. Grilli, B. Dutoit, and S. Stavrev, "Modelling the E–J relation of high-T c superconductors in an arbitrary current range," *Physica C: Superconductivity,* vol. 401, pp. 231-235, 2004.